The cryogenic photon detection system for the ALPS II experiment: characterization, optimization and background rejection.

vorgelegt von

NOEMIE ALICE CHLOE BASTIDON

aus Pierrelatte (Frankreich)

Hamburg 2016

Abstract

The search for new fundamental bosons at very low mass is the central objective of the ALPS II experiment which is currently set up at the Deutsches Elektronen-Synchrotron (DESY, Hamburg). This experiment follows the light-shining-through-the-wall concept where photons could oscillate into weakly interacting light bosons in front of a wall and back into photons behind the wall, giving the impression that light can shine through a light tight barrier. In this concept, the background-free detection of near-infrared photons is required to fully exploit the sensitivity of the apparatus.

The high efficiency single-photon detection in the near-infrared is challenging and requires a cryogenic detector. In this project, a Transition-Edge Sensor (TES) operated below 100 mK will be used to detect single photons.

This thesis focuses on the characterization and optimization of the ALPS II detector system including an Adiabatic Demagnetisation Refrigerator (ADR) with its two-stage pulse-tube cooler, two TES detectors and their Superconducting Quantum Interference Devices (SQUIDs) read-out system.

Stability of the detection system over time is a priority in the ALPS II experiment. It is in this context that the cooling system has been subjected to many upgrades. In the framework of this thesis, the cooling setup has been studied in detail in order to optimize its cooling performances. Furthermore, the stability of the detector has been studied according to various criteria.

Other essential parameters of the ALPS II experiment are its detection efficiency and its background rate. Indeed, the sensitivity of the experiment directly depends on these two characteristics. Both elements have been studied in depth in order to define if the chosen TES detector will meet ALPS IIc specifications.

Kurzfassung

Die Suche nach neuen fundamentalen Bosonen niedriger Masse ist das zentrale Ziel des ALPS II Experimentes, das zur Zeit am Deutschen Elektronen-Synchrotron (DESY, Hamburg) aufgebaut ist. Die Grundlage für dieses Experiment ist das light-shining-through-the-wall Konzept (übersetzt: Licht leuchtet durch die Wand). Hierbei können Photonen vor einer lichtundurchlässigen Wand in schwach wechselwirkende, leichte Bosonen oszillieren und hinter der Wand wieder in Photonen oszillieren. Dadurch entsteht der Eindruck, dass Licht durch die Wand leuchtet. Zur vollen Ausschöpfung der Sensitivität erfordert dieses Konzept eine hintergrundfreie Detektion von Nahinfrarotphotonen.

Die Detektion einzelner Photonen im Nahinfrarotbereich stellt eine Herausforderung dar und erfordert Kryogen-Technik. In diesem Projekt wird ein *Transition-Edge Sensor* (TES) mit einer Betriebstemperatur von weniger als 100 mK für die Detektion von einzelnen Photonen verwendet.

Diese Arbeit befasst sich hauptsächlich mit der Charakterisierung und Optimierung des ALPS-II Detektor-Systems. Dieses beinhaltet einen adiabatischen Entmagnetisierungs Kühler (Adiabatic Demagnetisation Refrigerator, ADR) mit einem zwei-Stufen-Pulsrohr-Kühler (engl.: two-stage pulsetube cooler) und zwei TES Detektoren mit zugehörigen SQUID (engl.: Superconducting Quantum Interference Devices) Auslesesystemen.

Die zeitliche Stabilität des Systems hat eine hohe Priorität für das ALPS II Experiment. In diesem Zusammenhang wurde das Kühlsystem mehreren Nachrüstungen unterzogen. Im Rahmen dieser Doktorarbeit wurde das Kühlsystem ausführlich studiert, um dessen Leistung zu optimieren. Ausserdem wurde die Stabilität des Detektors auf der Grundlage unterschiedlicher Kriterien studiert.

Weitere essentielle Parameter des ALPS II Experiments sind dessen Detektions Effizienz und Hintergrundrate. Die Sensitivität hängt direkt von diesen beiden Parametern ab. Beide Spezifikationen wurden im Detail studiert, um die Eignung des gewählten TES Detektors zu überprüfen.

Contents

1 Introduction

Our knowledge of the Universe has been largely widened over the last decade. The satellites WMAP (Wilkinson Microwave Anisotropy Probe) in 2003 [75] and Planck in 2013 [4] represent major steps in the understanding of physics phenomena. In particle physics, the Standard Model (SM) has demonstrated huge successes in providing experimental predictions [16]. Nevertheless, many questions are still to be answered, making searches beyond the SM necessary. It is in this context that a Weakly Interacting Slim Particle (WISP) model arose. In the following chapter, the WISP model, its motivations and the different detection principles will be discussed (see Sec. 1.1). Finally, we will describe how Any Light Particle Search collaboration (ALPS) obtained in 2011 the best constraints on such a model for a laboratory-based experiment at that time [32, 33] and how the setup has been updated since then to continue on this path with an improved sensitivity [11] (see Sec. 1.2).

1.1 Weakly Interacting Slim Particles

The Weakly Interacting Slim Particles (WISP) family could bring answers to some of the most burning physics questions in the 21st century going from the nature of dark matter to the resolution of the Strong CP Problem (see Sec. 1.1.1). Its most famous candidate, the axion, emerged in 1978 in order to solve the Strong CP Problem in QCD [88, 86]. Later, other members have been added to the family. Nowadays, the WISPs group consists of many more particles such as Axion-Like Particles (ALPs), Hidden Photons (HPs) or Mini Charged Particles (MCPs) [49, 54]. It is important to underline the fact that each of these hypothetical particles taken separately is only supported by a fraction of the general WISPs motivations (see Tab. 1.1).

WISPs can be divided into two categories. Some WISPs have the same quantum numbers as photons, which will allow kinetic mixing with photons (e.g. hidden photons), while others, pseudo-scalar or scalar bosons, will require two-photon interactions (e.g. ALPs). This will be an essential parameter for WISP detection (see Sec. 1.1.2).

	Neutrino	**Axion and ALPs**	**HP**	**Chameleons**
	Fermions	Pseudo Goldstone bosons	Gauge bosons	Scalars
DM	✓	✓	✓	
CP		✓		
Astro		✓		
DE				✓

Table 1.1: WISPs and their main motivations - WISPs include particles from the Standard Model (e.g. neutrino, graviton) and from beyond the Standard Model (e.g. ALPs, hidden photons (HP), mini charged particles (MCP) and chameleons). WISPs could be a constituent of Dark Matter (**DM**) as well as of Dark Energy (**DE**). They could solve the strong CP problem (**CP**). Moreover, they could solve various astrophysical problems (**Astro**) (see Sec. 1.1.1). MCPs as well as gravitons have not been depicted in this table as they are not considered as solutions of the hereby listed problems.

1.1.1 WISP motivations

The main motivations for WISPs search are the possible solutions that these new particles could offer to various physics questions such as "What is Dark Matter made of ?". A description of these motivations can be found in the following part.

Strong CP problem

At Brookhaven International Laboratory, in the summer of 1964, results of an experiment studying neutral kaons showed that the long-lived neutral kaons can decay in two pions [22]. This news came as a big surprise as it implied the violation of the CP (Charge conjugation parity) symmetry in the weak interactions and therefore a clear physics distinction between particles and antiparticles.

According to Quantum Chromodynamics (QCD), CP symmetry could also be violated in the strong interactions (see Eq. 1.1). However, this violation has not yet been experimentally demonstrated. Measurements of the neutron electric dipole moment result in much smaller values than what would be expected in the case of a violation of the CP symmetry in strong interactions [61]. This unsolved problem has been named *Strong CP Problem*.

$$\mathcal{L}_{QCD} = \underbrace{-\frac{1}{2}Tr(G_{\mu\nu}G^{\mu\nu})}_{Gluon\ dynamics} + \underbrace{\bar{\psi}(i\gamma^{\mu}D_{\mu} - me^{i\theta'\gamma_5})\psi}_{Kinetic\ and\ masses\ quark\ terms} + \underbrace{\Theta\frac{g^2}{32\pi^2}G^a_{\mu\nu}\tilde{G}^{\mu\nu a}}_{CP\ violating\ term} \quad (1.1)$$

A solution to this problem was proposed in 1977 and is now known as the Peccei-Quinn symmetry [60]. A few months later, it was shown that the breaking of this chiral symmetry resulted in the apparition of a new pseudo-Nambu-Goldstone boson called the axion [88, 86] (see Eq. 1.2). The original axion model has been experimentally ruled out very quickly but other younger axion models are still viable (e.g. Kim-Shifman-Vainstein-Zakharov (KSVZ) hadronic models [50], Dine-Fischler-Srednicki-Zhitnitskii (DFSZ) GUT models [90, 27]).

$$
\mathcal{L}_{QCD} = -\frac{1}{2} Tr(G_{\mu\nu} G^{\mu\nu}) + \bar{\psi}(i\gamma^\mu D_\mu - m e^{i\theta' \gamma_5})\psi
$$
$$
+ \underbrace{(\Theta - \frac{a}{f_a})\frac{g^2}{32\pi^2} G^a_{\mu\nu} \tilde{G}^{\mu\nu a} + \frac{1}{2}\partial_\mu a \partial^\mu a}_{Axion\ components} \tag{1.2}
$$

with $\Theta = \frac{a}{f_a}$, a being the axion field and f_a the axion decay constant also called the Peccei-Quinn breaking scale.

The axion mass m_a as well as the strength to its coupling to Standard Model particles g_a are inversely proportional to f_a. The mass of the axion can be expressed as:

$$
m_a \approx \frac{m_\pi f_\pi}{f_a} \approx 1\ meV \times (\frac{10^{10}\ GeV}{f_a}) \tag{1.3}
$$

where $m_\pi = 135\ MeV$ is the pion mass and $f_\pi \approx 92\ MeV$ is the pion decay constant[1]. Axion can couple to photons, electrons and nucleons [9]. The coupling values are model-dependent.

Universe composition

The study of our Universe history is at the heart of contemporary physics. One model was able to stand out, supported by many observational works. According to this model, an electromagnetic radiation has been created from a dense and hot era also known as the Big Bang. In 1965, this Cosmic Microwave Background (CMB) was discovered with a temperature as mea-

---

[1]Axions have a characteristic two-photon vertex inherited from their mixing with π^0 and η through the Primakoff effect.

sured today to be of $T_0 = 2,7255 \pm 0.0006\,\mathrm{K}$ [62, 36]. Its study has become one of the biggest priorities as it makes it possible to obtain the cosmological parameters, simple numbers allowing us to describe the Universe properties such as its expansion velocity or even its composition [59].

In the last forty years, many satellites[2] have been sent to space in order to study the CMB more precisely [74, 75, 4]. In particular, WMAP determined that the Universe is flat by measuring the small angular anisotropy. From these observations and the study of the Big Bang nucleosynthesis, it was concluded that the Universe is constituted of 68,5 % of Dark Energy, 26,6 % of Dark Matter and finally 4,9 % of baryonic matter. We can see here that the total matter density is not equal to the baryonic matter density even if the latter composes all the visible structures of our Universe. This is a serious hint for a new type of matter which has still not been identified in nature and is currently called Dark Matter as it interacts only very weakly with matter, making it non visible.

Even if today a lot of observations have been made which demonstrate the existence of Dark Matter, it has not always been the case. In 1933, the Swiss astronomer Fritz Zwicky, while observing the Coma cluster, got surprised by the relative dispersion of the galaxies [91]. In the 70's, the American astronomer Vera Rubin confirmed his observations by studying, this time, stars rotation velocity in the spiral galaxies. According to Newtonian mechanics laws, the rotation velocity of an object decreases when the distance to the rotation center increases. We then expect to obtain $v(r) \propto 1/\sqrt{r}$. However, computations based on her observations were pointing to an approximate constant velocity. This result implies the existence of a dark matter halo with a mass density of $\rho(r) \propto 1/r^2$, and it is then obtained that $v(r) \propto \sqrt{M(r)/r}$ where $M(r)$ is the mass within an orbit [70].

The second experimental observation validating the existence of Dark Matter is the gravitational lensing effect [34]. This light rays deflection phenomenon, which gives birth to gravitational arcs, occurs when two objects get perfectly aligned. It was predicted by the General Relativity theory and was observed by the Hubble telescope. Gravitational fields of massive objects bend the space-time inducing a modification of the photon trajectory. The study of such a curvature allows to determine the total mass of the body causing gravitational fields. By measuring the visible quantity of mass, it is then possible to demonstrate the existence of missing mass.

---

[2]WMAP, COBE and Planck

Before its exclusion, the hypothesis stating that Dark Matter is a particular form of ordinary matter was the most natural one. Over time, many different solutions were proposed before in turn being excluded by observations. A very long list of hypothetical non-baryonic particles is born with some of them more probable than others.

In the end, every candidate must fulfill three criteria in order to correspond to theory as well as to observations. Firstly, if Dark Matter really is a new particle, it has to be relatively stable as it is one of the Universe compounds since the Big Bang. Secondly, following observations, it cannot emit light which means that it interacts only very weakly with known matter. Finally, it needs to be heavy enough to have been not relativistic while structures started condensing. Indeed, cosmologists think that the fluctuations of non-baryonic matter have induced fluctuations of the gravitational potential, increasing baryonic fluctuations and resulting in the formation of condensed objects: the galaxies.

Cold Dark Matter is decomposed in different types of particles depending on their source process. If the supersymmetric Weakly Interacting Massive Particles (WIMPs) have represented the major part of Dark Matter research in the last ten years, the tendency has now changed. Indeed, another serious hypothetical particle family has arisen and is gathering more and more voices. In the early Universe, WISPs would have been produced in phase transitions and would have composed very Cold Dark Matter in spite of their low mass [7].

Astrophysical hints

Some astrophysical results are synonyms for hints for WISPs particles. Two examples of these astrophysical hints will be briefly discussed: the transparency of the Universe to TeV photons and the cooling of the stars.

TeV transparency - It is expected for the Universe to be not fully transparent to photons with an energy $\geq$ TeV. Indeed, these high energy photons are expected to scatter on the extragalactic background light. However, we have observed that the Universe is more transparent to this light than expected. This TeV transparency of the Universe could be explained by an hypothetical conversion of the photons into ALPs when being under the influence of the extragalactic magnetic field due to the Primakoff effect [24].

Cooling of the stars - Many stellar systems have been studied and it has

been shown that for some of them (e.g. white dwarfs, red giants) a non-standard cooling mechanism is preferred to theoretical models [38]. This phenomenon could be explained by WISPs being produced in the hot cores. Indeed they would contribute to the stars' energy loss. Simulations have been performed and it has been demonstrated that this observation represents a serious hint in particular for axion-like particles.

1.1.2 Detection principles

Nowadays, the Primakoff effect plays a key role in main axion searches [63]. In the case of the ALPS experiment, the phenomenon of interest is the coupling of axion to photon. When photons traverse an electromagnetic field they can convert into axions. The effective Lagrangian of the photon-axion coupling is expressed as:

$$\mathcal{L}_{a\gamma\gamma} = -\frac{g_{a\gamma\gamma}}{4}(F_{\mu\nu}\tilde{F}^{\mu\nu}a) = g_{a\gamma\gamma}a\vec{E}\cdot\vec{B} \tag{1.4}$$

with $F_{\mu\nu}\tilde{F}^{\mu\nu}$ the electromagnetic field tensor and its dual, a the axion field and $g_{a\gamma\gamma}$ the axion-photon coupling constant [11].

There are three main experiment types currently exploiting this phenomenon (see Tab. 1.2). The helioscope is a principle looking for solar axions and ALPs. The haloscope concentrates on direct detection of Dark Matter WISPs. Finally, the Light-Shining-through-a-Wall (LSW) concept is a principle where WISPs are produced as well as regenerated into photons for detection. This final principle is the concept followed by the ALPS experiment. Each experiment type will be discussed in the following subsections.

Haloscope	Helioscope	LSW

→ Dark Matter WISPs	→ WISPs produced in the Sun	→ WISPs
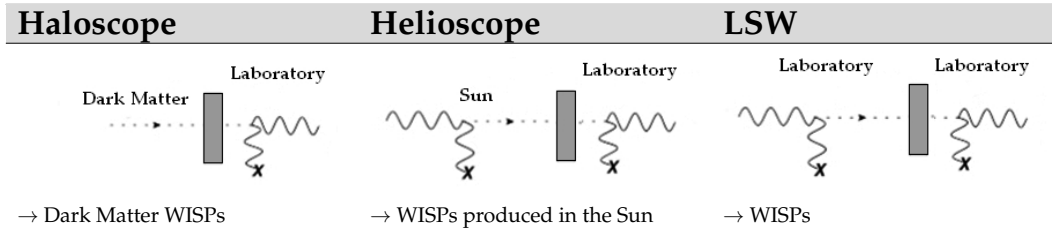
Table 1.2: The three main detection techniques currently used in order to search for WISPs (LSW stands for Light-Shining-through-a-Wall).

Helioscope

Helioscopes are designed to attempt the observation of the flux of WISPs generated in the Sun and propagating to Earth. Different WISPs could be produced in the Sun. The experiment is based on the Primakoff effect. Axions might be produced in the Sun through the electron decay into photons. The first experiment of this type was called Brookhaven [80]. The idea proposed was to use the inverse Primakoff effect by using a magnetic field in order to catalyse the conversion of solar axions back into photons (X-ray of a few keV). Many experiments have now followed this principle and the best constraints were obtained a few years ago by the experiment CAST (CERN Axion Solar Telescope). With the CERN powerful magnets (10 m long and 9 T field), CAST obtained a conversion factor 100 times better than the previous generations of experiments [10]. The magnet is mounted on a tilted platform. This setup allows to observe the Sun during one hour and a half at dawn and at twilight. It is able to move in order to follow the azimuthal motions of the Sun during almost the full year. When the Sun is not visible, the measuring time is used to study the background. Photon detectors are installed on both sides of the magnet.

Haloscope

This type of experiment is based on a possible abundance of Dark Matter composed of WISPs all around us. The aim is to exploit their coupling to ordinary photons which can be detected. Dark Matter WISPs can be considered as monochromatic. As a consequence, the energy will be dominated by the mass. The conversion of such WISPs into photons can be made more efficient by employing a resonator having peak response at a frequency corresponding to the energy of the produced photons, which is in turn equal to the mass of the incoming WISPs.

The most famous haloscope is Axion Dark Matter Experiment (ADMX) focusing on the detection of Dark Matter axions conversion into microwave photons [81]. The conversion is stimulated by an 8 T magnet and a cryogenically cooled microwave cavity. When the resonance frequency of the cavity corresponds to the axion mass, the interaction between the Milky Way axion and the ADMX magnetic field starts. In a nutshell, the aim is to test every resonance frequency of the cavity for different axion masses.

Light-Shining-through-a-Wall

The Light-Shining-through-a-Wall principle (LSW) has the advantage of allowing a complete control of the coupling process. Indeed, WISPs would be produced as well as converted back inside the laboratory. In the case of the ALPs search, a powerful laser is directed towards a light-tight barrier. The beam is surrounded by magnets in order to induce the coupling of two photons to produce a WISP. These weakly interacting particles would then traverse the wall and might reconvert when passing through a magnetic field located downstream of the barrier. WISPs detection will be done through photon detection. The regenerated photons are expected to have the same energy as the laser used to generate the original photon beam.

LSW experiments represent a technical challenge because of the small expected detection rate (i.e. one photon every few hours). The probability of conversion inside a magnetic field B of a length L is of [8]

$$P_{a \leftarrow \gamma} \approx \frac{\omega}{4k_a}(g_{a\gamma}\mathrm{BL})^2 \mid F \mid^2 \approx P_{a \rightarrow \gamma} \tag{1.5}$$

with $k_a{}^2 = \omega^2 - m_a{}^2$ where ω is the energy of the photon. The form factor F is such that $\mid F \mid \leq 1$ in the case where the magnetic field is homogeneous. The magnetic length is an essential parameter in the upgrade of a LSW setup.

1.2 ALPS II experiment

ALPS II experiment is a light-shining-through-a-wall setup located at the heart of the Deutsches Elektronen-Synchroton (DESY) in northern Germany (see Sec.1.1.2). This experiment aims to detect photon oscillations into WISPs (see Sec.1.1). In 2010, ALPS I came to an end with the world's best constraints that had been obtained at that time for axion-like particles and hidden photons [32, 33]. Since then, the collaboration has been developing a second phase of the experiment, ALPS II [11]. As shown on figure 1.1, the ALPS I concept included a green laser, an optical cavity, one HERA dipole as well as a photon detector (i.e. a CCD camera). The experimental area was 10 meters long at that time.

ALPS II will go through two different measurement phases. ALPS IIa will look for hidden photons and should start in 2017. A second optical cavity

has been added after the wall in order to improve the sensitivity to hidden photons (see Eq. 1.6). The second phase is called ALPS IIc and is foreseen for 2019. With this final ALPS II development, it will be possible to look for axion-like particles. In this phase of the experiment, QCD axions' region of interest will not be reachable (see Fig. 1.2).

The ALPS IIc experiment will be constituted in the same way as ALPS IIa with two 100-meter-long cavities and the addition of 20 HERA (Hadron-Electron Ring Accelerator) dipoles [11]. The magnets were all bent during their design what led to a reduction of their aperture (i.e. 35 mm). It is foreseen to unbend all the dipoles by applying a force in their middle (cold mass). The procedure has already been successfully followed. Indeed, in addition to reaching a final aperture of 50 mm, the dipole has even demonstrated a slight increase of its quench current [79].

The ALPS experiment sensitivity to the conversion of photons into axion-like particles depends on various parameters and is expressed as [83]

$$S(g_{a\gamma}) \quad \propto \quad \left(\frac{1}{\mathrm{BL}} \right) \left(\frac{\mathrm{DC}}{\mathrm{T}} \right)^{\frac{1}{8}} \left(\frac{1}{\eta \dot{N}_{\mathrm{Pr}} \mathrm{PB}_{\mathrm{PC}} \mathrm{PB}_{\mathrm{RC}}} \right)^{\frac{1}{4}} \qquad (1.6)$$

with a strong dependency on the magnetic length L and field B. The effect of the optical setup depends on $\dot{N}_{\mathrm{Pr}}$, the number of injected photons as well as on $\mathrm{PB}_{\mathrm{PC}}$ and $\mathrm{PB}_{\mathrm{RC}}$, the power build-ups of the production (PC) and regeneration cavities (RC) (see Sec. 1.2.1). Finally, the reached sensitivity depends on the total detection efficiency η and on the chosen detector's dark current (DC). The data-taking time is expressed as T.

The ALPS II experiment aims for an increase of the sensitivity to the axion-photon coupling by a factor of 3000 compared to what was obtained in the past. This upgrade will allow the scanning of the axion to photon coupling to three additional orders of magnitude.

1.2.1 Optical setup

The ALPS IIa (search for hidden photons) optical setup includes two 10-meter-long optical cavities separated by a light-tight barrier. Both optical cavities are placed in vacuum (10^{-6} mbar). A 30 W 1064 nm Master Oscillator Power Amplifier (MOPA) laser is injected inside the first cavity[3]. Such an

---

[3]The green laser has been replaced by an IR laser to avoid damages of the mirrors coating.
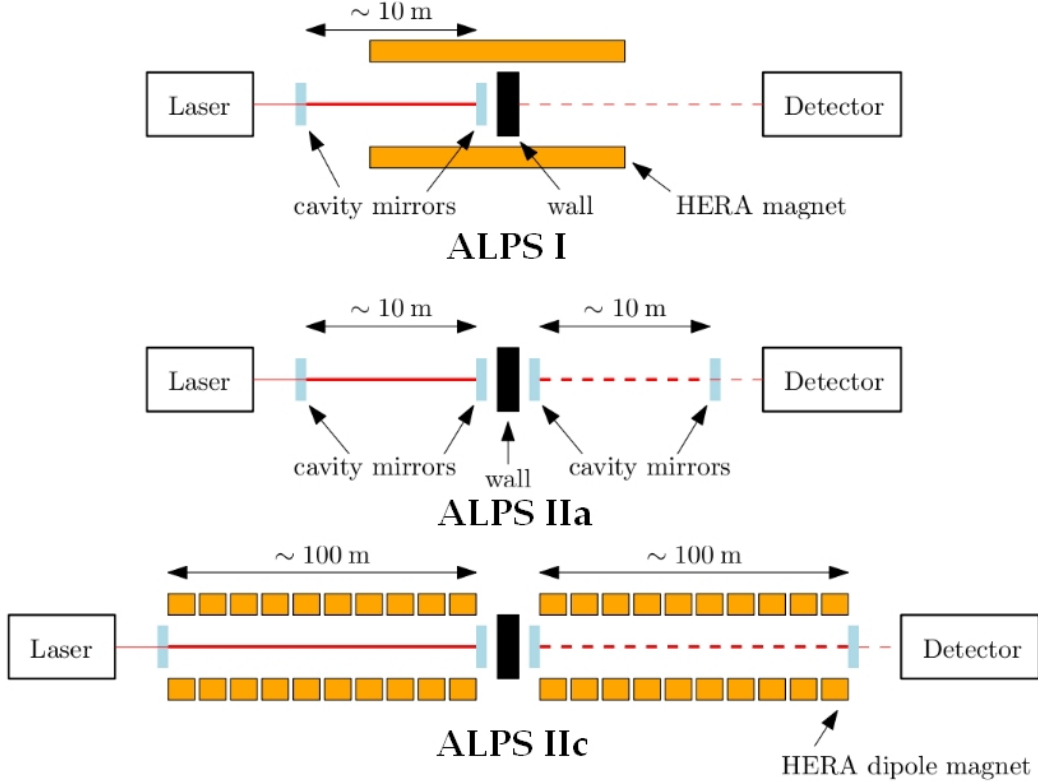
Figure 1.1: The different phases of the ALPS experiment including ALPS I and ALPS II. If the magnets are removed (e.g. ALPS IIa) it is possible to look for products of kinetic mixing (e.g. hidden photons). Magnets are necessary for the search of pseudo-scalar or scalar bosons (e.g. ALPs) as they request a two-photon interaction. ALPS IIb was cancelled in 2015. (Source: [11])

optical system is technically challenging [44]. An alignment of both cavities towards each other is necessary to provide a large spatial overlap of their modes. Moreover, high power buildups (PB) are required for both cavities in order to reach the ALPS IIa foreseen sensitivity. It is expressed as:

$$PB = \frac{F}{\pi} \qquad (1.7)$$

with F the finesse of the mirrors which is an expression of their reflectivity. The optical loss of the ALPS mirrors is a critical parameter that can be measured using a cavity ring-down technique [48]. In order to maximize the PB, the production (PC) and regeneration cavities (RC) need to be in the same modal phase with a mode-overlap of 95 %. The RC is locked via an auxiliary green beam obtained via second harmonic generation (KTP crys-
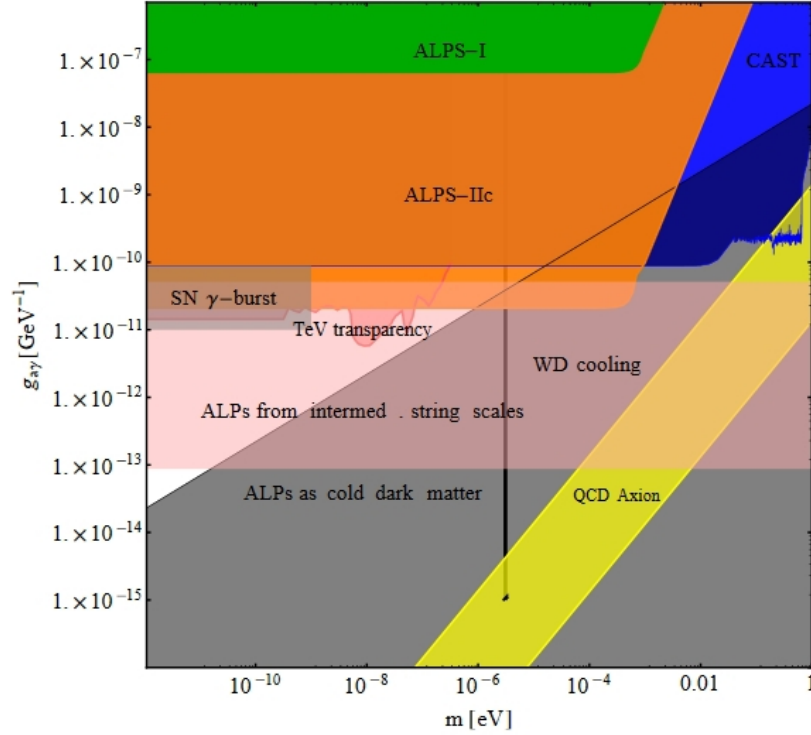
Figure 1.2: ALPS parameter of space - The coupling of the axion to photon expressed as a function of the axion mass. The region in green represents the parameter of space probed by ALPS I and the orange region represents the ALPS IIc aim. In blue, we can see the region probed by CAST (see Sec. 1.1.2). The diagonal yellow region represents the parameter of space where ALPs would correspond to the QCD axion. The grey area defines the region which would correspond to ALPS as Cold Dark Matter. Different hint regions as discussed in 1.1.1 are also depicted (i.e. TeV transparency and white dwarf cooling) as well as the Supernova γ-burst exclusion region. (Source: [11])

tal) of the PC infrared beam [44]. The aimed PB of the production cavity is of 5 000 and the aimed regeneration cavity PB is of 40 000.

The regeneration cavity will be connected via a fiber to a single-photon detector in order to spot possible regenerated photons. Efficient coupling of a $4.23\,\text{mm}$ beam inside a $8.2\,\mu\text{m}$ single-mode fiber represents a challenge. A free space to fiber coupling setup has already been implemented allowing for a coupling efficiency of up to $90\,\%$[4] [87].

---

[4]Test performed with a SM980 fiber.

1.2.2 Single-photon detector setup

The ALPS single-photon detector has many challenges to overcome (see Tab. 1.3) [11]. Indeed, the low energy of the photon (i.e. 1.17 eV) and the low expected rate (i.e. one photon every few hours) lead to very demanding specifications. The two most important parameters are the detection efficiency (DE)[5] of the detector (see Chap. 4) as well as its dark count rate (DC) (see Chap. 5). Good energy and time resolutions are also required as well as a long-term stability (see Chap. 3) .

The ALPS I photon detector was sufficient for the first stage of the experiment with its near to unity quantum efficiency (QE) for 532 nm photons and its dark current of 10^{-3} e$^-$/pixel/sec. Unfortunately this CCD camera[6] is not meant for infrared light. At 1064 nm, the efficiency falls to 1.2 % due to the proximity of the wavelength to the Si band gap energy. The detector had to be replaced in order to reach the ALPS IIc expected sensitivity [83].

The choice was made to use a Tungsten Transition-Edge Sensor (W-TES) developed by the National Institute of Standards and Technology (NIST). NIST has demonstrated that such a detector can reach quantum efficiency higher than 95 % [51]. We have measured a DC as low as 10^{-4} evt/sec [30]. Superconducting QUantum Interference Device (SQUID), produced by PTB (Physikalisch Technische Bundesanstalt), plays the role of the read-out system.

Properties	CCD	TES
QE for 1064 nm	1.208 ± 0.002(stat) ± 0.079(syst) % [83]	$> 95\%$ [51]
DC	10^{-3} e$^-$/pixel/sec [83]	10^{-4} evt/sec [30]
Energy resolution	-	8 % [30]
Time resolution	-	50 ns [30]
Long-term stability	✓ [83]	✓ [30]

Table 1.3: Towards ALPS IIc - Detector challenges versus detector characteristics. For more details on these topics see chapters 3, 4 and 5.

Transition-Edge Sensor

Transition-Edge Sensors are superconductive microcalorimeters measuring the temperature difference ΔT induced by the absorption of a photon with

---

[5]DE is the detection efficiency of the detector setup and η is the total detection efficiency of the experiment including the efficiency of the free space to fiber coupling setup.
[6]Pixis 1024B CCD camera
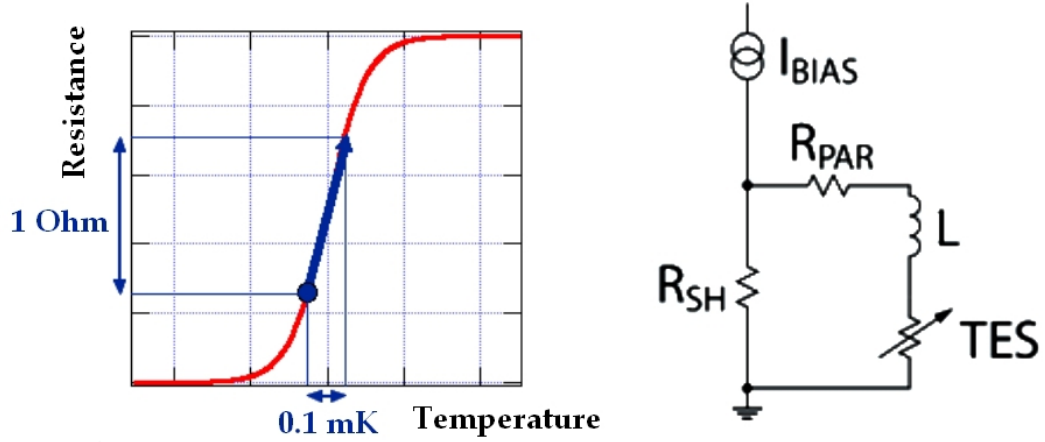
Figure 1.3: TES working principle - On the left, the resistance of the TES is expressed as a function of the temperature (Inspired by [3]). The TES is biased so that its resistance is of 30% of its normal resistance. On the right the TES electrical circuit is given following [46]. I_{bias} corresponds to the TES bias current. R_{SH} is the shunt resistance and R_{PAR} is the parasitic resistance of the TES circuit.

R(T,I) the resistance. The detector is positioned within its superconductive transition through a thermal link to a heat bath at $T_b = 80\,\text{mK}$ and by applying a constant bias voltage across the TES (see Fig. 1.5). In order to obtain the cool-down of the detector, it is placed in an Adiabatic Demagnetization Refrigerator (ADR) (see Chap. 2).

When a 1064 nm photon is absorbed by the tungsten chip, the sensor temperature rises by 0.1 mK (see Fig. 1.3). The heating of the detector brings it from its working point to close to its normal resistive stage with an increase of the resistance of $\Delta R \approx 1\,\Omega$. This is caused by:

$$
\begin{cases}
I_{bias} & = \quad \text{constant} \quad \text{Bias current of the TES} \\
R_{TES\ branch} & = \quad R_{TES} + R_{PAR} \quad \text{Resistance in the TES branch} \\
\frac{R_{TES\ branch}}{R_{SH}} & = \quad \frac{I_{bias}}{I_{TES}} - 1
\end{cases}
$$

$$
\Rightarrow \quad R_{TES\ branch} \uparrow \ \Leftrightarrow \ I_{TES} \downarrow
$$

This leads to a decrease of the current in the TES electrical circuit with $I_{TES} \approx 70\,\text{nA}$ (see Fig. 1.5). The inductively coupled SQUID converts this current variation in a voltage difference of $\Delta V \approx -50\,\text{mV}$.

The TES will slowly thermalise back to T_b thanks to the negative electro-

thermal feedback [47], following this:

$$
\begin{cases}
\mathrm{V} &= \text{constant} \\
\mathrm{P}_{J,0} &= \mathrm{V}^2/\mathrm{R}_0 = \mathrm{P}_{bath} \quad \text{Joule power of the TES at t} = 0 \\
\mathrm{P}_J &= \mathrm{V}^2/\mathrm{R} \neq \mathrm{P}_{bath}
\end{cases}
$$

$$
\mathrm{R} \uparrow \ \Rightarrow \ \mathrm{P}_J \downarrow \ \Rightarrow \ \mathrm{T}_{TES} = \mathrm{T}_{bath}
$$

More detailed information on Transition-Edge Sensors can be found in [46]. For more details about ALPS II TES detectors look at [29].

Superconducting QUantum Interference Device

A Superconducting QUantum Interference Device is a magnetometer used to measure very small magnetic fields. Each SQUID is constituted of two parallel Josephson junctions placed in a superconducting loop. The ALPS II SQUID chips have been developed by PTB and are used in ALPS II experiment as linear transducers of current to voltage [31].
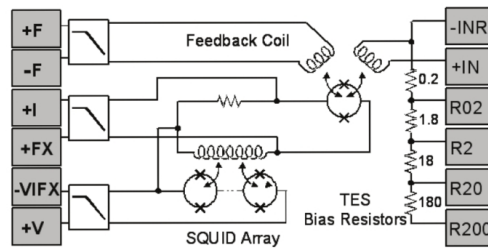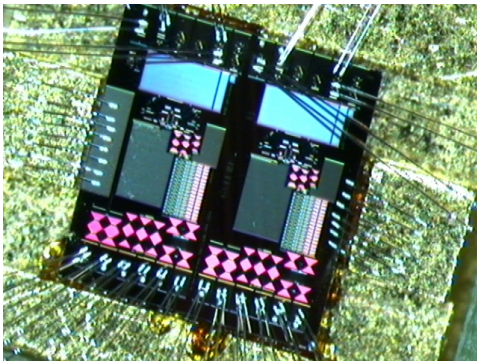
Figure 1.4: SQUIDs chip - On the left, a picture of the ALPS SQUID chip taken with a microscope. One SQUID chip includes two double-stage SQUIDs (see Fig. 2.16 for close-up). On the right, the drawing of one double-stage SQUID circuit (source PTB).

Each C6X114HW SQUID chip consists of a front-end SQUID (SQ1) followed by a SQUID Series Array (SSA) including 16 devices and playing the role of an amplifier. Both stages are made of niobium (Nb), which acts as a type II superconductor with a transition temperature of $Tc_1 = 9.3$ K.

More information about SQUIDs can be found in [23].

(a)

(b)

(c)
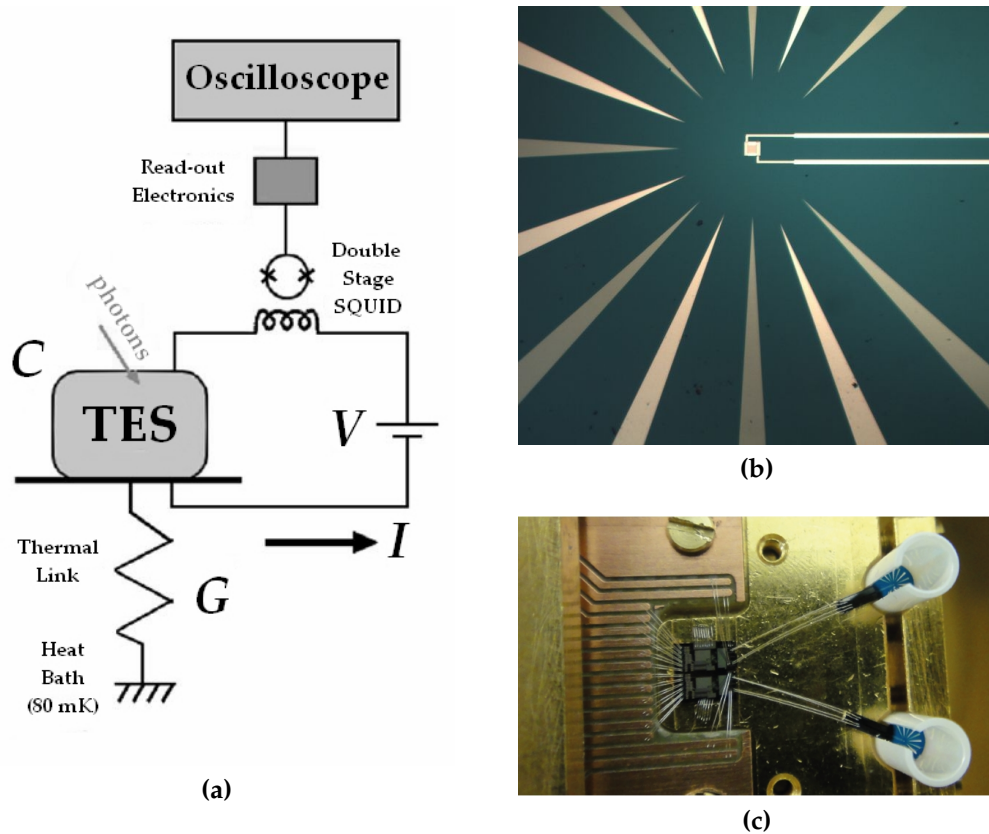
Figure 1.5: Transition-Edge Sensor in ALPS 2 - (a) The detector is coupled to a 80 mK heat bath. G is the thermal conductance of the thermal link. C is the heat capacity of the absorber (i.e. the TES). The change in current in the TES circuit will be read by the double stage SQUID. The oscilloscope plays the role of DAQ (Data Acquisition) system.

(b) Picture of the TES detector taken with a microscope. The blue surface is the Si substrate. The white track are acting as eye-guides. The squared tungsten sensitive region is surrounded by the aluminium wire connected to the SQUID.

(c) The ALPS II detector module is constituted of two TESs coupled to a SQUID. Both detectors are $25 \times 25\ \mu\mathrm{m}^2$ large and 20 nm thick. A ceramic standard mating sleeve towers above each detector, allowing coupling of a standard single-mode fiber.

This thesis deals with the characterization and optimization of the ALPS II detector setup as well as the study of its background. It is divided in five different parts:

- In chapter 2, a description of the ALPS II cooling system can be found. An important optimization work has been accomplished in the framework of this thesis. The details of the system upgrade will be described and the results discussed.

- Chapter 3 describes the detector response to 1064 nm photons. In addition, a detailed discussion concerning the detection stability of the TESs can also be found in this chapter.

- Chapter 4 details measurements and analysis regarding the detection efficiency of ALPS II experiment.

- Chapter 5 focuses on the study of the different background sources for the ALPS TES detector.

- Finally, Chapter 6 brings ideas together thinking about towards as well as beyond ALPS IIc.

2 ALPS cooling system and optimization

The cooling system used to maintain the ALPS detector at 80 mK is an essential part of the detector setup. Indeed, the ALPS II single-photon detector is a Transition-Edge Sensor (TES), superconductive microcalorimeter which requires a low temperature environment. ALPS collaboration chose an Adiabatic Demagnetization Refrigerator (ADR) purchased from Entropy GmbH[1] and optimized in the last years for the ALPS experiment. The full ALPS cooling system is divided in two different cooling levels.

The primary cooling system makes possible to reach a **temperature baseline** of approximately 2.5 K for an extended period of time called a **cooldown**. It is based on a He-compressor attached to a pulse-tube cooler. The secondary cooling system will enable the colder stages to reach temperatures as low as 80 mK for a period of approximately 24 hours (i.e. a **recharge**). Each cool-down can include many recharges.

In the following chapter, each part constituting the cooling system will be examined. In a first section, the primary cooling system will be described and parts which were optimized will be discussed in detail. In a second section, the ADR and its upgrades will be reviewed.

2.1 Primary cooling system

The heart of the primary cooling system is a F-50H Sumitomo helium compressor. Its aim is to produce compressed He-gas. It is made up of three main circuits: the water circuit, the oil line and the helium-gas circuit (see Fig. 2.1). Experience has shown that the influence of the compressor status on the temperature baseline is very high (see Sec. 2.1.1).

---

[1]GmbH is a German acronym which stands for Gesellschaft mit beschränkter Haftung and can be translated in English by "company with limited liability".

Cold and low-pressure He is sent from the cryostat to the compressor. It will be compressed in the compressor capsule. The process will dramatically heat up the He which will need to be cooled down before going back to the cryostat. In order to do this, the compressor is equipped with a water-helium heat-exchanger. The compressor capsule is also attached to an oil-line. Indeed, the mechanical parts used in the compression process require constant lubrification. As the process will also heat-up the oil, this one has to go through a water-oil heat-exchanger for cooling. Finally, compressed and cooled helium will be sent back to the cryostat after being filtered multiple times for oil contaminant. The adsorber is a coal filter and represents the final filtering step [52].
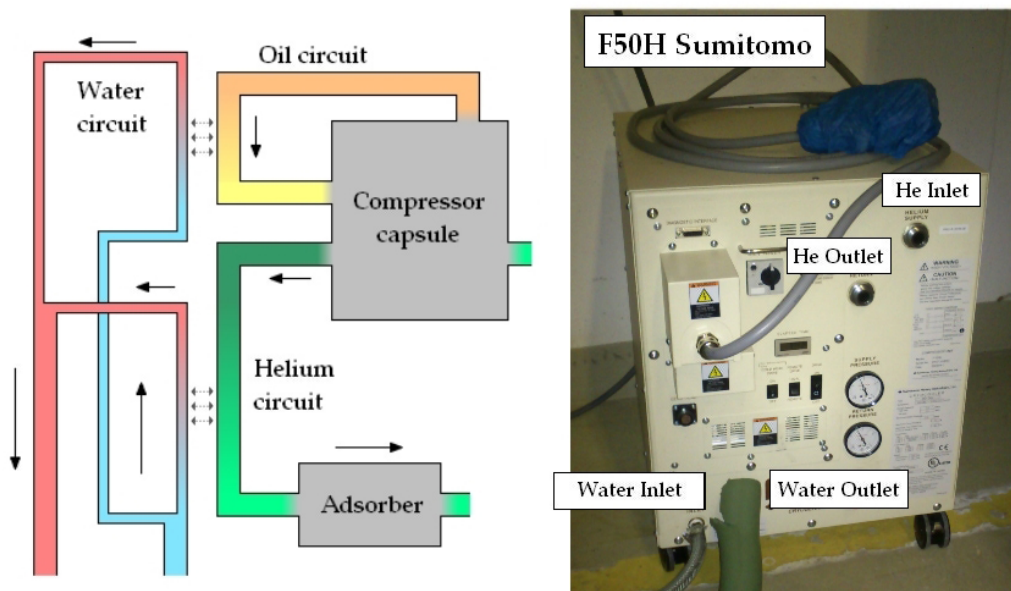
Figure 2.1: F-50H Sumitomo compressor simplified drawings and picture - On the picture, both He lines are missing. The place where the supply and return lines should be connected is indicated.

The full primary cooling system is shown on figure 2.2. Upstream the compressor, a custom-made air-water chiller cool-downs the water to a stable temperature of 15 °C. This part of the circuit has required intense upgrades and improvements from the second half of 2014 until January 2015 (see Sec. 2.1.1).

Downstream the compressor, the He-lines are connected to a valve unit (i.e. a rotary valve) which includes a stepper motor as well as a Rulon® cylindrical piece. Finally, the helium cooling circuit is finished by a RP-062

Sumitomo two-stage pulse-tube cooler. Its first stage has a cooling power of up to 30 W at 65 K and its second stage goes up to 0.5 W at 4.2 K [53] (see Fig. 2.4).
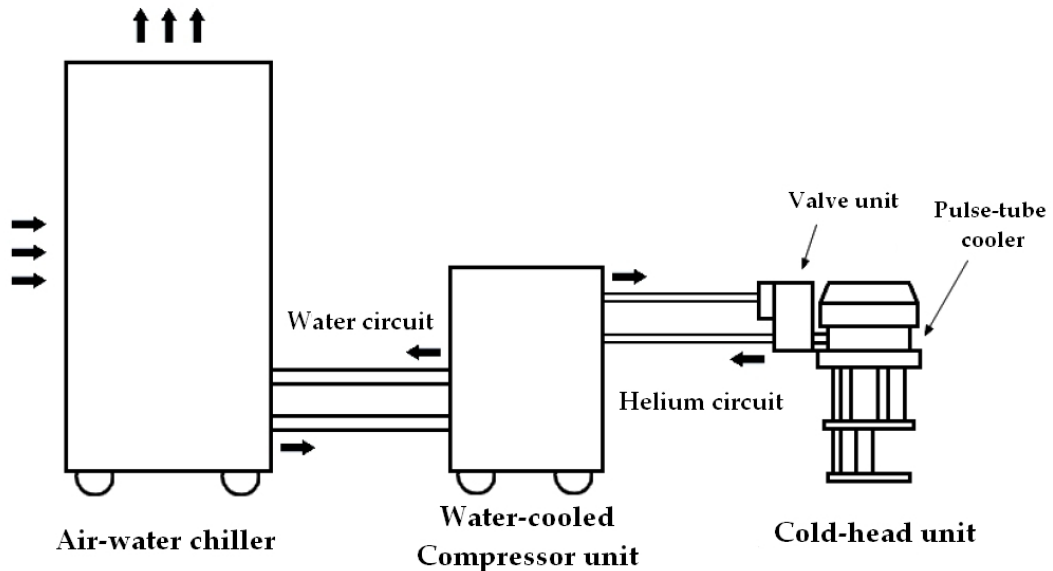
Figure 2.2: Primary cooling stage of the ALPS detector cooling system.

Pulse-tube cryocoolers are particularly good candidates for cooling down superconductive detectors. Indeed, the absence of moving parts in the cold insures a good reliability of the system and reduces vibrations at the colder stages [66, 84]. Two-stage pulse-tubes make it possible to reach temperatures as low as 2 K.

High pressure gas arrives through the helium flex-lines to the rotary valve (i.e. the so-called valve unit) which produces a pressure oscillation[2] (see Fig. 2.3). The gas goes through the regenerator where it is precooled. Regenerators are optimized for heat-transfer with a careful selection of the material and optimization of their contact surface[3]).

During a high-pressure phase, the gas is compressed in the pulse-tube, causing an increase of the gas temperature. This hot gas flows through the orifice up to the point where the equilibrium is reached (i.e. when

---

[2]Pulse-tube cryocoolers are anologous to AC electrical systems. Indeed, pressure is analogous to voltage and mass flow or volume flow is analogous to current. Following this analogy, current and voltage are in phase with each other in such devices.

[3]Regenerators are usually made of ErNi or HoCu with the shape of stacked fine-mesh screens or packed spheres

$P_{reservoir} = P_{pulsetube} = P_{average}$). The heat of the hot gas is evacuated through an air-helium heat-exchanger located on the warm end of the pulse-tube. When a low-pressure phase starts, the gas in the pulse-tube is adiabatically expanded and its temperature decreases. The gas which is located in the reservoir will move back to the pulse-tube through the orifice and will push the cold gas to the pulse-tube cold-end up to the point where the average pressure is reached again [67]. The cycle is then repeated with a frequency of 1.3 Hz. In the case of a two-stage pulse-tube cryocooler, this process is done twice following a load map that is shown on figure 2.4.

The **temperature baseline** (i.e. equilibrium temperature) that can be obtained after approximately a day of cooling is an essential parameter which will influence the hold-time at 80 mK (i.e. the data-taking time). In order to approach the best cooling performance, the temperature baseline needs to be as low as possible as well as very stable. Many issues have been encountered since the setup has been purchased from Entropy GmbH. Table 2.1 summarizes briefly the evolution of the system in the framework of this thesis. More details will be given in the following subsections.

Additional information on standard cooling performance during a cool-down in the ALPS cooling system can be found in [29].

Parameters	Before	January to June 2015	After
Temperature baseline (K)	2.5 - 4.5	2.7 - 3.3	2.5 - 2.6
Temperature shift (mK/day)	≈ 80	≈ 50	≈ 5
Hold time at 80 mK (hours)	0 - 24	8 - 16	1 - 22

Table 2.1: Evolution of the cooling performance of the ALPS detector cooling system. Before January 2015, degraded cooling performances were connected to the primary cooling circuit. After June 2015, short hold-times are due to damages on the secondary cooling system. The temperature shift corresponds to an average value for the concerned time slot.

2.1.1 Before January 2015

When the setup was first moved to Hamburg in November 2012, the compressor had been directly connected to the DESY water cooling system. Due to the ALPS laboratory location, which is at the lowest level of this general cooling system, the compressor pipes started accumulating debris coming from other experiments. Quickly, because the diameter of the compressor pipe was reduced by the deposit on its surface, the temperature baseline
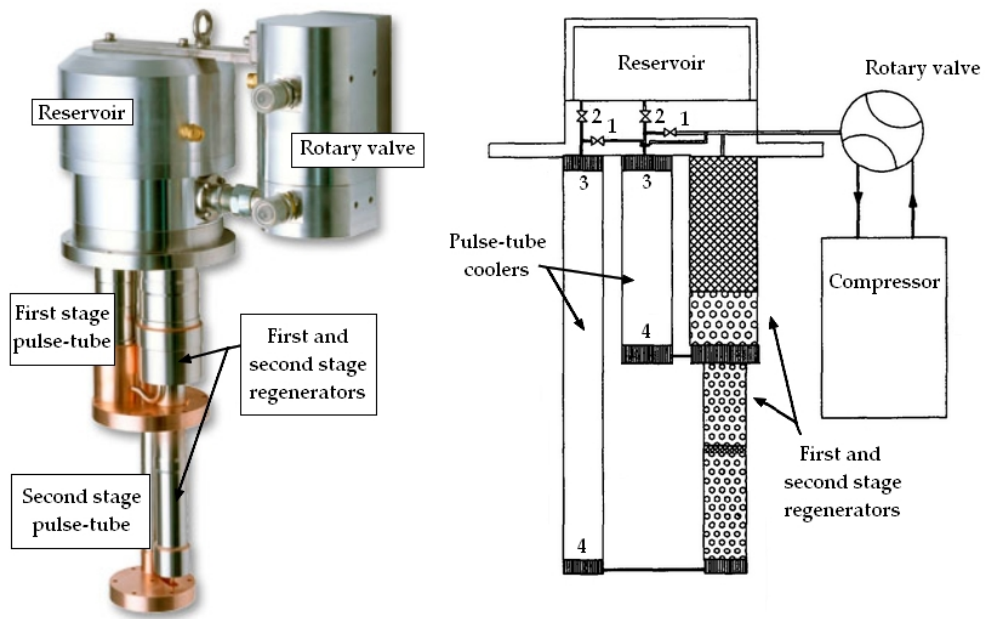
Figure 2.3: Pulse-tube cryocooler - 1) Double-inlet valves 2) Orifice valves 3) Air-helium heat-exchangers 4) Pulse-tubes cold end (Inspired by [84] and Sumitomo.)
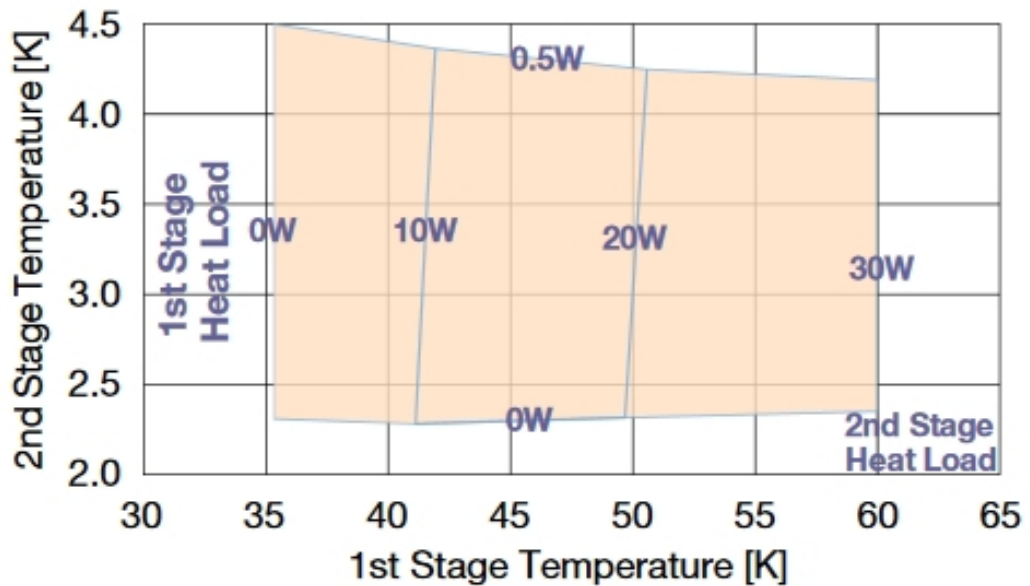
Figure 2.4: Sumitomo RP-062B pulse-tube load map (Source: Sumitomo).
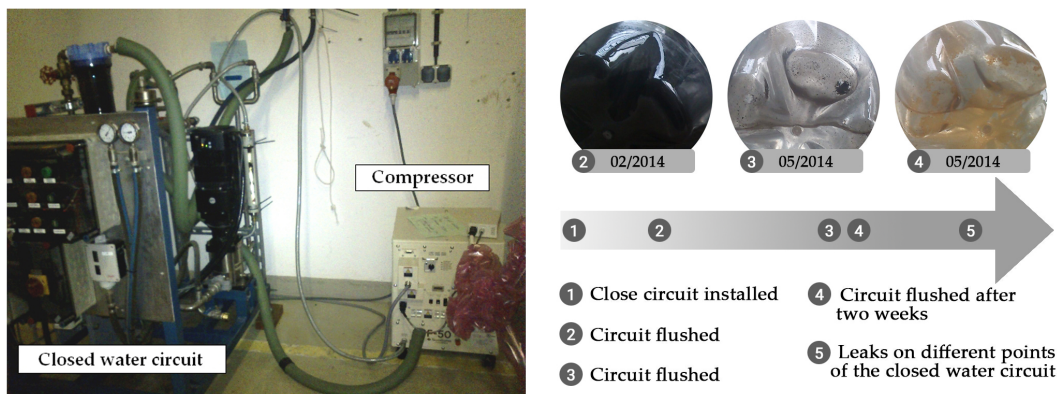
Figure 2.5: Closed cooling circuit before 2015 - On the right, the picture shows the closed cooling circuit that was installed in December 2013. On the left, the picture shows the water which was removed from the water circuit and the corresponding timeline.

increased from 2.5 to 2.9 K[4] [29]. In December 2013, decision was taken to connect the compressor to its own cooling circuit (see Fig. 2.5). The close circuit was then cooled down through a water-water heat-exchanger which was refreshed on its other side by the DESY cooling water[5]. Unfortunately, the old makeshift closed circuit did not bring the expected improvements.

After the circuit switch, the temperature baseline continued degrading. A cleaning process for the full circuit was developed in order to remove as much as possible of the remaining deposits. However, if the turbidity[6] of the water decreased, the baseline temperature remained higher than what was expected. Various issues have been hilighted and studied as discussed in the following.

Galvanic corrosion

Galvanic corrosion occurs when two different metals are connected one to each other in a water circuit. One metal becomes anodic while the other becomes cathodic [43].

The pipes of the closed circuit were constituted of steel[7]. Because some

---

[4]Temperature baseline at the beginning of a cool-down

[5]The DESY cooling system has a temperature of 8 °C.

[6]The turbidity is the measure of relative clarity of a liquid. The smaller the turbidity, the more transparent the liquid will be.

[7]Steel is an alloy of carbon (C) and iron (Fe).

28

portions of the circuit were magnetic and others were not, it was presumed to be composed of different types of steel which all have very different properties towards corrosion because of their various composition. The compressor water heat-exchanger is made of copper (i.e. internal pipes) and its connections are made of brass.

Having copper and steel in the same circuit can be an issue considering their anodic indexes[8]. The material with the lowest absolute value for their anodic index would play the role of cathode while the one with the highest value would be the anode. In order to avoid corrosion, the difference between the anodic indexes of the two materials in contact should not be higher than 0.25 V. Copper with an anodic index of -0.35 V and steel with an anodic index going from -0.5 (chromium or tin plated steel) to -1.20 V (galvanized steel) form a galvanic couple. In our case, the pipe was the anode when the compressor was the cathode (see Fig.2.6). The closed circuit pipes was then the one suffering from corrosion while some steel deposited on the copper.
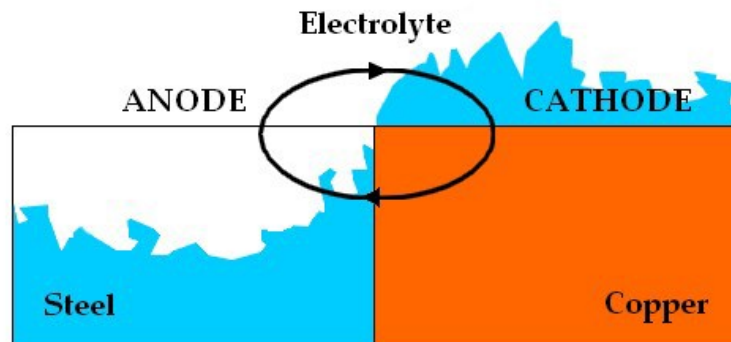
Figure 2.6: Galvanic corrosion process between steel and copper. The anode metal (i.e. steel) will dissolve inside the electrolyte and the deposit will be collected on the cathodic metal (i.e. copper). (Inspired by [1])

Corrosive bacteria

Other types of corrosion can occur. The higher the electrical conductivity, the faster the reaction will be. In the case of anaerobic corrosion of metallic iron, $Fe(OH)_2$ will be produced. Through the Schikorr reaction, $Fe(OH)_2$

---

[8]The anodic index (AI) is evaluated by measuring the free corroding potential of a metal relative to gold with gold AI=0.0 V."

will decay in Fe_3O_4 (i.e. magnetite) [71]. This black powder is very magnetic and corresponds to the dark debris that was found in big quantity inside our closed circuit in February 2014 (see Fig. 2.5).

$$Fe + 2H_2O \rightarrow \underbrace{Fe(OH)_2}_{Iron(II)hydroxide} + H_2$$

$$3Fe(OH)_2 \rightarrow \underbrace{Fe_3O_4}_{Iron(II,III)oxide} + 2H_2O + H_2$$

$$\Rightarrow 3Fe + 6H_2O \rightarrow Fe_3O_4 + 2H_2O + 4H_2$$
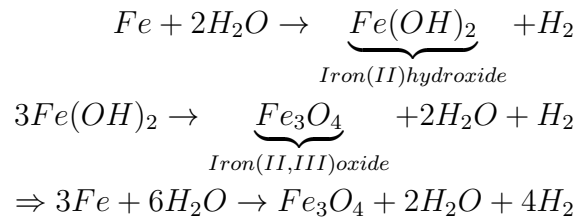
Iron bacteria colonize the transition zone which separates anaerobic from aerobic environments. When the dissolved oxygen level is low, they will reduce Fe_2O_3 (i.e. rust) in $Fe(OH)_2$ and O_2. The released oxygen will be used for further oxidations. If the water inside the circuit is changed too often, corrosion will be encouraged by an addition of dissolved oxygen inside the closed circuit. This will cause the formation of Fe_2O_3 (i.e. rust) sediments on the surface of the steel pipes. Following this mechanism, iron bacteria increase the corrosion rate [6]. Rust was found in the system in May 2014 (see Fig. 2.5) and must have been induced by the frequent cleaning of the setup.

$$H_2O + \underbrace{Fe_2O_3}_{Iron(III)oxide} \rightarrow 2Fe(OH)_2 + O_2$$

$$2Fe(OH)_2 + O_2 \rightarrow H_2O + Fe_2O_3$$
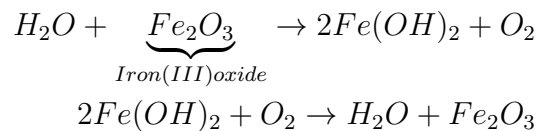
In return, if we do not change the water often enough, sulfate-reducing bacteria will develop in the circuit and might cause spectacular injuries to the pipes. Sulfate reducing bacteria [58] use sulfate from the water to produce hydrogen sulfide (H_2S, egg smell, very toxic). Hydrogen sulfide is very acidic and induces pipe corrosion.

In August 2014, it was noticed that stored samples of water were smelling like egg which gave a strong indication of the presence of sulfate reducing bacteria in the closed circuit.

Many more corrosive bacteria exist. Nitrate-reducing bacteria will transform nitrate in ammonia [78] which at a concentration higher than 1 ppm is known to create corrosion in copper alloys [68]. Sulfur-oxidizing and methanogenic bacteria (i.e. bacteria which produce methane) would also induce corrosion [72, 40].

Water characteristics

Corrosion is always the result of a combination of physical, chemical, and biological factors. Physical factors as water flow and temperature are essential. If the flow is too low (e.g. dead-ends), the corrosion rate will increase. However, corrosion by erosion can be the result of too fast a flow [15]. Copper is particularly sensitive to such phenomena. Moreover, corrosion increases with increase in temperature [28].

The corrosion rate also depends on various chemical factors such as alkalinity, hardness, electrical conductivity, dissolved oxygen concentration or the presence of sulfates and chlorides. The Sumitomo compressor comes with specific requirements in order to fight corrosion [52]. The inner copper pipes are an essential part of the circuit and cannot be replaced.

Parameters	Sumitomo requirements [52]	Hamburg tap water [85]
Temperature range (°C)	4.0 - 28.0	10.7
pH value at 25 °C	6.5 - 8.2	6.5 - 9.5
Electrical conductivity at 25 °C (mS/m)	<80	<279
Chloride Cl^- (mg/l)	<200	<250
Sulfate SO_4^{2-} (mg/l)	<200	<250
Total hardness (mg/l)	<200	263
Iron Fe (mg/l)	<1.0	<0.2
Copper Cu (mg/l)	<0.3	<2.0
Ammonium NH_4^+ (mg/l)	<1.0	<0.5

Table 2.2: Comparison of Sumitomo water requirements to Hamburg tap water quality.

In table 2.2, Sumitomo water requirements have been compared to the water quality that was used up to January 2015 (i.e. Hamburg tap water). One can see that the drinking water reglemention is most of the time too permissive when it comes to closed circuit applications.

The alkalinity as well as the pH are essential parameters. By controlling these two values, it is possible to limit the corrosion in the system [14]. John

R. Baylis created what is now known as the Baylis curve (see Fig. 2.7). It shows the solubility of $CaCO_3$ with regards to alkalinity and pH. By choosing specific couple values of (pH, alkalinity), it is possible to decrease the water natural corrosivity.
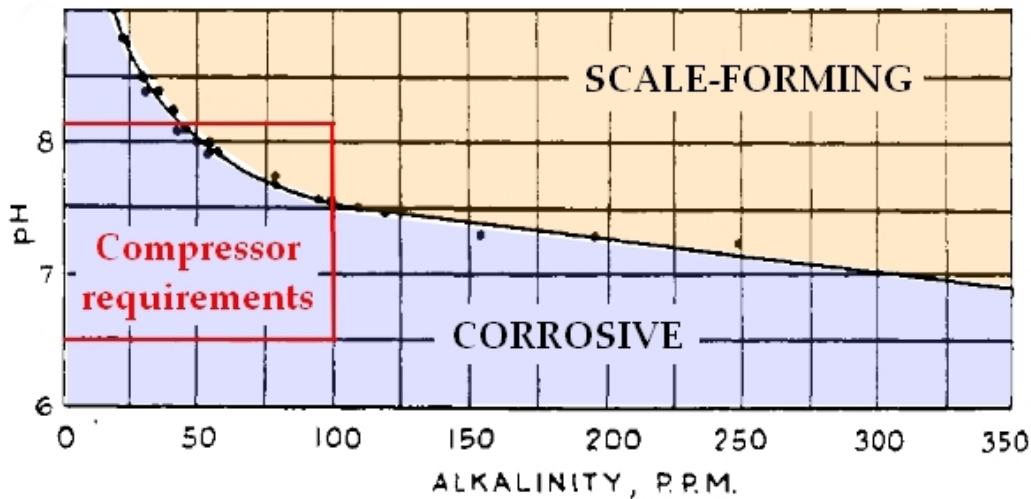
Figure 2.7: **Baylis curve** - The black line shows water parameters which will result in stable water. Couples of parameters located below this plot will result in corrosive water and couples above the plot correspond to scale-forming water. Sumitomo's allowed range is indicated in red (Adopted from [14]).

Concerning biological factors, we have seen that many bacteria can speed both corrosion and the formation of corrosion by-products. Fortunately none of them are harmful to health as they are all quite resistant to high levels of disinfectant (e.g. chlorine). We will see in the following section that other type of bacteria can represent a real limit in closed circuit application even if they are not directly connected to corrosion.

Bacteriological risks

With time, the performance of the compressor was severely affected by bacterial contamination of the water in the closed circuit. Biofilms damaged the pipe's surface [21], reduced the energy efficiency of heat-exchangers [18] and endangered the operating safety. Analysis were carried out by an external laboratory in September 2014. They came to the conclusion that the water could be considered high with a risk of health contamination when in

direct contact with the water.

In a nutshell, the handling of the contaminated water when cleaning the system had become potentially hazardous so that the system had to be taken out of operation. The compressor unit underwent an unscheduled maintenance at Sumitomo where the inner water pipes of the compressor were cleaned with acid.

Sample	CFU/ml at 22°C	CFU/ml at 36°C	Hazardous contaminant
Inlet circuit	44640	1370	Biofilm bacteria
Flowmeter	17120	3290	Biofilm and fecal bacteria
Outlet circuit	47440	13440	Biofilm bacteria

Table 2.3: Bacterial analysis of water flowing in the closed circuit [19]. CFU stands for Colony-Forming Unit and is an estimate of the number of viable bacteria and fungi in a sample at a fixed temperature.

Hazardous bacteria developping in water circuits are mainly of two kinds: biofilm bacteria and fecal bacteria. Fecal bacteria are clearly a consequence of a lack of hygiene when handling the circuit. They can be very dangerous for operators who will be in contact with the water [37]. The most common are E.Coli and Salmonella. The first ones can be eliminated by boiling the water or by using iodine tablets to desinfect the water. Salmonella bacteria need to be heated up to 60 °C.

Heating up the water would only kill a part of the bacteria. This process would not affect bacteria hiding in the biofilm against which chemicals are harmless. Biofilms bacteria are indeed very difficult to eradicate. For instance, even if the development of legionella is limited by water at 60 °C, the bacteria might not be killed [42]. Furthermore, after a week, the development rate might increase again. Another example is the one of Pseudomonas bacteria [55]. They were found in quite high quantity in the ALPS cooling circuit. These bacteria are known to hide in biofilm and could only be eradicated by antibiotics. Enzymatic solutions have been developed in the industry in order to destroy biofilm and extract hiding bacteria. Finally, besides being dangerous to human health, biofilm bacteria can seriously damage pipes.

In the end, heating up the circuit or using antibiotics and enzymatic solution were not suitable options. Nevertheless, this would anyway not have been sufficient considering the extent of the problem. Decision was taken to replace the circuit by a dedicated closed cooling system.

2.1.2 From January 2015 to July 2015

Water circuit

End of 2014, a custom-made commercial laser-chiller was purchased[9] (see Fig. 2.8). The unit was successfully installed in January 2015. This device is designed to cool down up to 9 kW, which corresponds to the power to dissipate in case of problem with the compressor. This compact setup includes an air-water heat-exchanger, a water pump, water and air filters as well as various sensors (e.g. pressure sensor, thermometer, flowmeter).

Such a device needs to be in a well aerated place. In our case, the room temperature is of $20.5 \pm 0.2°C$. Great care has been given in the choice of the different characteristics of the device (see Tab. 2.4).

Parameters	Requirements	Circuit characteristics
Cold water temperature (°C)	4.0 - 28.0	15.0 ± 0.1
Pressure range (bar)	1 - 6.9	3.7 ± 0.1
Flow rate (l/min)	4.0 - 10.0	9.3 ± 0.1
Particle size (μm)	<100	50

Table 2.4: Evaluation of the current water circuit characteristics through a comparison to the Sumitomo requirements [52].

Cold water temperature - The compressor inlet temperature is an essential parameter. It has a direct effect on the temperature baseline inside the cryostat. The colder the cooling water, the lower the temperature baseline will be. This explains the difference between the temperature baselines that were observed with the clean *pre-January-2015* setup and with the *post-January-2015* upgrade (see Tab. 2.1). Indeed, the inlet water was at 8 °C in the past. The temperature of the water in the circuit is now of 15.0 ± 0.1 °C. It corresponds to the minimal temperature that the current laser chiller setup can attain without modification of the system. In order to reach lower temperatures, the cooling liquid would be replaced by a glycol/water mix[10] and the pipes would need to be protected with foam in order to avoid condensation water and then possible electrical risks. Replacement of the cooling

---

[9]Laser chiller P810-AW-S from Termotek company

[10]Two cooling mixes can be used: 50/50% water/ethylene glycol or 50/50% water/propylene glycol [52].

liquid has been considered but it has been shown that decaying products of such a mix can be extremely corrosive [69].

Flow rate and pressure range - The flow is a crucial characteristic of the cooling circuit. The bigger the flow, the smaller the temperature baseline will be. With first circuit, a 0.1 K difference was measured for a flow difference of 1 l/min. The flow is regulated by a flow valve. In January 2015, the flow valve which was installed on the stainless steel output of the chiller was made of brass. A custom-made stainless steel valve was ordered but was delivered only one year later. This was a possible source of galvanic corrosion.

Particle size - A polypropylene water filter is mounted on the cold part of the circuit upstream the pump. It can stop particles with a diameter as small as $50\,\mu m$. It offers a good protection for the stainless steel water pump.

Figure 2.8: Water cooling system status after January 2015 - On the left, picture of the water circuit including the compressor and the chiller taken with a fish eye objective. On the right, picture of the EC/T/TDS/pH meter. (Source: Y. Berger)

The water quality has been proven to be a fundamental parameter in order to optimize the system. Tap water was clearly not a solution (see Tab. 2.2). Demineralised water presents the disadvantage of having a very low pH (i.e. < 6.5). Nevertheless, it is the best water candidate considering its very low electrical conductivity.

Decision was taken to produce the water following Sumitomo requirements. The pH of the demineralised water has been adjusted by adding pH plus[11] and pH minus[12] powders usually used for swimming-pool treat-

---

[11]Sodium carbonate
[12]Sodium hydrogen sulfate

ment. The monitoring of the electrical conductivity as well as the pH has been made since then with the help of a EC/T/TDS/pH meter[13] (see Fig. 2.8) .

Additional care was taken in the meantime to avoid every type of corrosion.

Galvanic corrosion - Galvanic corrosion was a real issue in the *pre-January-2015* setup. In order to reduce this phenomenon, careful selection of the constituent materials was made. The compressor side is made of copper and is attached to PVC pipes[14] for connection to the chiller. The chiller is a compact device including a stainless steel pump, stainless steel connectors as well as PVC pipes and filter connections. Only the brass flow valve, which was used up to June 2016, represented a galvanic corrosion source.

Bacteria development - In order to limit bacteria development, sterile demineralised water was chosen as source water. Every handling has been made since then with protective gloves and masks. Contact to rust has been avoided. The pipes which connect the chiller to the compressor are food-grade. Their surfaces are soft in order to limit biofilm development. They have been chosen transparent in order to facilitate the monitoring of suspicious deposits.

Helium circuit

In July 2015, the valve unit attached to the pulse-tube cooler required replacement after $\approx 15\,000$ operation hours[15]. This part contains a Rulon® piece which erodes more or less quickly with time, causing a drop in cooling performance (i.e. strong temperature drift over time). At this occasion, the service technician from the Sumitomo Cryogenics company additionally replaced the helium of the complete circuit.

2.1.3 After July 2015

For a year, the air-water chiller and the water-cooled helium-compressor have run smoothly, allowing to reach the optimum temperature baseline in-

---

[13]Hanna HI 9313-6 portable pH/EC/TDS/temperature meter reads pH, temperature, electrical conductivity as well as total dissolved solid concentration.

[14]PVC is the acronym of polyvinyl chloride.

[15]It was done a little earlier than anticipated as the manufacturer foresees regular exchange intervals of 20 000 hours of operation.

side the ALPS cryostat (e.g. 2,5 K). This optimal status will be maintained by performing frequent and well defined maintenances on the different parts of the primary cooling circuit (see Tab. 2.5).

Parts	Actions	Frequency
Air filter	Replacement	6 months
Water filter	Replacement	6 months
Water quality	Analysis	6 months
Water quality	Replacement	As often as necessary
Valve unit	Replacement	$20\,000 \pm 5\,000$ HO
Adsorber	Replacement	$30\,000$ HO
Cold head	Maintenance	$20\,000$ HO

Table 2.5: Regular maintenances of the ALPS cooling system for an optimal cooling power - For water analysis, a multiparameter bench photometer (Hanna HI83205 multiparameter bench photometer) has been purchased in order to measure the concentration of up to 20 different chemical components. HO stands for hours of operation.

In June 2016, a regular water maintenance was performed to replace the brass flow valve by the new stainless steel one, replace the used air and water filters as well as the water which had already been used for a year and a half. It was decided to use this opportunity to carry out in-house tests of the water quality. The analysis of the cooling water has been done using the multiparameter bench photometer. During the tests, four different water samples have been analysed. **Sample 1** was removed from the water circuit after one year and a half of usage. **Sample 2** was produced at the same time but has been stored in plastic cans for a similar period of time. **Sample 3** has been produced in June 2016 and stayed in storage. **Sample 4** was produced at the same time but flowed in the water circuit for one week. Various parameters have been measured such as the copper or the iron concentrations. Results can be found in table 2.6.

Copper - Copper is an essential parameter to measure. Indeed, dosage of this element gives information on the compressor status. Unfortunately, up to June 2016, the flow valve attached to the chiller was also made of brass[16]. Nevertheless, copper dosage is still very interesting.

We can see that in samples 2 and 3 (storage water), the copper quantity is very low. However, sample 1 and 4 show high concentrations of this ion. The brass valve was at first suspected to be the source for Cu^{2+} in the system. However, in June 2016, during the maintenance, the brass valve

---

[16]Brass is made of copper and zinc.

Parameters	Sample 1	Sample 2	Sample 3	Sample 4
Date of production	January 2015	January 2015	June 2016	June 2016
Duration of usage	1 year and a half	-	-	1 week
Temperature ($^\circ$C)	24	23	23	24
Copper Cu^{2+} (mg/l)	0.93 ± 0.02	0.01 ± 0.02	0.00 ± 0.02	0.25 ± 0.02
Free chlorine (mg/l)	0.08 ± 0.03	-	0.06 ± 0.03	-
Total chlorine (mg/l)	0.06 ± 0.03	-	0.00 ± 0.03	-
Iron Fe (mg/l)	0.00 ± 0.04	-	0.00 ± 0.04	-
Amonia NH_3-N (mg/l)	0.34 ± 0.05	-	0.09 ± 0.05	-
Ammonia NH_3 (mg/l)	0.41 ± 0.05	-	0.11 ± 0.05	-
Ammonium NH^{4+} (mg/l)	0.43 ± 0.05	-	0.11 ± 0.05	-
Silica SiO_2 (mg/l)	0.82 ± 0.03	0.20 ± 0.03	0.22 ± 0.03	-
Silicon Si (mg/l)	0.38 ± 0.03	0.09 ± 0.03	0.10 ± 0.03	-
joint **Dissolved oxygen** (mg/l)	8.6 ± 0.4	-	9.1 ± 0.4	-

Table 2.6: Analysis results obtained with the photometer in June 2016. Sample 1 and 4 have been taken inside the water circuit at different times. Sample 4 was put inside the circuit after the water maintenance. Sample 2 and 3 have never supplied the system. The temperature indicates the temperature of the samples when the tests were performed.

was replaced by the stainless steel flow valve. Sample 4 was taken after the switch and still shows high concentration of copper.

During the maintenance, the water filter was replaced and green deposits were found which could be copper hydroxy carbonate also known as malachite ($Cu_2(OH)_2CO_3$). This would be a sign of copper corrosion and could be explained by the usage of mixed pH plus (sodium carbonate, Na_2CO_3) and pH minus (sodium hydrogen sulfate, $NaHSO_4$) when the water was first produced:

$$\underbrace{NaHSO_{4(s)}}_{pH\ minus} + H_2O \rightarrow Na^+_{(aq)} + SO_4^{2-} + H_3O^+_{(aq)}$$

$$SO_4^{2-} + Cu^{2+} \rightarrow CuSO_4$$

$$\underbrace{2CuSO_4}_{from\ pH\ minus} + \underbrace{2Na_2CO_3}_{pH\ plus} + H_2O \Rightarrow \underbrace{Cu_2(OH)_2CO_3}_{Green\ precipitate} + 2Na_2SO_4 + CO_2$$
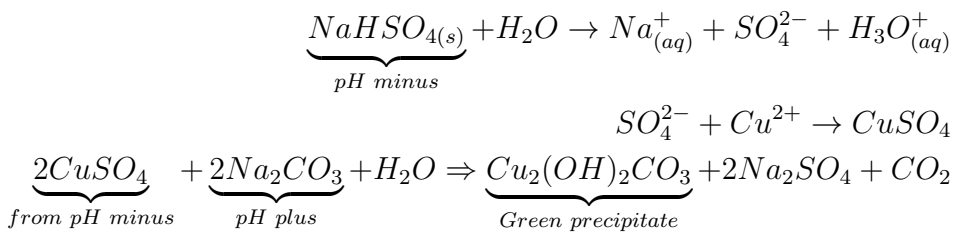
In the future, pH minus should not be used in the water production in order to avoid these chemical reactions catalysed by the filter. Iron concentration will be carefully monitored as dissolved copper could depose on steel surfaces where it could cause galvanic corrosion.

Chlorine - The total chlorine is the addition of the combined chlorine and

the free chlorine. The combined chlorine are all chlorine atoms which are combined with other organic elements. Following the evolution of these rates is very instructive as it gives information on the presence of organic molecules inside the water. Indeed, in the case where the water would be "dirty", the free chlorine rate would decrease and the total chlorine would increase. Results show that the water is free of organic elements. Chlorine concentration should not be too high as it would cause corrosion of the copper.

Iron - Iron concentration evaluates the status of the stainless steel components in the cooling circuit (e.g. the pump). No iron was found in new as well as used water. The stainless steel parts don't seem to be going through corrosion.

Ammonia - Ammonia as well as ammonium concentration were quite large after a year and a half. Nitrate-reducing bacteria might be present in the circuit. They would have transformed nitrate (NO_3^-) in ammonia (NH_3) [78] following:

$$NO_3^- + 2H^+ + 2e^- \rightarrow NO_2^- + H_2O$$
$$2NO_2^- + 4H^+ + 3e^- \rightarrow N_2O_2^- + 2H_2O$$
$$N_2O_2^- + 6H^+ + 5e^- \rightarrow 2NH_2OH$$
$$NH_2OH + 2H^+ + 2e^- \rightarrow NH_3 + H_2O$$
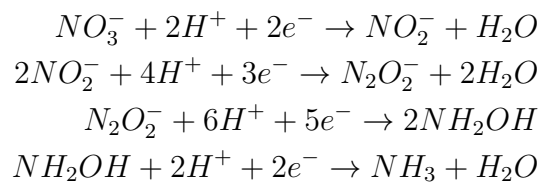
Unfortunately, the photometer does not allow for nitrate dosage. Nevertheless, the concentration is not concerning as it was shown in [68] that ammonia starts being a source of corrosion in copper alloys at concentration higher than $1\,\mathrm{ppm}$ (approx. $1\,\mathrm{mg/l}$) only. The water would need to be replaced frequently enough so that the ammonia concentration stays below this value.

Silica and silicon - Silica and silicon concentration have increased in the circuit. Every parts of the circuit have been considered as a silica source. The sealings of the system contain silicone[17]. Silicone caulk could have contaminated the water circuit.

These rates need to be carefully monitored. Indeed, diatoms, which are

---

[17]Silicones are polymers made up of repeating units of siloxane $Si - O - Si$.

among the most commons phytoplankton, are known to feed on silicate[18] [77]. Their arrival in a water circuit usually doesn't go unnoticed as diatoms contain a brown pigment and usually plate every free surface.

Dissolved oxygen - The dissolved oxygen concentration stayed stable after one year and a half. Oxygen-consumer processes could be limited. Nevertheless, considering [28], such dissolved oxygen rates are not worrying.

In summary, after implementation of all the improvements, the first stage of the ALPS cooling system has shown an optimal behaviour. Chemical analysis of the water allowed to improve the protocol which has been put in place in January 2015. The full circuit will stay under a close surveillance as we have learned the importance of this part of the cooling system.

2.2 Secondary cooling system

The secondary ALPS cooling system is an Adiabatic Demagnetisation Refrigerator (ADR) that can be seen on figures 2.9 and 2.10. It is divided in five different stages with varying temperatures as well as various components (see Tab. 2.7). More detailed information on ALPS ADR components can be found in [29]

ADR stages	Shielding	Thermometer	Additional components	T_{CD}	T_{RC}
300 K stage	3 mm thick Al	-	Pressure gauge	300 K	300 K
70 K stage	2 mm thick Al	✓	6 T magnet	50 K	50 K
4 K stage	2 mm thick Al	✓	Heat-switch motor	2.5 K	2.5 K
GGG stage	-	✓	Attached to GGG pill	2.5 K	500 mK
FAA stage	< 1 mm thick Cu	✓	Attached to FAA pill	2.5 K	80 mK

Table 2.7: Characteristics of the different ADR stages - T_{CD} is the cool-down temperature after thermalisation. T_{RC} is the temperatures of the different stages during a recharge while the regulaton is on (i.e. data-taking time).

The ADR can be put in two different positions. In **maintenance position**, the cold-head unit faces the ground while the FAA cold-finger[19] points to the roof. In **working position**, the full cryostat is rotated by 180 ° so that the FAA cold-finger points to the ground and the cold-head points to the roof.

---

[18]Silicate contains SiO_4 connected to other elements such as aluminium, iron or sodium.
[19]The cold-finger is the metallic bar on which the detector chip is attached.
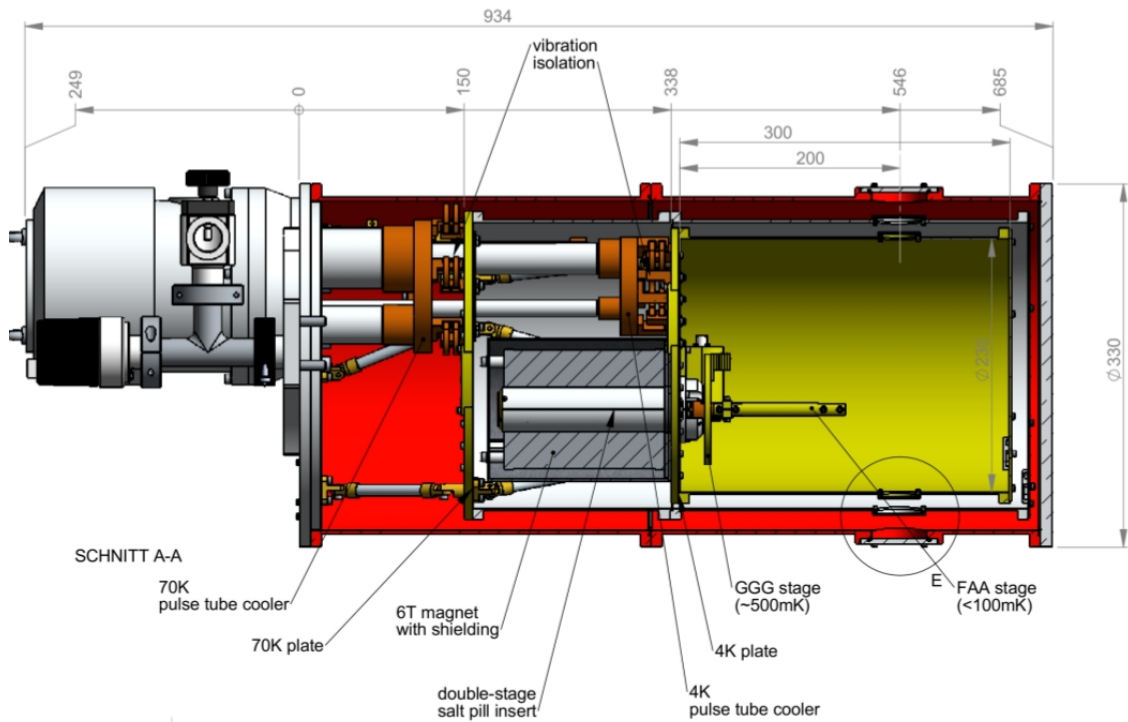
Figure 2.9: ADR drawing (Source: Entropy GmbH)
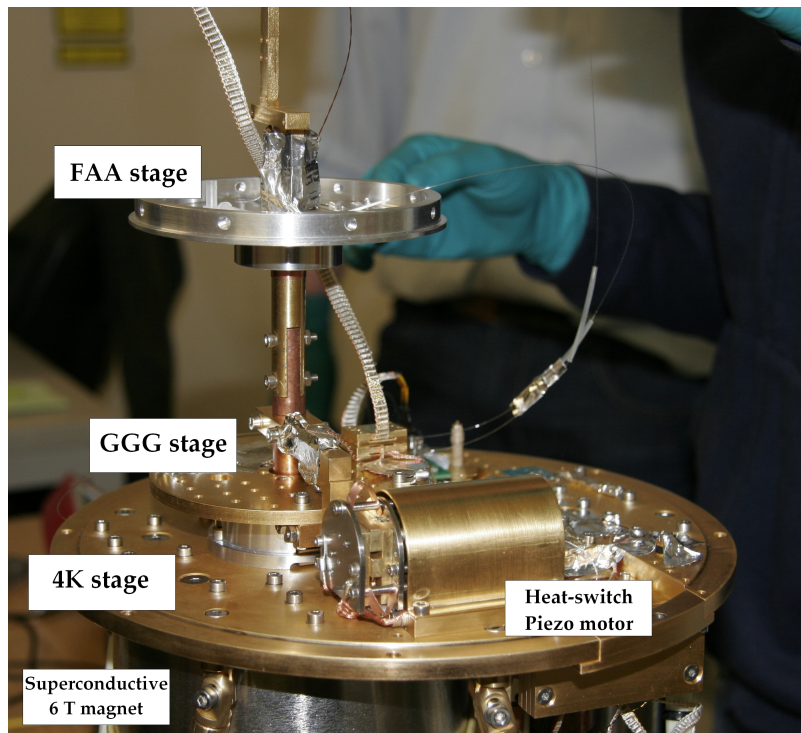
Figure 2.10: Picture of the inner stages of the ADR in maintenance position [89].

The colder stages of the ADR system are preliminary cool-down by the double-stage pulse-tube cryocoolers which gives a temperature baseline of 2.5 K (see Sec. 2.1). At this temperature, a recharge can be performed in order to reach 80 mK which is the ALPS TES working temperature.

The ADR has in its heart a double-stage salt pill insert constituted of FAA[20] and GGG[21]. Each of them are attached to the stage of the same name (see Tab. 2.7). FAA stage can reach a temperature as low as 30 mK. This stage is the coldest and is attached to the detector chip via the so-called cold-finger. Inside the salt pill insert, each pill is mechanically maintained as well as thermally coupled to the next outer stage through Vespel pins. This coupling can be neglected when the heat-switch piezo-motor is closed (see Fig. 2.12 and 2.13). Indeed, when the heat-switch is in a close position, the FAA/4K and GGG/4K couplings are maximal.
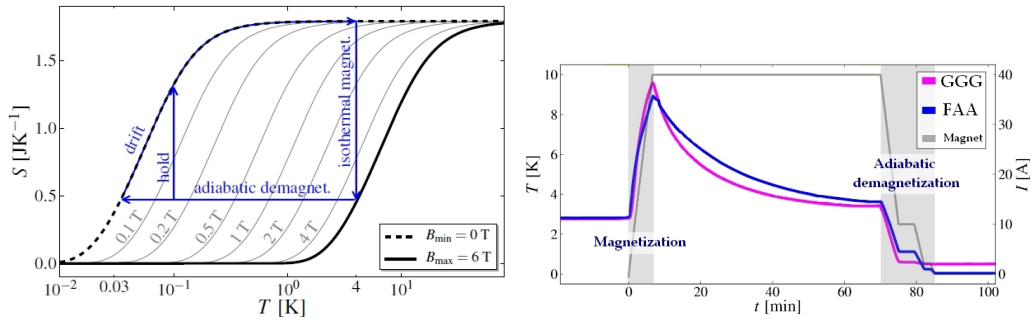
Figure 2.11: Recharge process - 1) FAA and GGG are in temperature equilibrium with the 4K-stage. The heat-switch is closed. 2) **Magnetization**: The superconductive 6T magnet is ramped up. The magnetization is not isothermal. T_{FAA} and T_{GGG} increased. 3) After thermalization of FAA and GGG, the heat-switch is opened to decouple FAA and GGG from the rest of the cryostat. 4) **Adiabatic demagnetization**: The magnet is ramped down in three steps. 5) FAA and GGG temperatures are as low as $T_{FAA} \approx 30\,mK$ and $T_{GGG} \approx 500\,mK$. (Adopted from [29])

A recharge is a cycle at low temperature (see Fig. 2.11). Before the process is started, FAA and GGG are strongly coupled to the 4K-stage and, as a consequence, their temperature are similiar to the 4K-stage temperature (i.e. the temperature baseline). The recharge protocol starts with the ramp-up of the 6T magnet going from 0 to 40 A. Both inner stages are going to be heat up through their coupling to the salt pills. The spin of electrons of the pills are aligned. For approximately one hour, the pills will thermalise thanks to

---

[20]The FAA salt pill is $\approx 80\,g$ of Ferric Ammonium Alum ($Fe_2(NH_4)_2(SO_4)_4 24H_2O$).
[21]The GGG salt pill is $\approx 95\,g$ of Gadolinium Gallium Garnet ($Gd_3Ga_5O_{12}$).

the pulse-tube cooler.

The thermalisation temperature is higher than the temperature baseline[22]. It is reached when $T_{FAA} = T_{GGG}$ and has to be $< 4\,K$ in order to maintain $T_{recharge}$ as low as expected during a reasonable hold-time. The heat-switch is opened in order to decouple the salt pills from the rest of the cryostat.

The magnet is finally ramped down in three steps. At that moment, the salt pills are completely decoupled from the rest of the ADR. The magnet ramping down, the spins will be misaligned again (for a maximization of the pills entropy). However, such a process requires energy. The only energy left is the heat of the salt pills [39, 65]. It will result in a temperature decrease of the inner stages of the cryostat as low as $T_{FAA} \approx 500\,mK$ and $T_{FAA} \approx 30\,mK$. The GGG stage plays the role of a thermic buffer between the detector stage (i.e. FAA) and the warm 4K-stage.

The TES superconductive detector needs to be maintained in its superconductive regime at a stable temperature during the full recharge. The chosen temperature is of $80\,mK$ in this case. In order to reach this requirement, the $6\,T$ magnet is ramped up to approximately $100\,mT$ in a standard process of Proportional-Integral-Derivative (PID) regulation [57]. After approximately 24 hours, the magnet current will reach zero and the temperature will start rising again in the ADR (see Fig. 2.14).

2.2.1 Cooling performance

The hold-time at $80\,mK$ is an essential parameter of the ADR as it corresponds to the detector working time during which data can be taken. Recharge optimization can be done by many means. In summary, coupling of the colder stage to heat source needs to be avoided as much as possible.

Vibrations of the different components inside the ADR can be a source of heat. Aluminium tape is used to fix all the wirings which could vibrate or enter in contact with FAA or GGG. The vacuum quality is also an important criterion. Outgasing inside the cryostat needs to be minimized and leak needs to be repaired. In the cold the pressure is as low as $4.0 \cdot 10^{-7}\,mbar$. Permeability status is tested at the beginning of every cool down with an Alcatel leak detector including two vacuum pumps as well as a mass spec-

---

[22]It might be due to the heating of the magnet normal resistive power cables. The 70K-stage temperature is going up, producing an increase in the temperature baseline.
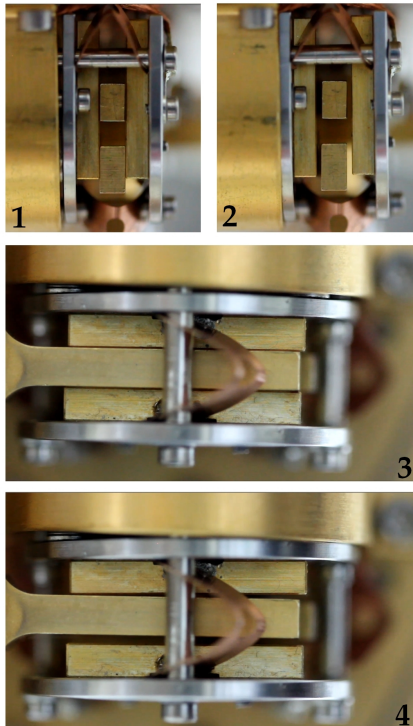
Figure 2.12: Heat-switch close and open in ADR working position (detector near to the ground).
1) View from the side of the close heat-switch.
2) View from the side of the open heat-switch.
3) View from below of the close heat-switch.
4) View from below of the open heat-switch.
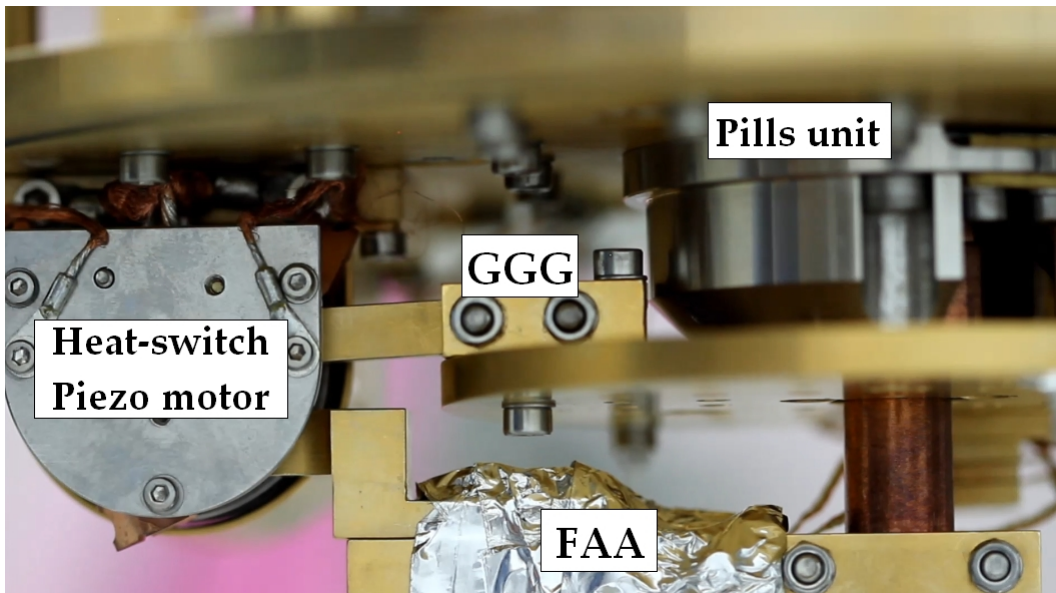
Figure 2.13: Heat-switch lateral view.
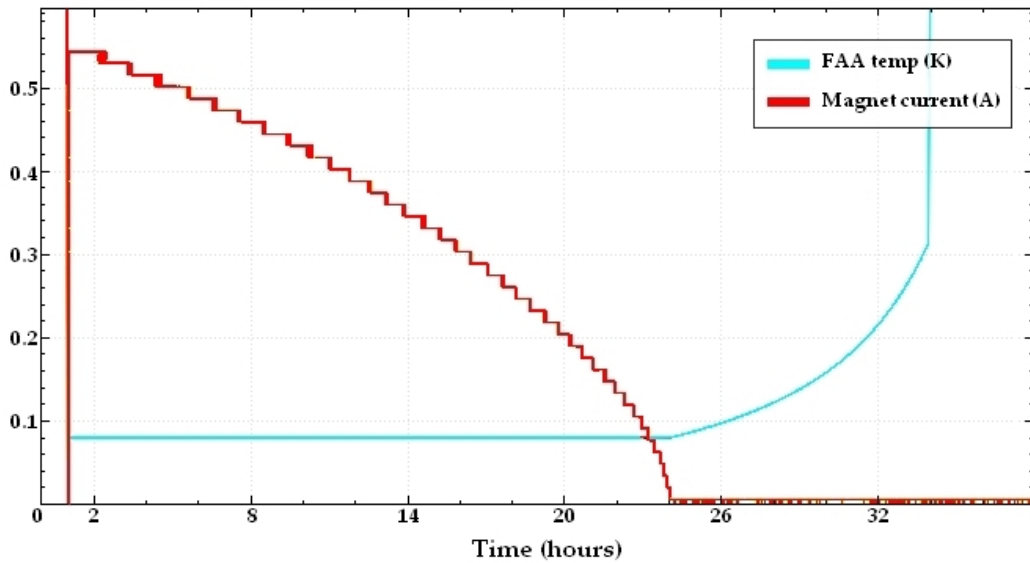
Figure 2.14: Holding time at 80 mK and PID controlled regulation.

trometer calibrated for helium[23].

The incidence of the previous points on the hold-time would be negligible, should the heat-switch not work properly. The device has to be set up by finding a good compromise between a fast motion of the actuator and an optimized thermal contact when closed. In the case where the heat-switch is not set correctly, it might not even be possible to thermalize FAA and GGG at the beginning of a cool-down. The heat-switch design currently in usage inside the ALPS cryostat is known to present frequent failures. Multiple times, the motor stopped functioning in the cold. In other cases, the heat-switch moves on its own at unexpected times. The piezo-motor motions have been studied by speeding up movies taken for different positions. A tilt move at the beginning of the opening motion has been highlighted. These interferences could be connected to the aging process of the mechanical structure which maintains the motor.

In the case where the heat-switch would correctly be opened but that the hold-time would still be short, other causes should be considered. Indeed, the pins which maintain mechanically both salt pills are very delicate to adjust and, if not set up correctly, are known to considerably shorten the hold-time [29].

---

[23]The primary pump is a turbomolecular pump which allows to reach pressures of 10^{-2} mbar. The secondary pump is an oil pump.

In April 2016, the inner structure which maintained the pills broke. The mechanical support was replaced. A few cyclings in the cold have been necessary so that the material is ready for an optimal operation. Current October 2016, a few recharges have been performed. However, the hold-time was of 1 h 30 only. Since then many studies have been conducted in order to understand the source of this issue. One of them consisted in modelling the heating up of FAA and GGG during a recharge without regulation.

For this study, the ADR has been divided into three systems: a bath at a constant temperature T_b, the GGG stage (T_G) and the FAA stage (T_F). They are all considered to be uniform in temperature. We consider that FAA and GGG have heat exchanges following four different processes. First, they can exchange heat through the heat-switch if this one is closed. Second, they can exchange heat through the mechanical pin structure. Third, they can be cooled-down by adiabatic demagnetisation ($\dot{q}_{ad}$). Finally, they are subject to a finite heat production considered to be independent of the temperature and connected to parasitic effects ($\dot{q}_s$). This can be summed up by the following system of equations:

$$\dot{T}_b = 0$$

$$C_G(T_G)\dot{T}_G = \underbrace{\lambda_{HS}\frac{A_{HS}}{l_{HS}}(T_b - T_G)}_{Heat-switch} + \underbrace{N_P\lambda_P\frac{A_P}{l_P}(T_b - T_G)}_{N_p \ pins \ between \ GGG \ and \ the \ bath}$$

$$- \underbrace{N_P\lambda_P\frac{A_P}{l_P}(T_G - T_F)}_{N_p \ pins \ between \ GGG \ and \ FAA} + \underbrace{\dot{q}_{s,G}}_{Parisitic \ heat} - \underbrace{\dot{q}_{ad,G}}_{Adiabatic \ Demagnetisation}$$

$$C_F(T_F)\dot{T}_F = \lambda_{HS}\frac{A_{HS}}{l_{HS}}(T_b - T_F) + N_P\lambda_P\frac{A_P}{l_P}(T_G - T_F) + \dot{q}_{s,F} - \dot{q}_{ad,F}$$

$C_G(T_G)$ and $C_F(T_F)$ are the heat capacity of GGG and FAA. λ_P is the heat conductivity of one pin and λ_{HS} is the heat conductivity of the heat-switch. (A_P, l_P) and (A_{HS}, l_{HS}) are the contact surface and the length of the pins and the heat-switch respectively. When the heat-switch is completely open after an adiabatic demagnetisation, the equations can be simplified to:

$$\dot{T}_b = 0$$

$$C_G(T_G)\dot{T}_G = N_{P1}\lambda_{P1}\frac{A_{P1}}{l_{P1}}(T_b - T_G) - N_{P2}\lambda_{P2}\frac{A_{P2}}{l_{P2}}(T_F - T_G) + \dot{q}_{s,G}$$

$$C_F(T_F)\dot{T}_F = N_{P2}\lambda_{P2}\frac{A_{P2}}{l_{P2}}(T_G - T_F) + \dot{q}_{s,F}$$

$$\kappa_{p1} = N_{P1}\lambda_{P1}\frac{A_{P1}}{l_{P1}} \approx 3.9 \cdot 10^{-3}\, T^{1.2}\, mW/K^{-1}$$

$$\kappa_{p2} = N_{P2}\lambda_{P2}\frac{A_{P2}}{l_{P2}} \approx 4.5 \cdot 10^{-3}\, T^2\, mW/K^{-1}$$

Using these equations, a modelisation of the cryostat warming up during a recharge has been performed. The results have been compared to data collected during a previous cool-down as well as to data obtained during the latest failed recharge.

Conclusion of this modelling work is that the coupling between FAA and GGG was higher than expected by a factor of 8 [45]. Following these results, the full salt pill structure has been opened again. The pins which mechanically maintain the structure were again broken which resulted in this huge coupling. The two successive breaks of the pins is an issue that will be investigated.

2.2.2 Magnetic shielding

SQUIDs are magnetometers (see Sec. 1.2.2). As a consequence, the ambient magnetic field B_{amb} should be minimized. The SQUIDs are made of niobium Nb which acts as a type II superconductor with a transition temperature of $Tc_1 = 9.3\ K$ (see Tab. 2.8). Type I superconductors have only one phase transition, whereas type II have two of them.

This leads to the risk of trapping flux inside the niobium part of the chip. Indeed, if the ambient magnetic field increases up to $B_{amb} > B_{cool,max}$, the niobium might be brought into the mixed phase where normal resistive vortices can be found inside the superconductive material [17, 29]. This limit value can be determined following $B_{cool,max} = \phi_0/\omega^2$ with ϕ_0 the magnetic flux quanta and ω the line width of the SQUID Nb stripes [76]. This trapped flux will lead to phase differences in the response of the SQUIDs of the SSA (SQUID serie array, i.e. SQ2) (see Fig. 2.15 and 2.16). The amplitude of the

Type I		Type II		
$X < Xc$	$X > Xc$	$X < Xc_1$	$Xc_1 < X < Xc_2$	$X > Xc_2$
S	N	S	S+N	N

Table 2.8: Phase transformation in superconductors for the two different types of superconductor (S stands for superconductive and N for normal resistive). The different phase transitions depend on the current I, the temperature T and the magnetic field H of the superconductor. X can be replaced by I, T and H. Xc depends on the values of I, T and H.

response signal will then be limited, shortening significantly the rise of the signal where the SQUID is locked. The main consequence of such trapped flux inside the SSA is a non-negligible rise of the electronics noise. Above a certain critical limit, the ambient magnetic field will be high enough to bring the niobium to its normal conductive regime.

In 2014, it was concluded that the ambient magnetic field inside the ALPS IIa laboratory was uncritical to operate the NIST module equipped with two Transition-Edge Sensors (TES) and their Superconducting Quantum Interference Devices (SQUIDs) [29]. In October 2015, the SQUIDs started trapping flux.

Flux trapping

By plotting $V\phi$ curves, SSA modulations can be studied in order to determine among other things if some ambient magnetic field is trapped inside the array (see Fig. 2.17). The first step of this procedure consists in biasing correctly SQ2 at its working point which depends on the environment (i.e. the critical current Ic). Then, a signal called PhiX is sent to the SSA and its response is observed. In October 2015, for the first time, the SQUIDs were trapping flux (see Fig. 2.18).

Flux trapping is a local effect. Vortices are produced at one or more points of the niobium stripes (i.e. SQUID loop) and cause dephased voltage-fluxes. These vortices are local phase transitions (normal resistive/superconductive) and are favored by defects in the niobium structure [17]. These defects can be induced during the fabrication process or can be impurities brought later to the chip. Because the module was transported to PTB in Berlin for maintenance works, dust deposits were considered as a source of trapped-flux. The second source of flux-trapping is an excessive B_{amb} ambient magnetic field, higher than $B_{cool,max}$. This value is an intrinsic parameter that should
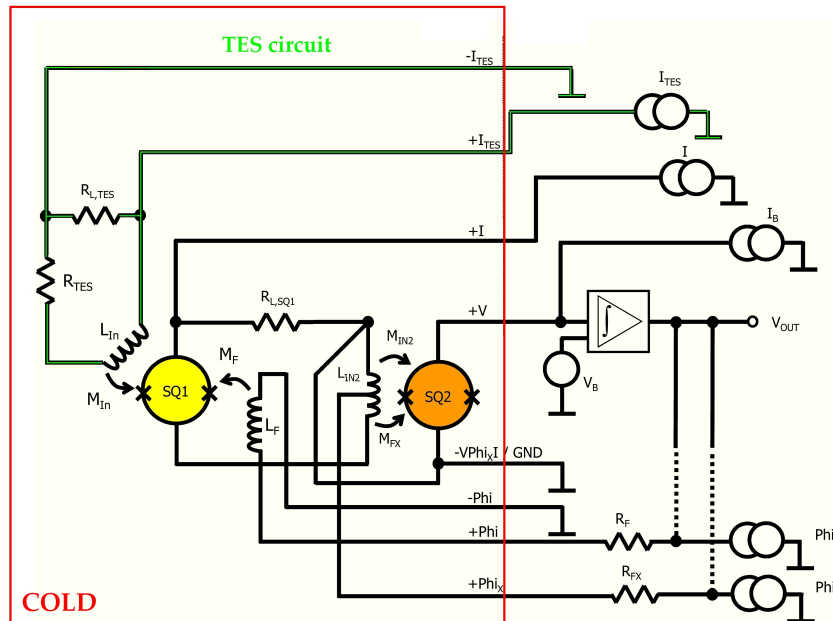
Figure 2.15: Electrical circuit of the detection system - The TES circuit as well as the two stage-SQUID are shown. The detector chip is connected through superconductive wires to the SQUID electronics box located outside the cryostat. The device has been developped by Magnicon. It allows to monitor as well as set the SQUIDs and the TES. (Source: PTB)
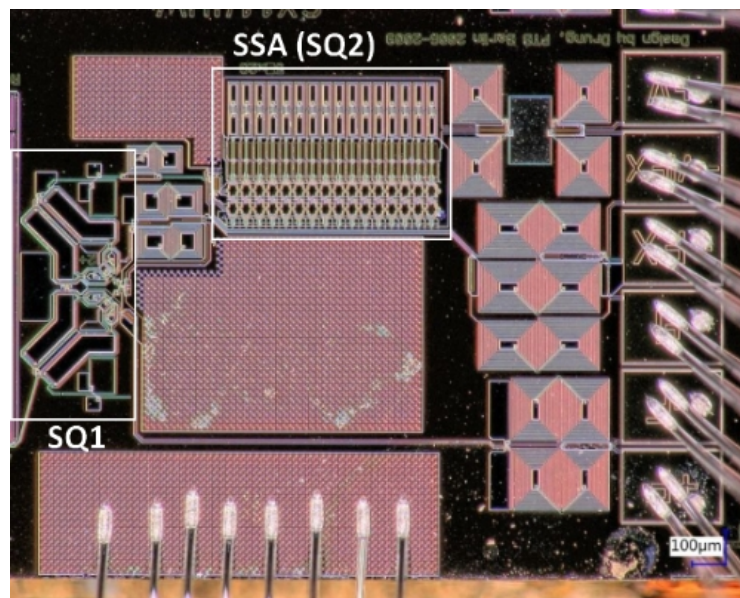
Figure 2.16: One double-stage SQUID - This picture was taken with a microscope. The SQ1 is connected to a serie array of 16 SQUIDs also called the SQ2 or SSA.
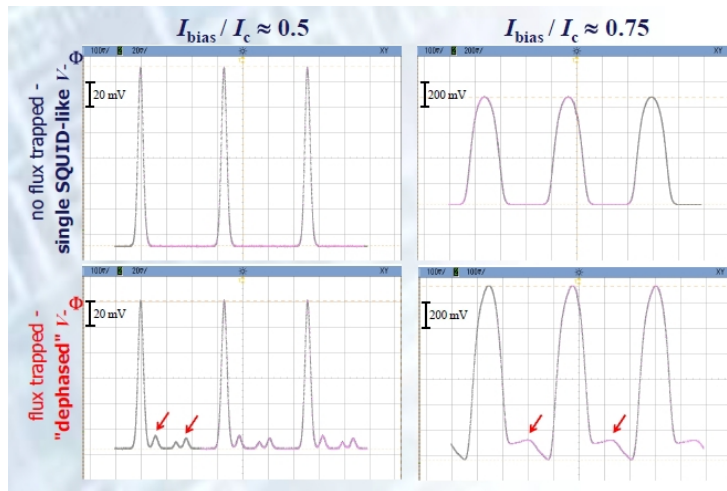
Figure 2.17: Trapped flux diagnosis - The four plots are Vϕ curves. They depict the output voltage of the SQUID as a function of time. The two top plots show a SQUID response for a working SQUID. The two bottom one shows Vϕ curves when flux is trapped. (Source: [17])
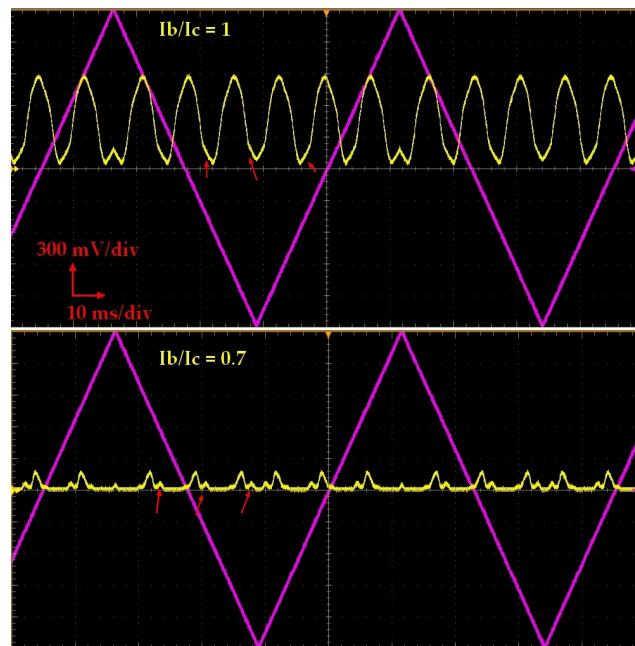
Figure 2.18: Vϕ curves for CH1 SSA - These oscilloscope screenshots show Vϕ curves which were taken during the same recharge. The magenta plot shows the PhiX fluctuations and the yellow plot depicts the voltage output of the SSA. The critical current (I_c) corresponds to the bias current (I_b) working point. When $I_b < I_c$, the trapped flux is easier to spot.

be stable in time and is different for each single SSA. Because the chip was working in the past, it was clear that either B_{amb} had increased in the laboratory or $B_{cool,max}$ had been lowered by impurities. Both hypotheses have been tested from October 2015 to February 2016 in order to find a long-term solution.

Ambient magnetic field

The first hypothesis which was tested is the one where the ambient magnetic field in the laboratory has changed. In order to study this possible cause, various tests have been performed. The DC ambient magnetic field has been measured with two different probes which are a Hall effect probe and an inductively coupled probe [20]. None of these measurements explained the new SQUID situation. Indeed, values which were measured were lower than the $B_{cool,max}$ of the chip, what seemed to rule out a high DC magnetic field as a trapped-flux source (see Tab. 2.9).

SQUID $B_{cool,max}$	Hall effect probe	Inductive coupled probe	Earth magnetic field
$\approx 95\,\mu$T	$40\pm9\,\mu$T	$32\pm4\,\mu$T	$49.6\pm0.1\,\mu$T

Table 2.9: Total DC ambient magnetic field measured in the surroundings of the cryostat with two different probes. Inductive coupled probes are known to be the most efficient devices for such low magnetic fields. The Earth magnetic field is given for the laboratory position in october 2015 according to [2]. The given error corresponds to the secular variation.

The complete ALPS laboratory has been considered in order to look for a new source of ambient magnetic field. All electronics devices located in the surrounding of the ADR have been switched off and all metallic pieces which were not necessary for operation brought to another room. None of these modifications resulted in any improvement. The only piece which was new to the room was the valve unit of the ADR. However, if the valve unit produces a high magnetic field (approx. $500\,\mu$T just below the device), it should not be an issue for the SQUIDs because of its position with respect to the cryostat.

The ADR has been rotated and moved in order to place the SQUID in a maybe lower magnetic field. Improvements were seen, but a position allowing a proper operation of the SQUID could not be found. A compensating coil[24] has been used without any success. Finally, Vϕ curves have been

---

[24]See [29] for details on the compensating coil.

taken while the ADR magnet was off and defluxed, i.e. after stopping the compressor to reach higher temperatures and going back to 2,5 K. Everything seemed to point to another source of flux-trapping.

Finally, both SSAs have been inspected under the microscope in order to look for dust debris which could create such an effect. Small particles of dust have been observed but not on enough SQUIDs of the SSA to explain the Vϕ curves shape.

Inner magnetic shielding

Because the cleaning of the SQUID requires a lot of efforts, the natural development for this situation was to test a magnetic shielding inside the cryostat in order to confirm that the ambient magnetic field was not the main issue. Indeed, the shielding would definitely lower the ambient magnetic field. However, this solution would prove insufficient, should the problem results from dust on the chip. The choice was made to install a 0.1 mm thick μ-metal foil[25] on top of the colder stage inside the cryostat (see Fig. 2.19). PTB has measured the reduction factor at 4 K of such material to be of 10. In our case, this factor was smaller as the μ_r of μ-metal decreases with temperature. However, it was decided to place the shielding inside the ADR as a problematic magnetic field inside the cryostat itself was not ruled out[26]. In February 2016, the foil was installed on top of the copper FAA shielding and Vϕ curves were taken at different temperatures.

At 2,5 K, the Vϕ curves of both SQUIDs were showing no sign of trapped flux. This meant that the recent situation was induced by a new high ambient magnetic field located outside the shielding. In order to test if this foil could be a long-term solution, the magnet was ramped up to proceed with a recharge. Once the recharge procedure was completed and a FAA temperature of 45 mK was reached, new Vϕ curves have been taken. As expected, both SQUIDs were trapping flux. Indeed, when the magnet is ramped up, the temperature of the FAA stage increases. With an ambient magnetic field of 6 T produced by the ADR magnet during the recharge procedure, the niobium critical temperature was lowered. As a consequence, the SQUIDs entered a mixed phase (superconductive + normal resistive) resulting in trapped-flux. With such tests, the foil has been permanently magnetised and no further tests were possible.

---

[25] μ-metal is made of nickel and iron.
[26] The presence of a high magnetic field inside the ADR was not probable as improvements were obtained by moving the cryostat inside the laboratory
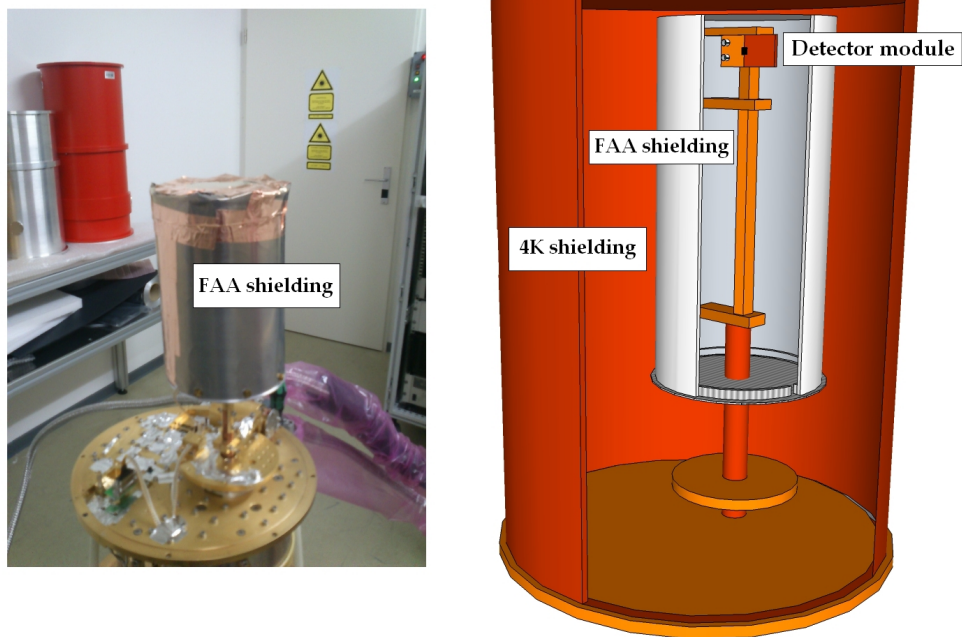
Figure 2.19: Inner μ-metal shielding - On the left, the picture shows the μ-metal shielding fixed with copper tape to the outer surface of the thermic FAA shielding. On the right, the drawing represents the colder stages of the ADR.

Outer magnetic shielding

Finally, the long-term solution which was tested successfully consists in placing a home-made μ-metal shielding around the cryostat following a specific procedure. The shielding was built with the same foil that was used inside the ADR. The design allows to install/remove quickly and easily the shielding (see Fig. 2.20). The μ-metal is placed around the cryostat before starting the cool-down. It can be removed after the thermalisation of the colder stages. During a recharge, the μ-metal needs to be stored far away from the ADR magnet to avoid its magnetization. When the procedure is done, the shielding can be placed back around the ADR. With a maximum temperature of $\mathrm{T}_{SQUIDs} = 10$ K reached during the full procedure, the SQUIDs always need to be defluxed before being used. It is easily done thanks to the heater installed next to each SSA. By heating up the array for 0.1 sec with a power of 26 mW, the trapped-flux is successfully defluxed as can be seen on figure 2.21.

In conclusion, even if the source of the new ambient magnetic field localised in our laboratory is not yet identified, it has already been well shielded.
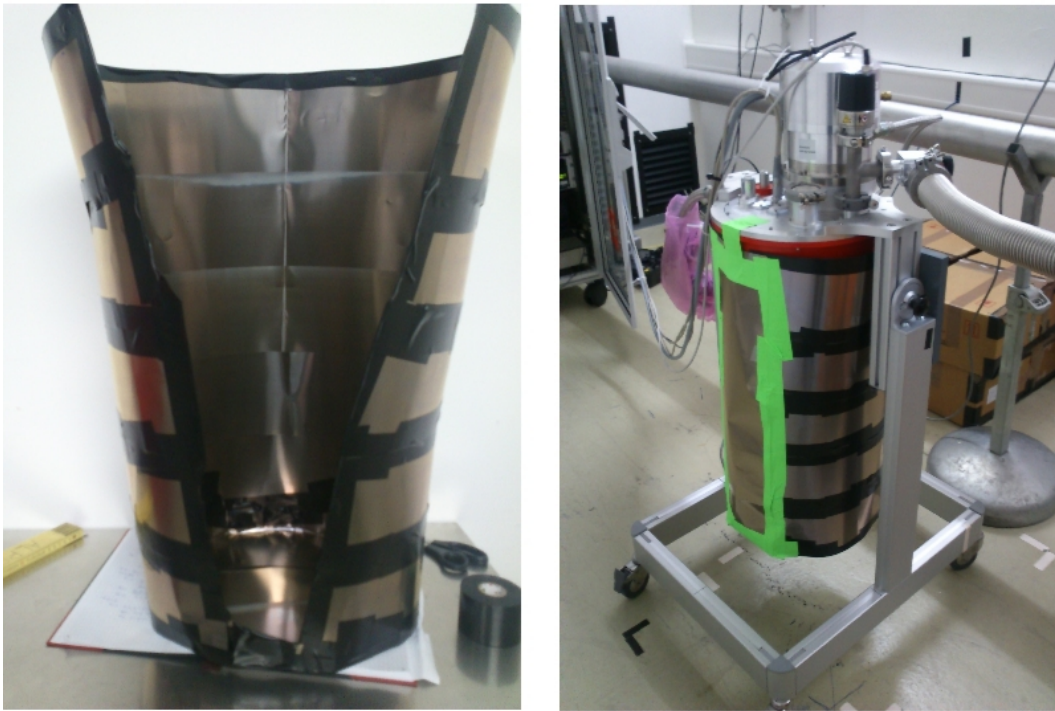
Figure 2.20: Outer μ-metal shielding - On the left, the picture shows the shielding opened. On the right, the picture shows the μ-metal shielding attached to the ADR outer shielding.
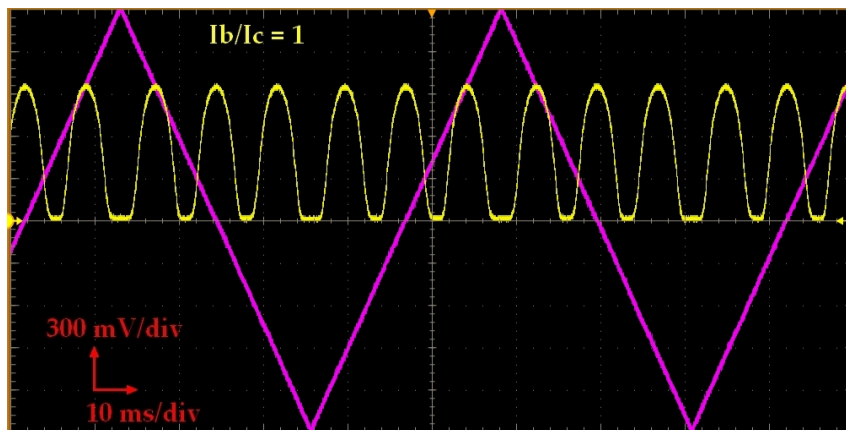
Figure 2.21: Vϕ curve for CH1 SSA - This oscilloscope screenshot shows a successful Vϕ curve. No trapped flux

3 A Transition-Edge Sensor for ALPS IIc

As regards infrared single-photon detection, the ALPS II collaboration chose a Tungsten Transition-Edge Sensor (W-TES) from the National Institute of Standards and Technology (NIST) (see Sec. 1.2.2). Indeed, such detectors are very promising considering the challenges that the ALPS II detector system has to overcome [11]. Complete characterization of the system was a necessary step in order to evaluate the different parameters of the detector.

In this thesis, the detector's stability, its detection efficiency (see Chap. 4) as well as its background rate (see Chap. 5) will be discussed in dedicated chapters.

This chapter will focus on the data analysis and the detector system stability. In a first section, data taking and analysis methods will be addressed. In a second section, the stability of the detector system according to different parameters will be assessed.

3.1 Data processing

Various detection setups have been used in the framework of this thesis. However, three main types can be defined (see Fig. 3.1):

- The **Noise setup**[1] is the simplest one. The detector module is isolated inside the cryostat. Every event will be considered as intrinsic dark counts. This setup is perfect to study the inherent parameters of the detectors and SQUIDs.

- The **Background setup** is similar to the previous one. However, in this case, the detector sees the warm outer environment thanks to an optical fiber going through the different cryostat stages and shining

---

[1]Capital letter have been added to setup names (i.e. Noise, Background and Signal) in order to differentiate them from event types (i.e. noise, background and signal).

on the TES[2]. Additional events come from outside (e.g. black body photons, ambient light) and inside the fiber (e.g. natural radioactivity, Cherenkov light). Comparison of the Noise and the Background events is essential. Indeed, the Noise count corresponds to the minimal background level achievable if no modification is brought to the detector module or its direct environment (i.e. the cryostat).

- The last setup called **Signal** is similar to what the detector will be exposed to in the ALPS II experiment. Light of different wavelengths can be shone inside the optical fiber attached to the detector. Such setup allows to do an extensive characterization of the detector's response to photons.
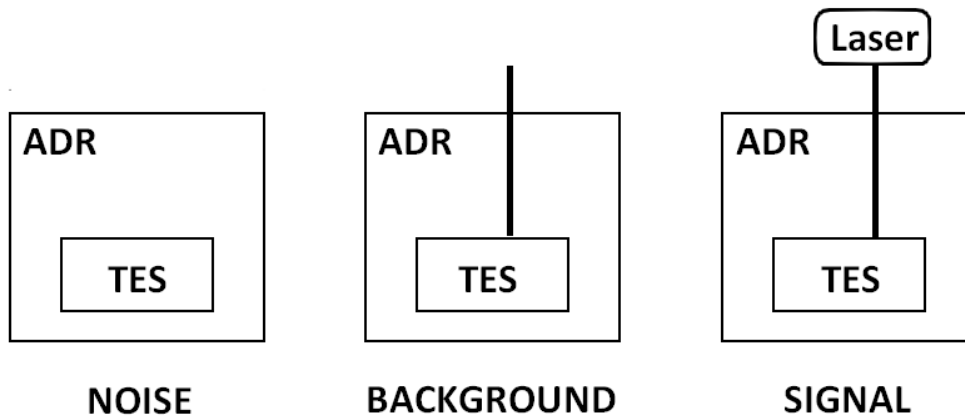
Figure 3.1: Three main test setups for the characterization of the ALPS II detection system - In the Background and Signal setups, the TES is attached to a single-mode optical fiber. The Noise and the Background data are presented in chapter 5.

Figure 3.1 gives a simplified view of the detection system. Indeed, the NIST module includes not one but two TESs. These detectors are called **Channel A** (CHA) and **Channel B** (CHB). Reference [29] focuses on CHA. In this framework, both detectors have been considered.

Similar pulse-shapes are expected for both detectors. However, for a fixed energy, the absolute value of CHB's pulse height is smaller than for CHA. One $1064\,\mathrm{nm}$[3] single-photon event can be seen on figure 3.2. A particle transfers energy to the detector or its surroundings. This change in heat will

---

[2]The fiber end is protected by a cap which should be opaque to visible light. Main contribution to the total counts is believed to be thermal (i.e. black body photons).

[3]For simplicity, the wavelength has been reduced to 1064 nm. In reality, two laser sources
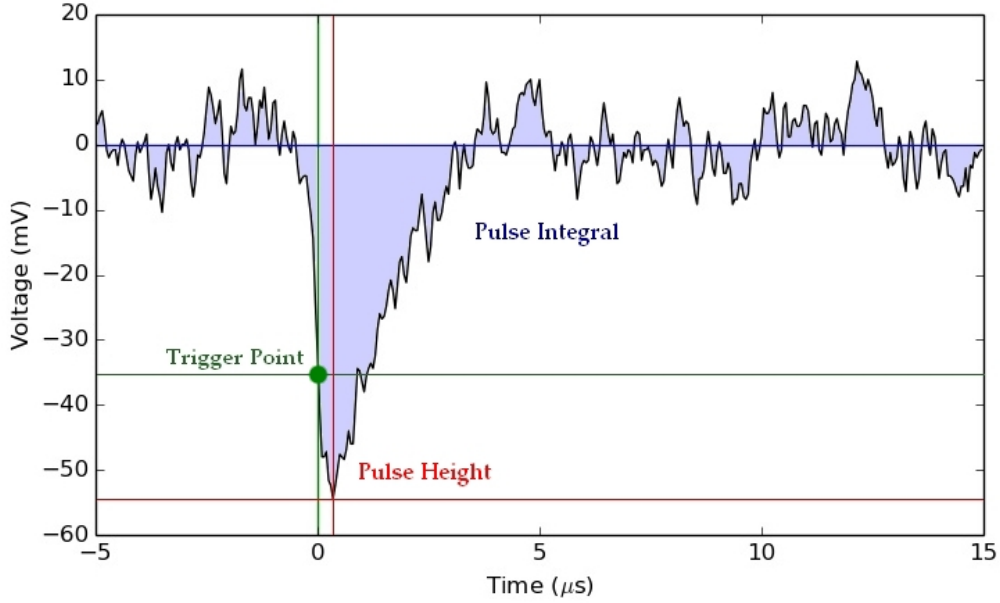
Figure 3.2: One CHB 1064 nm single-photon pulse - The trigger point had been used to center the pulse on $0\,\mu$s. The pulse height is shown in red and the pulse integral is depicted in blue.

result in a negative voltage [26]. The detector will slowly thermalize up to the point when the baseline is reached again at $T_{FAA}= 80$ mK. The baseline noise has an amplitude of approximately 20 mV. A trigger level can either be selected online (i.e. on the oscilloscope) or offline (i.e. in the analysis). A pulse height and pulse integral analysis (HIA) has been performed similarly to what is described in [29].

Each single event is represented by a couple of parameters (PH, PI) where PH (pulse height) is the peak value of the voltage and PI (pulse integral) is expressed as:

$$PI = \sum V_i \Delta t \tag{3.1}$$

that being the sum of all the voltage entries in the event window. Figure

---

have been used with wavelengths approaching 1064 nm. The S+K 51nanoFCM 1064 nm laser's wavelength was estimated at 1072 nm. The S+K 58FCM 1064 nm laser's wavelength was measured to be of 1059 nm. [89]

3.3 shows a PI-PH-plane for a Signal setup. Events generated by a 1064 nm laser will help define the ALPS II region of interest (ROI). This distribution can be described as a 2D Gaussian function. Different n-σ elliptic contours can be plotted[4]. The 3-σ contour of the 1064 nm population has been chosen as the ROI for the following characterization studies [29]. It allows to consider 99.73 % of the detected photons while limiting contamination from nearby populations. Figure 3.4 shows the average 1064 nm pulse for CHB. The stability of the ROI (i.e. the stability of the detector's response to 1064 nm photons) is an essential criterion which will be discussed in the following section.

3.2 Detection setup stability

In the framework of this thesis, the stability of various parameters has been assessed. For instance, studying the influence that a change in recharge, cool-down or laser could have on the 3-σ region parameters, gives a good indication of the stability which can be expected from the ALPS II detection system. Figure 3.6 summarizes these results.

Every 3-σ region can be described by five parameters (see Tab. 3.1). The center position is given by the pair (μ_{PH}, μ_{PI}) with μ_{PH} and μ_{PI} respectively the mean PH and PI values of the sample respectively. The scale of the ellipse contours is given by the standard deviation of PH and PI (σ_{PH} and σ_{PI}). Finally, as can be seen on figure 3.3, the ellipses are tilted. The 3-σ region inclination depends on the PH-PI correlation[5].

CD	RC	Laser	$\hat{\mu}_{PH}$ (mV)	$\hat{\mu}_{PI}$ (mV)	$\hat{\sigma}_{PH}$ (mV.μs)	$\hat{\sigma}_{PI}$ (mV.μs)	I_{TES} (μA)
28	7	58-FCM	-46.32 ± 0.01	77.95 ± 0.41	9.749 ± 0.06	40.77 ± 0.26	64.7 ± 0.5
32	2	58-FCM	-50.07 ± 0.07	78.21 ± 0.92	10.79 ± 0.08	73.03 ± 1.51	62.9 ± 0.5
32	3	51-nano-FCM	-50.37 ± 0.04	80.09 ± 2.16	10.96 ± 0.06	63.47 ± 1.54	62.3 ± 0.5
32	6	51-nano-FCM	-47.77 ± 0.07	77.27 ± 1.13	10.66 ± 0.10	91.21 ± 0.75	62.9 ± 0.5
38	5	51-nano-FCM	-51.067 ± 0.12	88.13 ± 0.45	10.99 ± 0.04	53.24 ± 0.64	58.0 ± 0.5

Table 3.1: Setup characteristics of the data plotted in figure 3.6 - CD stands for cool-down and RC for recharge. Considering [73], the S+K 51nanoFCM 1064 nm laser has a wavelength of 1072 nm and the S+K 58FCM 1064 nm laser has a wavelength of 1059 nm. The average values of μ_{PH}, μ_{PI}, σ_{PH} and σ_{PI} are given for every set of data. Finally, the TES bias current I_{TES} is given considering that PH depends on I_{TES}.

---

[4]n is an integer.

[5]More details on the correlation coefficient of PH and PI can be found in [29].
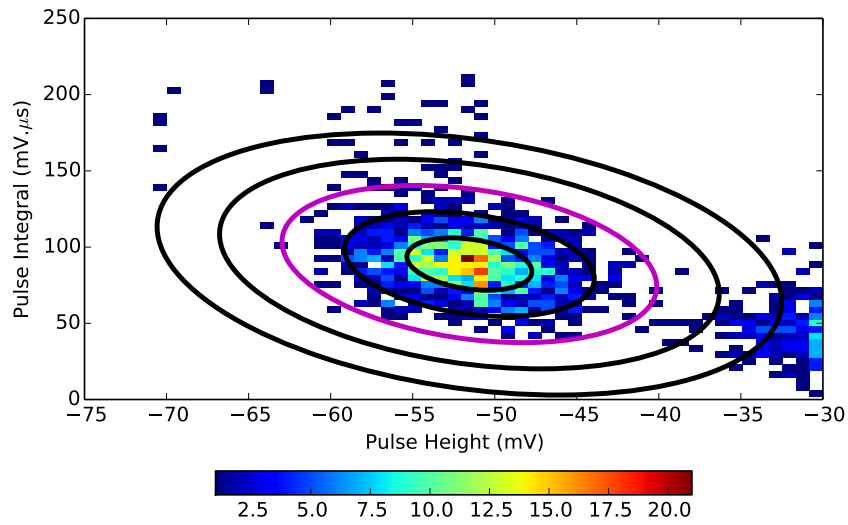
Figure 3.3: CHB PI-PH-plane - Events taken during 1 second with a Signal setup have been placed on the PI-PH-plane. The laser distribution follows a 2D Gaussian function. Elliptic contours correspond to the n first ellipses with n=[1,5]. The ROI (i.e. 3-σ contour) is marked in magenta. The laser used in this test has a wavelength of 1072 nm. The color scale corresponds to the number of counts in each bin.
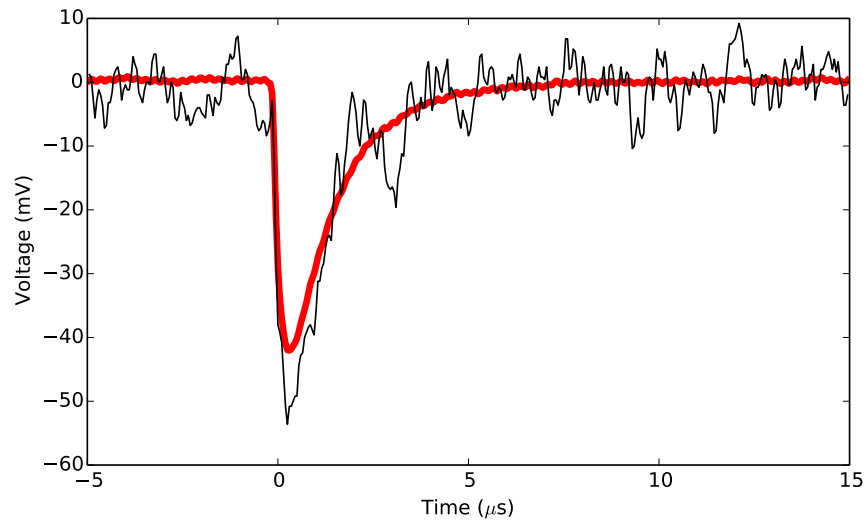
Figure 3.4: CHB average 1064 nm pulse - In black, one single event is shown. The red plot corresponds to the average pulse of the 1-σ region (Sample of 399 events).

Stability during a recharge - Measurements taken during one recharge have been plotted with similar colors on figure 3.6. It can be observed that the pulse height variation is lower than 0.25 % for photons with the same energy (i.e. same laser). Furthermore, the pulse integral fluctuation is lower than 3 %. The time-scale of a recharge is the most important parameter as it corresponds to the data-taking time.

In-depth studies of the stability during a recharge have been performed in order to determine the maximum expected fluctuations of the pulse height of monoenergetic events during a recharge. This can be done by studying the variation of the TES working point I_{TES}. This TES bias current (i.e. I_{TES}) corresponds to the electrical current applied to the TES detector in order to place it in its superconductive transition. I_{TES} is chosen in such a way that the resistance in the TES circuit is of $R_0 = 0.3 R_N$ with $R_N = 13.8\,\Omega$, that is to say the resistance of the TES when it reaches its normal conductive regime.

Evaluations of CHB's I_{TES} have been done every two hours during a complete recharge. Results can be found on figure 3.5. The fluctuations were found to be $< 1.5\,\mu A$. It is possible to convert this result into a PH fluctuation via [29] (see Fig. 2.15):

$$\Delta I_{TES}[\mu A] = \Delta V_{out}[\text{mV}] \cdot \frac{M_{in}^{-1}[\mu A/\Phi_0]}{R_f[\text{k}\Omega]M_f^{-1}[\mu A/\Phi_0]} \tag{3.2}$$

with for channel B, $M_{in}^{-1} = 5.747\,\mu A/\Phi_0$, the inverse mutual input inductance[6]. The feedback resistance R_f is of $100\,\text{k}\Omega$. The inverse mutual feedback inductance $M_f^{-1} = 44.16 \pm 0.038$ (stat.) $\pm\ 0.13$ (syst.) $\mu A/\Phi_0$[7] (see Fig. 2.15).This results in a conversion factor of:

$$(I_{TES}/V_{out})_{NIST,B} = 1.301 \pm 0.049(stat.) \pm 0.007(syst.)\,\text{nA/mV} \tag{3.3}$$

In conclusion, the bias current fluctuation will result in a pulse height difference of less than 2 % for channel B[8].

Stability during a cool-down - During the cool-down 32, samples have been recorded for three different recharges. $\hat{\mu}_{PH}$ varies by 5 % between recharges 2 and 6. This difference could be caused by the use of a distinct

---

[6]The inverse mutual input inductance has been estimated by PTB.

[7]This value of the M_f^{-1} has been measured in ALPS laboratory for a temperature of the SQUID similar to the working temperature.

[8]Similar measurements have been performed on CHA. Results can be found in [30].

laser but RC 3 results tend to invalidate this hypothesis. Furthermore, such a difference cannot be explained by a modification of I_{TES}. One possible factor which can explain such variation is the difference in laser power output between recharges 3 and 6. Indeed, it has been shown that both 1064 nm lasers demonstrate strong degradations of their spectrum at low power (i.e. the spectrum is largely broadened and the peak wavelength is shifted) [89].

Stability between cool-downs - In this case, the fluctuations between cool-downs are presumed to be induced by the modifications of the optical fiber setup. Indeed, the three different optical setups that were used in these tests were showing very various optical efficiencies (see Chap. 4). Such effects result in a fluctuation of approximately 10%.

In conclusion, the ALPS TES detector setup has proven to be reasonably stable over time. Its satisfactory stability during a recharge offers a reliable data-taking time of approximately 20 hours.
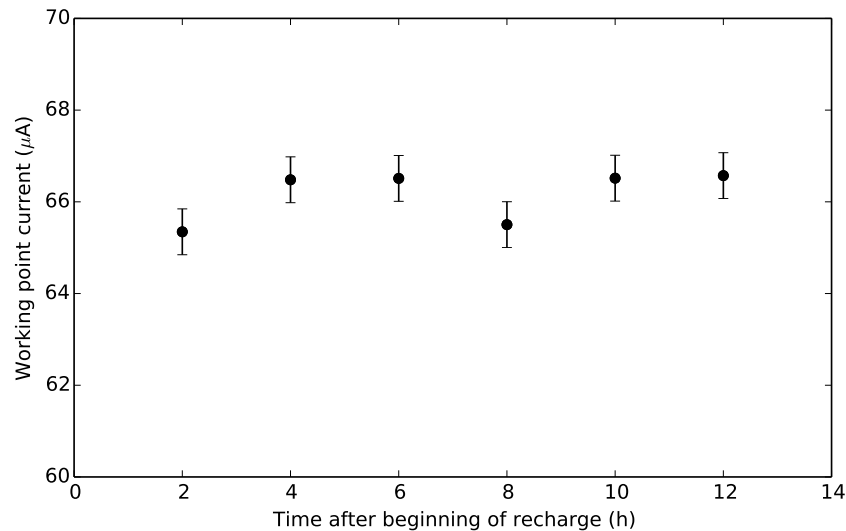
Figure 3.5: Stability of CHB I_{TES} over time during a full recharge at 80 mK - Stability of the TES working point current, equivalent to $R_0 = 30\ \%\ R_{normal}$, as a function of time after the beginning of a recharge.
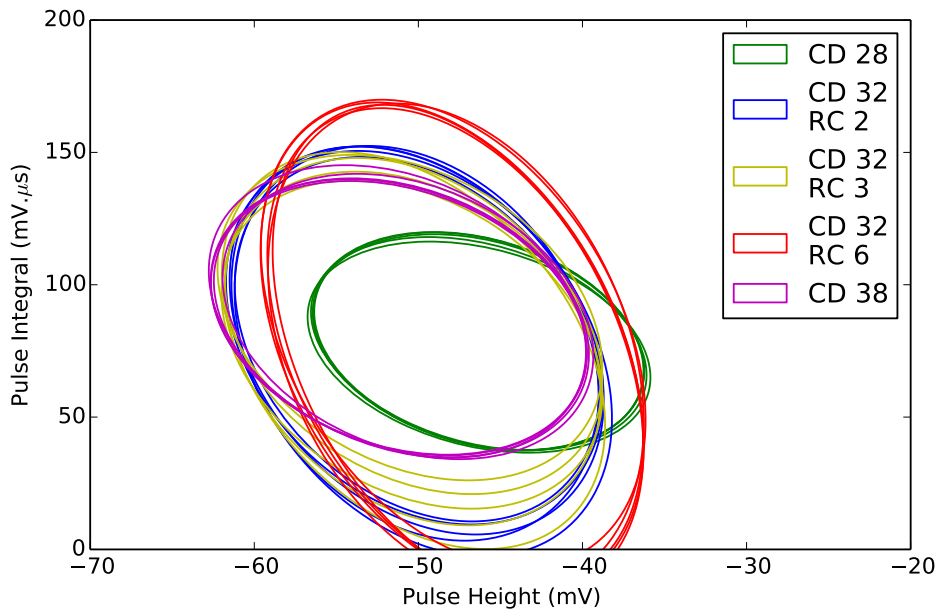
Figure 3.6: Stability of the 3-σ region for CHB - The green ellipses are connected to data which were gathered during cool-down 28 (CD). The blue, yellow and red elliptic contours represent data of three different recharges (RC) of cool-down 32. Between RC 2 and RC 3, the photon source has been switched (see Tab. 3.1). The magenta 3-σ regions correspond to data taken during CD 38. Each ellipse parameter is extracted from the statistical analysis of a sample of events, collected in one second of exposure. [73]

4 ALPS IIc detection efficiency

A high total detection efficiency of 1064 nm photons (η) is required in order to meet the ALPS IIc's sensitivity [11]. Indeed, the overall sensitivity of the experiment depends on the ALPs coupling to two photons $g_{a\gamma\gamma}$ which scales with $\eta^{1/4}$ (see Eq. 1.6). The different components that contribute to this variable are the 1064 nm transmissivity of the regeneration cavity (T_{RC}), the efficiency of the coupling of the 1064 nm beam inside the optical fiber (CE) and finally, the detection efficiency of the detector to 1064 nm photons (DE) which depends on the detector quantum efficiency[1] (QE) and on the optical efficiency of the optical fiber system (OE).

$$\eta = T_{RC} \cdot CE \cdot DE = T_{RC} \cdot CE \cdot QE \cdot OE \qquad (4.1)$$

For the ALPS II experiment, T_{RC} was determined to be of about 85% [44]. The aimed CE is of 95%. However, the best CE obtained so far is of 90% [87]. Concerning the detector, NIST has shown that such W-TES detectors have a QE higher than 95% [51]. In order to reach η >75% [11], the OE should be higher than:

$$OE > \frac{\eta}{T_{RC} \cdot CE \cdot QE} = 98\% \qquad (4.2)$$

In this context, an optimization of the OE of the detector was crucial. In the framework of this thesis, many tests were performed and many upgrades implemented. The description of the chosen method as well as the first results obtained for such a setup will be discussed further in section 4.1. The three different optimization phases will be described in section 4.2.

4.1 Detection efficiency evaluation

Two main methods can be used in order to determine the efficiency of a system. The first technique consists in sending a known number of parti-

---

[1]The QE includes the efficiency coupling of the fiber to the detector.

cles to a system and then compare it to the fraction of particles transmitted/detected [51]. A second approach involves evaluating the relative efficiency of a system compared to the one of a well-known setup (see Fig. 4.1). Such a process is the method that was picked for these tests [12]. It will be further detailed in the following paragraphs.
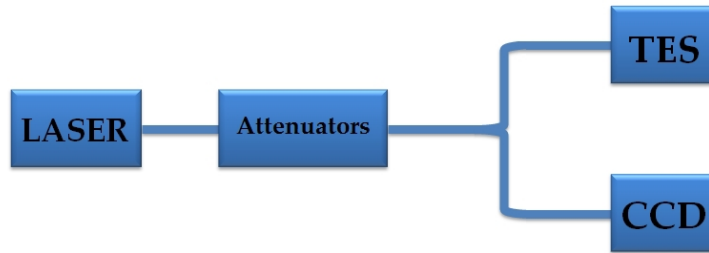
Figure 4.1: Evaluation of the TES efficiency with a back-to-back setup - The lines connecting the different components of the setup represent optical fibers.

A 1064 nm laser beam, after being strongly attenuated[2], is injected inside a fiber coupler. The attenuation was chosen to achieve a TES rate of approximately 1 000 evt/sec[3]. The TES counts are compared to the counts obtained by the ALPS I CCD camera in order to evaluate the efficiency of the TES detector. The former Pixis CCD camera was a good candidate for an assessment of the TES DE because its quantum efficiency had already been measured in the past [83]. However, such a solution presents a serious weakness: its quantum efficiency is of $(1.208 \pm 0.002(\text{stat}) \pm 0.079(\text{syst}))\%$ for 1064 nm [83]. As a consequence, such a back-to-back measurement is rather delicate as it is necessary to find a good compromise between receiving enough photons on the CCD on the one hand and not saturating the TES on the other hand.

Following such a technique, a first evaluation of the detection efficiency of both TESs was performed in February 2014 (see Fig. 4.2). The 58FCM laser has been connected to various attenuators. Downstream, a 2x2 SMF28 fiber coupler has been used in order to feed simultaneously one of the TESs and the CCD. Such device is produced by fusion-combining two fibers. Each fiber coupler comes with a defined split ratio. Because these devices are bidirectional, any one of the four fibers may be used as a single input. In this case, one of the ends was connected to the laser and the two outputs

---

[2]The attenuation was approximately of 20 dB.

[3]At this rate, the dead-time of the detector is negligible if compared to the statistical error of the 3-σ counts.

64

were swapped multiple times. Taking into account the ratio of the fiber coupler[4], the conclusion for such tests is that the detection efficiency of the TES detectors was very low. The channel A's DE has been measured to be approximately 700 times lower than the CCD's efficiency. Channel B was approximately 900 times less efficient than the Pixis camera.
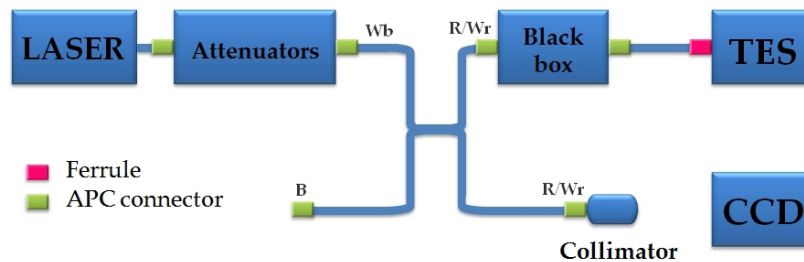
Figure 4.2: Test setup number 1 - The fiber 58FCM laser ($\lambda = 1059$ nm, see Sec 3.1) is attenuated by a few attenuators placed in series. This part of the setup does not influence the detector setup's optical efficiency. The incoming photons are then coupled to a 2x2 fiber coupler through an FC/APC connector. Outputs R and Wr are swapped after each measurement. On the TES side, the coupler is coupled to the TES fiber in the so-called black box via a mating sleeve. The black box is a feedthrough located on top of the ADR. On the CCD side, the light is sent to the chip after crossing a collimator.

Optimization of such a setup was necessary. This improvement work can be divided in three different phases. The details of the upgrades can be found in the following section.

4.2 Detection efficiency optimization

A low detector DE can be caused by many factors. In our case, the first parameters that have been considered as potentially problematic are the quality of the optical fibers used in the test as well as the optical efficiency of the various connections using FC/APC connectors[5].

The standard optical fibers that are used in ALPS setup are step-indexed fibers made of silica. The cladding and the core of the fiber have different

---

[4]The Wr output receives 80 % of the photons and the R receives 20% when the laser is connected to the input labelled Wb.

[5]FC stands for Ferrule Connector. They can be of two kinds: APC (Angled Physical Contact) and PC (Physical Contact).

refractive indices with $n_{cladding} > n_{core}$ (see Fig. 4.3). The light propagating inside the core will be completely reflected at the interface core/cladding if the incident angle is larger than a critical angle θ_c which can be expressed as [35]:

$$\theta_c = \arcsin(n_{cladding}/n_{core}) \qquad (4.3)$$

Losses can also be induced by a defective coupling of two fibers. Two techniques have been used. The FC/APC connectors are user-friendly. Indeed, such connections can easily be done or undone. However, such connections were proven to be in our case unreliable and unreproduceable with fluctuations in the connection efficiency as high as 50 %. The second method is called fusion-splicing and consists in fusioning both fibers together. Such a connection requires more efforts than the previous one but demonstrates good stability and very high efficiency. Additional examples of possible fiber losses are depicted on figure 4.3.

It was decided to create a robust and stable fiber setup. All FC/APC connectors have been replaced by fusion-splices of the fiber (losses of 0.1 dB) (see Fig. 4.8). Results of the different test phases have been summarized in table 4.1. Each measurement will be discussed in a dedicated section.

Test setup	Laser λ (nm)	Laser	TES A/CCD	TES B/CCD
1	1059	58-FCM	≈ 0.001	≈ 0.001
2.1	1059	58-FCM	≈ 15	≈ 10
2.2	1072	51-nano-FCM	-	-
3	1072	51-nano-FCM	≈ 60	≈ 90
4.1	1072	51-nano-FCM	≈ 115	≈ 115
4.2	1072	51-nano-FCM	≈ 90	≈ 90

Table 4.1: Detection efficiency assessments - The Test Setup number is given to fiber setup including the beam splitter. Measurements with the same number but different indices are measurements taken with the same setup. TS 4.1 and 4.2 have been taken for different power levels.
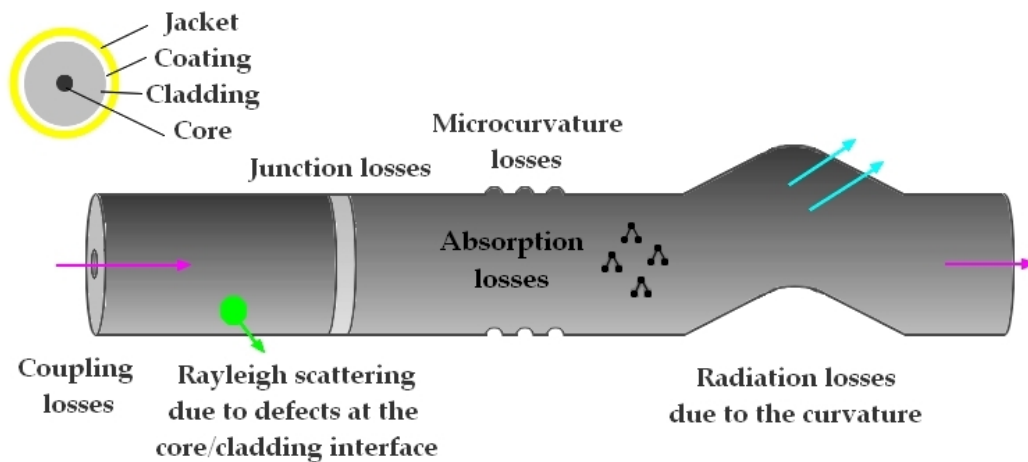
Figure 4.3: Step indexed fibers and possible losses - Fibers are made of four different layers: the core, the cladding, the coating and the jacket. The core and the cladding are the two active parts of the fiber. The coating as well as the jacket are mechanical protections. If the jacket of a fiber is removed, the left fiber is called bare fiber. Optical fibers can suffer losses of different types. Coupling losses are induced when installing a connector on the fiber. Curvature as well as microcurvature are also sources of loss. Junction losses are induced when two fibers are fusion-spliced. Furthermore, absorption losses are due to the vibrations of the silica of the lattice in the IR. Finally, in case of heterogeneity of the core/cladding interface, Rayleigh scattering can occur.

4.2.1 Test setup number 2

The test setup number 2 was performed multiple times throughout the full mounting phase in order to monitor its optical efficiency. The optical fibers located between the attenuators and the TES detectors have been replaced with new fibers. A 1x4 25:25:25:25 HI1064 fiber coupler has been spliced on the TES outputs in order to cancel the losses induced at the mating sleeve level (i.e. black box) (see Fig. 4.8). Fibers installed inside the cryostat were SMF28 fibers. Figure 4.4 shows the new principle which has been followed in this measurement.

Before splicing the fiber coupler, precise measurements of its splitting ratios have been performed. Furthermore, the coupler has been tested for backscattering. When injecting light in one of the outputs, the beam going out of another output is attenuated by a factor 10^{-5}. More measurements have been performed during the full mounting process in order to study the influence of each step. For example, cutting the FC/APC connectors resulted in an increase of 1.5 times the output power.
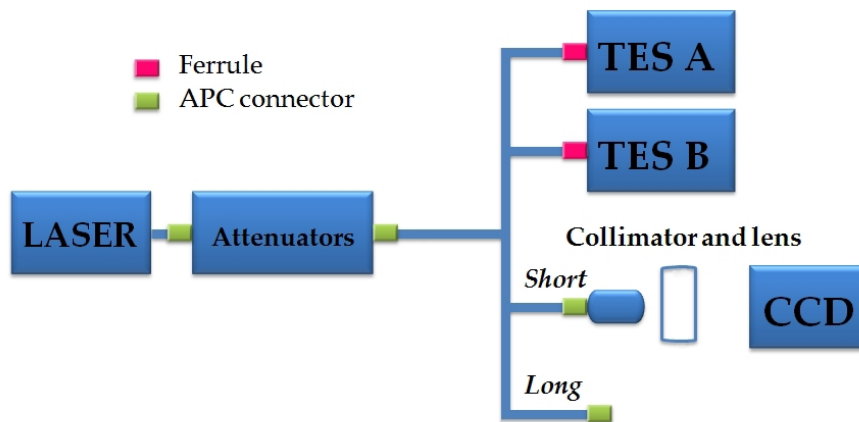
Figure 4.4: Test setup number 2 - The 1x4 25:25:25:25 fiber coupler is spliced to the fibers coupled to the TES via two splices each. Fibers inside the cryostat are approximately 2.5 m long. A lens ($f = 100$ mm) has been added upstream of the collimator. The CCD has two dedicated outputs. The short output is unchanged. The long output is mounted similarly to the TES branches: a 2.5 m long fiber has been added in the middle. The laser used for this measurement is the 51nanoFCM which corresponds to the laser used in the CCD efficiency evaluation [83].

Because two connectors were left on the CCD side, it was decided to keep one unchanged (i.e. short) and to treat the other one similarly to the TES outputs (i.e. long). Such a process allows ruling out strong effects of the mounting techniques. In TS 2.1, only the short CCD fiber was used.

To optimize the CCD camera's signal to noise ratio, 5 minutes exposure measurements were taken while numerous one second timelines (limited by our current DAQ system) were recorded with both TES detectors simultaneously. First results (i.e. TS 2.1) showed a small improvement in TES A and TES B DE (see Tab. 4.1). However, the results were apparently lowered. Indeed, the light-tightness of the CCD was very poor at that time. Background photons increased the CCD count rate. As a consequence, the TESs efficiency seemed virtually lower.

For a second test phase (i.e. TS 2.2), the full setup was covered with black light-tight fabric purchased from Thorlabs. This resulted in a much better TES efficiency evaluation. However, by using both CCD outputs (i.e. short and long) it was noticed that results were very unstable. In the short fiber measurement, TES A efficiency was evaluated to be 100 times higher than
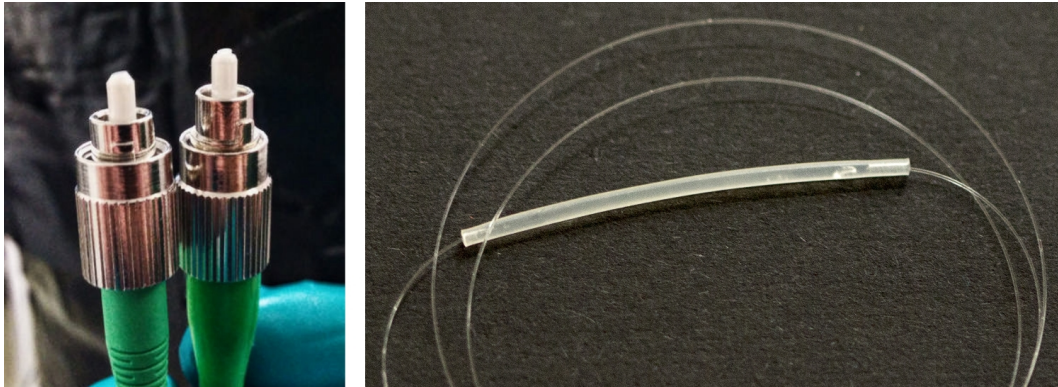
Figure 4.5: Different types of connections - The picture on the left shows the two different types of connectors that have been used on the CCD side with TS 2. The left APC ferrule is of the standard type. The picture on the right side shows a fiber fusion-spliced similarly to what is used inside the cryostat. Metallic splice protection tubing should be avoided as some types of stainless steel become magnetic under cryogenic temperature.

the CCD one. With the long fiber, the results would only be 60 times better. In the end, this effect was understood and solved. It was caused by the non-standard ferrule of the fiber coupler which was not compatible with the collimator fiber connector. This has led to clipping and instabilities (see Fig. 4.5). For TS 3, the connectors have been replaced successfully with standard ferrules.

4.2.2 Test setup number 3

With the test setup number 3, the TESs DE was evaluated by using a similar setup to the one used for the TS 2 (see Fig. 4.4). Corrections to the beam splitter ratios linked to the non-perfect distribution of the input power were made (28:27:22:23), leading to a good estimation of the ALPS Transition-Edge Sensors DE. In this test, TES A was 55 ± 5 times more efficient than the CCD and TES B was 80 ± 10 times more efficient than the CCD.

The estimation obtained during this measurement was far from meeting our expectations. Either the TES QE was lower than expected or the CCD was in the end not so well known. Many different factors which could decrease the efficiency of the ALPS detector have been listed and, for a large part, ruled out.

Obstruction of the TES detector - Both TESs' surfaces have been checked

with a microscope to determine if dust was obstructing them. Deposits were found around both TESs, but no particles was seen on the detector itself, ruling out a sizeable obstruction.

Separation of the fiber end from the TES - Dirt discovered on the area surrounding the TES could induce a tilt of the fiber or a large free space between the fiber end and the detector's surface. It has been shown by NIST that a gap in the warm larger than $20\,\mu$m would cause a severe decrease in Transition-Edge Sensors quantum efficiency[6] [56]. Following the microscope study of the quality of the connection, this hypothesis was also ruled out.

Fiber in the cold - It was shown that the detection efficiency of the detector system highly depends on the behavior and quality of the fibers used within the second part of the fiber coupler (i.e. outputs). Work has been done to optimize the setup by reducing losses. All the mating sleeves used in the second part of the setup had already been replaced by fusion splices (losses of 0.02 ± 0.01 dB). The ratio of each output has proven to be independent from the power input. However, at low temperatures the efficiency of the two fibers coupled to the detectors could be decreased causing then a degradation of the TES detection efficiency. Indeed, fiber suppliers only insure fibers functioning up to $70\,$K. In order to test this parameter, a fiber has been installed so that it enters the cryostat, goes up to the $80\,$mK stage and comes back through all the stages again up to the room. Measurements of a few hours each have been taken during various stages of a cool-down. This test has shown that the fiber efficiency has a variation of 1% only (dominated by the instability of the laser over time) if the fiber is placed in a temperature gradient of approximately $300\,$K (see Fig. 4.6).

Damage to the TES coating - The possibility of the degradation of the anti-reflective coating of the device has been considered. This layer is however protected by a layer of silicon oxyde (SiO_2) which is approximately $200\,$nm thick. The mechanical deterioration of this layer is unlikely. However, measurements of both TESs' detection efficiency for various wavelengths would have allowed to clarify this point as a large difference should be seen between red, green and IR photons (see Fig. 4.7). This test was not performed.

Misalignment of the fiber end - It has been shown by NIST that a fiber/TES misalignment would cause a reduced coupling efficiency [56]. For such

---

[6]This depends on the Numerical Aperture (NA) and core radius of the chosen fiber. These tests were performed with SMF28 optical fibers.
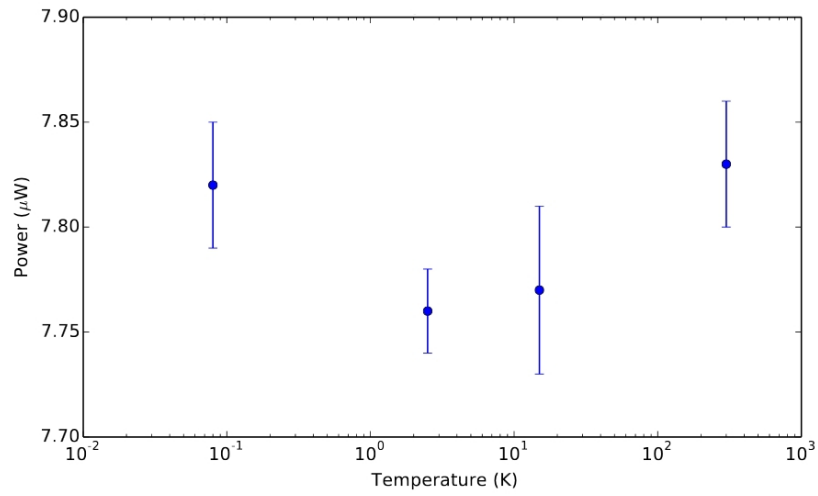
Figure 4.6: Power measured at the end of a fiber traversing the ADR and going back outside at different temperatures (80 mK, 2.5 K, 15 K, 300 K).
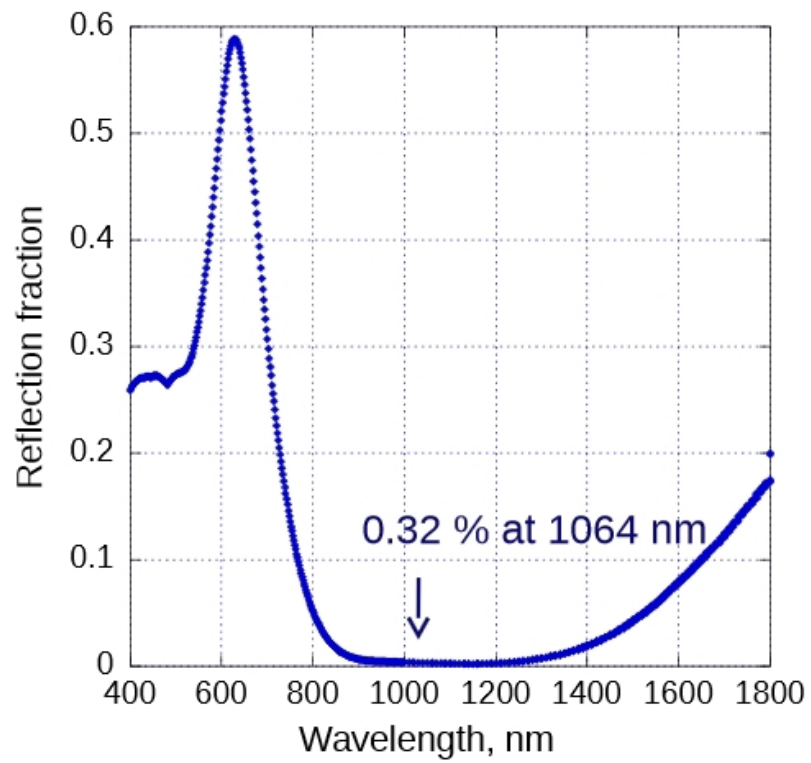
Figure 4.7: Reflectivity of the TES depending on the photon wavelength (source: NIST).

measurements, an IR laser is shone on the chip and the picture of the backside is studied. However, such tests are usually performed before the aluminium oxide (Al_2O_3) ferrule is placed behind the detector chip and is part of the alignment procedure. The additional ferrule makes the choice in the laser wavelength rather complicated. The silicon substrate will not let the visible light go through. The crystal "ferrule" located on the back of the detector will not let far infrared photons go through.

In the end, the focusing of the CCD was of poor quality during the measurements, causing a very low signal to noise ratio at such a low photon rate. The improvement of the focusing via modification of the CCD optical setup was performed, in order to induce an enhancement of the precision of the TES detection efficiency in future measurements.

Another important improvement of the setup comes from the work which has been done at the optical fiber level. In the past, fibers were of heterogeneous kind. It was decided to replace the full setup with HI1060 flex fibers only. The operating wavelength of this singlemode fiber is 980 nm. The SMF28 standard singlemode fibers that were used in the past had the drawback of acting as multimode fibers at 1064 nm[7]. A fiber coupler with one input and four outputs has been custom made for our setup by the company SEDI-ATI (see Fig. 4.8). The coupler has then been connected on the TES side to ferrule endings with an antireflective coating treatment (i.e. dielectric coating).

4.2.3 Test setup number 4

In March 2016, data were collected with the improved setup (i.e. TS 4). The general method for this measurement has not been modified compared to the previous tests. However, the optical setup of the CCD camera has been upgraded. Improving the focus of the beam allowed an optimization of the signal-to-noise ratio. The beam size was reduced to about 2x2 pixels [89]. This improvement allowed a better precision on the TES efficiency evaluation by reducing the error margin on the CCD counts.

The beam splitter ratio has been measured at each step of the installation. During the measurements, runs with both the long and the short CCD endings were successively taken. Results can be found in table 4.2.

---

[7]It depends on the modal dispersion of the fiber and its core radius.

RUN	TES	Counts (γ/s^{-1})	CCD output	Counts (γ/s^{-1})
1	A	1998 ± 17	3	18 ± 1
1	B	2048 ± 17	3	18 ± 1
2	A	1854 ± 19	4	16 ± 1
2	B	1887 ± 20	4	16 ± 1
3	A	2527 ± 22	3	27 ± 1
3	B	2605 ± 22	3	27 ± 1

Table 4.2: Results of test setup 4.1 - Normalised counts for each run and detector. The dark count as well as the beam splitter ratio have already been taken into account.

By computing the ratio of TES counts over CCD counts, it is possible to say that the TESs are on average 108 ± 10 times more efficient than the Pixis CCD camera. Additional data (TS 4.1) have been taken with a lower input power (approx. 0.5 kHz on the TES side). On average, the TESs have been found 91 ± 10 times more efficient than the CCD camera. The detection efficiency of the TES detectors does not depend on the input power.

In order to conclude with a precise detection efficiency for both TESs, it would be necessary to estimate the overall efficiency of the CCD. The latter takes into account the quantum efficiency, the optical efficiency as well as the analysis efficiency. However, it has been shown that both lasers, which were used in these tests, present a broadened spectrum at low power input [89]. The CCD efficiency is highly dependent on the wavelength at these energies.

In a nutshell, if such a technique gives a good estimation of the relative efficiency of the TES compared to the CCD's, it is not meant to be used for an absolute measurement of the TES efficiency. From February 2014 to April 2016, the detection efficiency of the detector system was improved by a factor of approximately 100 000 (i.e. from QE 1 to QE 4, see Tab. 4.1). Additional tests would be necessary in order to determine if this increase in sensitivity would be sufficient for ALPS IIc.
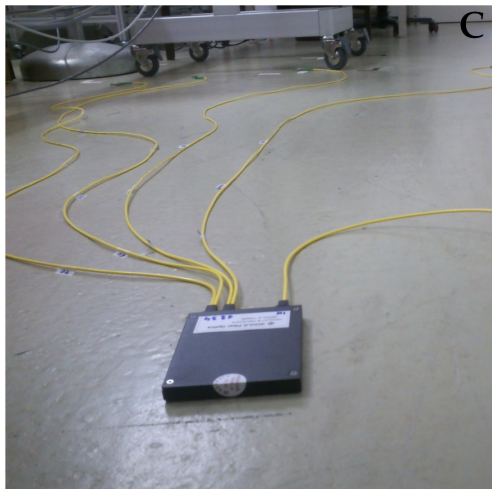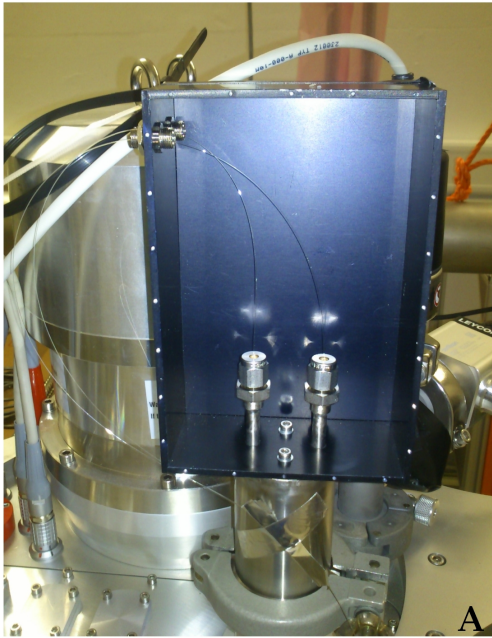
Figure 4.8: A few pictures of the DE measurement setup - **A**) Picture of the black box feedthrough. The fibers go through the mating sleeve. No connector is used. **B**) Picture of the test setup number 4. The fiber coupler is attached to the ADR outter shielding. **C**) Picture of the 1x4 custom-made SEDI-ATI fiber coupler. **D**) Picture of the home-made light-tight shielding which started being used arount the TS 3.

5 Background characterization

The intrinsic dark count rate of the TES (i.e. measurement without fiber attached to the TES) has been measured to be of about 10^{-1} counts/sec inside the total triggered window (see Fig. 5.1). It results in approximately 10^{-4} counts/sec in our region of interest (i.e. about 1 pulse every 2.5 h with the pulse height value higher than -30 mV). When the highest efficient fiber setup is attached to the detector (see Sec. 4) this rate is increased by three orders of magnitude (see Fig. 5.2). The aimed dark count rate of the TES for ALPS IIc is of 10^{-6} counts/sec [11]. It is in this context that an identification work of the different background sources has started. In the following chapter, these studies will be described and possible means of reducing the background are proposed.

Four main sources of background will be studied. In a first section, the background constituted of visible photons will be considered. In a second section, the thermal background will be discussed. In a third section, muon influence on the background will be studied. Finally, the influence of the natural radioactivity will be examined in a last section.

5.1 Visible light

Visible (VIS) light represents a source of background for the ALPS detector. Indeed, as seen in figure 4.7, the detector has a good efficiency to VIS light. Two sources of VIS photons can be considered. Firstly, ambient light could enter into the cryostat in the case where the light-tightness of the dewar would not be sufficient (see Sec. 5.1.1). Moreover, ambient photons could be transported to the TES by the optical fiber. Secondly, green light will be used in the regeneration cavity, which makes it essential for the detector to be able to differentiate green and IR photons [44].

In order to do this, one of the essential characteristics of the detector is its linearity. Indeed, if the detector's response depends directly on the photon energy, it is then possible to easily identify single-photons. Such a test has been performed and will be described in section 5.1.2.
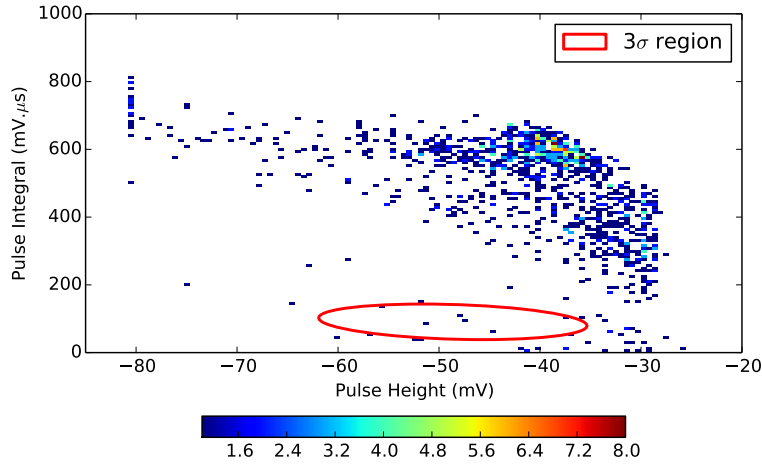
Figure 5.1: Counts obtained with a Noise setup - The setup is depicted on figure 3.1. This result was obtained with CHB during CD 48. The data-taking time was of 13 hours 40 minutes. The rate of triggered events (TL = -30 mV) was of $2.30(7) \cdot 10^{-2}$ counts/sec. The 3-σ region counted $1.42(5) \cdot 10^{-4}$ counts/sec.
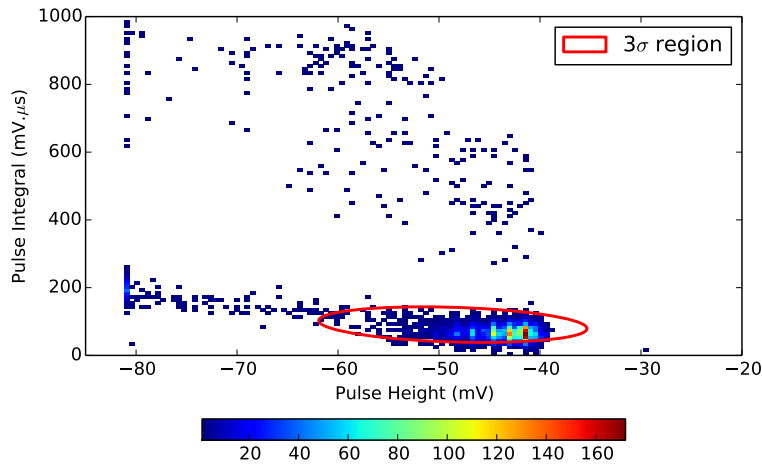
Figure 5.2: Counts obtained with a Background setup - The setup is depicted on figure 3.1. This result was obtained with CHB during CD 49. The data-taking time was of 4 hours 20 minutes. The rate of triggered events (TL = -38 mV) was of $3.85(5) \cdot 10^{-1}$ counts/sec. The 3-σ region counted $3.26(5) \cdot 10^{-1}$ counts/sec.

5.1.1 Light tightness

In order to quantify the ADR's light-tightness, two optical fibers were installed, going from outside to the top of the 70 K plate. Fiber number 1 was ended on the part of the 70 K plate located in front of the detector. Fiber number 2 was attached to the part of the 70 K plate which is located behind the detector. Their optical efficiencies in the ADR were measured before and after the cool-down. They were of approximately 75% during each measurement period.

For this test, the black box's light-tightness (i.e. feedthrough) was obtained by covering it with black tape. Measurements were taken for both channels in two different environments. Firstly, a *dark-laboratory* measurement was performed while all lights were turned off. Secondly, in the case of the *shiny-laboratory* measurement, the intensity of the ambient light was maximized. A summary of the final results can be found in table 5.1.

Channel	Setup	Passed TL (counts/sec)	3σ-region (counts/sec)
	Dark lab	$5.7(3)\cdot10^{-3}$	$1.7(5)\cdot10^{-4}$
A	Shiny lab	$8.1(4)\cdot10^{-3}$	$5.1(3)\cdot10^{-4}$
	Noise CD 30	$7.1(3)\cdot10^{-3}$	$4.1(8)\cdot10^{-4}$
	Dark lab	$1.26(4)\cdot10^{-2}$	$1.7(5)\cdot10^{-4}$
B	Shiny lab	$1.23(4)\cdot10^{-2}$	$1.2(4)\cdot10^{-4}$
	Noise CD 30	$1.26(4)\cdot10^{-2}$	$3.2(7)\cdot10^{-4}$

Table 5.1: Light-tightness test 1 - Counts obtained for CHA and CHB in two different light environments. The results are compared to the intrinsic dark counts measurement performed during CD30. Indeed, the Noise count represents a lower limit, which is reached in case of light-tightness.

Considering the current intrinsic dark counts (i.e. same order of magnitude than dark counts), these results demonstrate that the setup is sufficiently light-tight at the outer shielding level. In order to control the inner light-tightness of the device, the test was repeated by taking three sets of five 1 sec-timelines. The first set corresponds to Background data. In the second set, the laser was shone to fiber number 1. Finally, the third set of data was taken by sending 1064 nm photons to fiber number 2. Results can be found in table 5.2.

Channel	Setup	3σ-region (counts/sec)
	Background	0
A	Fiber 1	0
	Fiber 2	0.6 ± 0.3
	Background	0
B	Fiber 1	0
	Fiber 2	1.2 ± 0.5

Table 5.2: Light-tightness test 2 - Counts obtained for CHA and CHB by shining a 1064 nm laser in two different fibers. Fiber 1 ends on the 70 K plate, behind the detector, while fiber 2 is located in front of the detector on the same cooling stage. The results are compared to Background counts. No event fell in the 3-σ region for the Background and fiber 1 setup.

In conclusion, though the outer and 70 K shieldings seem to be rather well light-tight (see Tab. 5.1), the 4 K shielding light-tightness could still be improved (see Tab. 5.2).

5.1.2 Background rejection

In order to study the detector's response to photons of different energies, four different lasers were shone on the detector (see Tab.5.3). All measurements were performed during the same recharge. As a consequence, the fiber coupled to the detector (SMF28) was not modified in between measurements[1]. Multiple histograms were taken with each laser (see Fig. 5.3). The power of the laser has been adjusted with as many attenuators as necessary in order to have comparable background and signal peaks.

Wavelength (nm)	Power (mW)	Type
1064	< 1	Commercial laser
635	< 1	Commercial laser
501-561	< 500	Modified commercial laser
405 ± 10	85	Laser pointer

Table 5.3: Laser used during linearity measurement - The power and wavelength information are given according to the manufacturer notes. The green laser (501-561 nm) spectrum shows anomalies. It includes three peaks. One at 532 nm, one at 804 nm and finally, one at 1064 nm. The second peak is dominating.

In Figure 5.4, the average PH is shown as a function of the energy of the photons which are absorbed by the detector. The sensors are linear in our

---

[1]The fiber does not match perfectly with every tested wavelength.
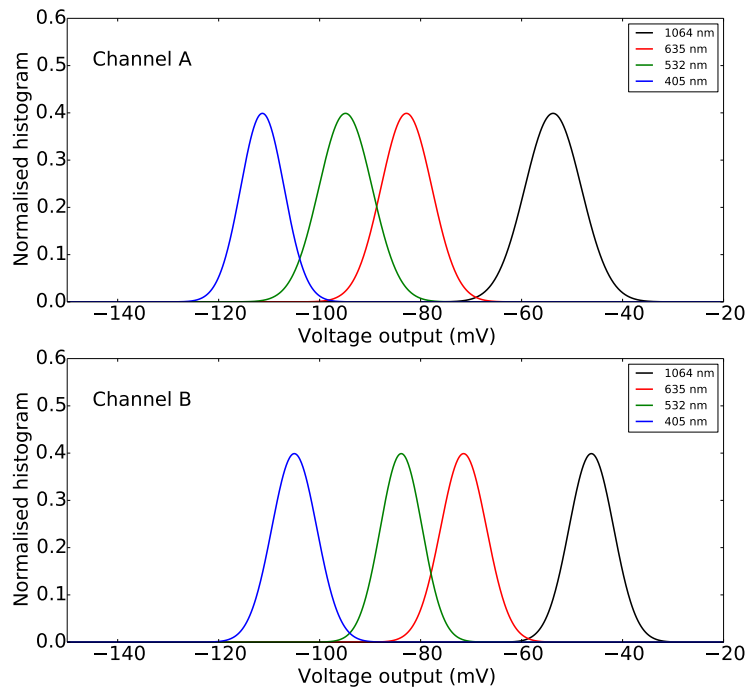
Figure 5.3: Normalised histogram for each laser - This plot shows the mean voltage output which corresponds to the detectors' response to various wavelengths. One can see that CHA and CHB responses are shifted. Indeed, this parameter is proper to each detector and depends on the design of the latter (see Eq. 3.2).
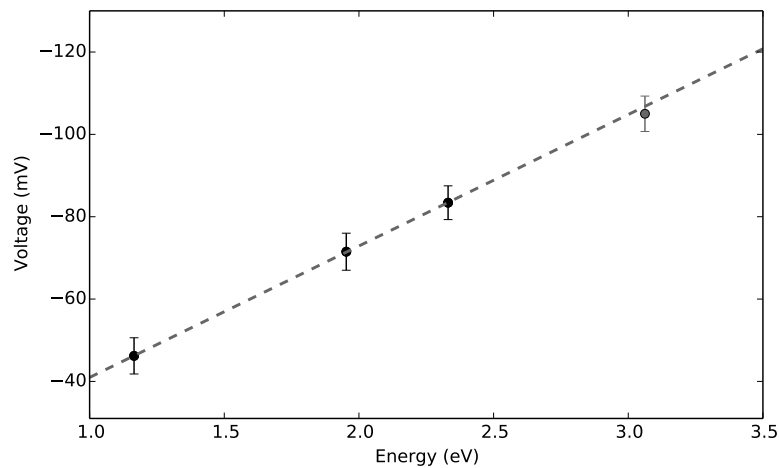
Figure 5.4: TES B linearity - Average pulse height in units of voltage output as a function of photon energy for TES B. The dashed line is a fit to the first three points.

region of interest (1.17 eV). The non-linearity at higher energies (E > 3.0 eV) matches expectations. It is due to the saturation of the detector. The energy resolution was measured to be of $\Delta E/E < 10\%$ at 1.17 eV and of $\Delta E/E < 5\%$ at 2.33 eV. Concerning CHA, similar results can be found in [30].

The linearity of the detector offers a good tool to differentiate photons of different energies (i.e. comparison of their PH). This possibility to separate photons is quantified by the detector's energy resolution (i.e. minimal difference in energy which can be detected). As can be seen on figure 5.3, green photons should not be an issue for the ALPS II experiment as their signal region is not expected to leak in the ALPS ROI[2].

5.2 Black body photons

Compared to the Noise setup, the Background setup shows a large increase in background events[3]. In reference [29], it was suggested that these additional counts could be connected to thermal events. Various tests and computations were performed in order to determine how much of an influence the thermal background has on the ALPS II detector setup.

Two possible sources of black body photons (BBPs) have been considered: photons in the surroundings of the fiber (see Sec. 5.2.1) and photons emitted by the fiber itself (see Sec. 5.2.2).

5.2.1 Black body photons emitted in the surroundings of the fiber

The spectral density of electromagnetic radiation emitted by a black body in thermal equilibrium at a given temperature T is given by Planck's law [64]. The spectral radiance indicates how much BBPs will be emitted by a black body. It is expressed as:

---

[2]This statement becomes wrong for high intensity. The intensity of the green beam will be limited in order to protect the coating of the mirrors.

[3]Background events with a small b are events falling in the ROI even if no 1064 nm photon source is connected to the setup.

$$L = \int_{\lambda_1}^{\lambda_2} \frac{2hc^2}{\lambda^5} \frac{1}{\exp(\frac{hc}{k_b \lambda T}) - 1} d\lambda \quad [\mathrm{W} \cdot \mathrm{m}^{-2} \cdot \mathrm{sr}^{-1}] \tag{5.1}$$

with h the Planck constant, c the speed of light and k_B, the Boltzmann constant. L depends on the temperature T of the blackbody. The number of BBPs (N_{BBP}) which will enter an optical fiber through its connector in an energy range [E_1 - E_2] of the order of the energy resolution[4] is of:

$$N_{BBP} = \frac{LS\Omega}{E} \tag{5.2}$$

$$\begin{cases} S &= \pi(d/2)^2 \quad \text{Surface of the fiber end} \\ E &= \frac{hc(\lambda_1 + \lambda_2)}{2\lambda_1 \lambda_2} \quad \text{Energy range} \\ \Omega &= 2\pi(1 - cos\theta) \quad \text{Solid angle of acceptance} \\ \theta &= sin^{-1}(NA) \quad \text{Numerical aperture of the fiber} \end{cases}$$

This results in a rate of approximately 10^{-5} counts/sec in our ROI for an ambient temperature in the laboratory of 293 K. Black body photons' dependence on the temperature can be seen on figure 5.5 for two different fiber types.

Another source which was considered is connected to BBPs hitting the fiber from the side. Because of the fiber geometry, independently of the refractive indexes, the outcome will always be the same. Indeed, in step-index fibers, we have $n_{core} > n_{cladding} > n_{coating}$. According to Snell's law, a photon which will enter the fiber through its coating will only go through the fiber and will therefore not contribute to the final rate (different behavior if the fiber is bent).

In our energy range, such photons are not a dominating background. However, pile-ups of low energetic photons (i.e. $\approx 0.8\,\mathrm{eV}$) could be the main source of our high Background excess (i.e. when a fiber is connected to the detector) [29]. The spectral radiance at this energy is five orders of magnitude bigger than at 1.17 eV. Many proposals have already been made such as using a 1064 nm filter in the cold, or cooling down the fiber's end [29].

---

[4]The integral limits have been chosen such as λ_1= 1064 - ΔE/E and λ_2= 1064 + ΔE/E. The energy resolution at 1064 nm is of ΔE/E=10% .
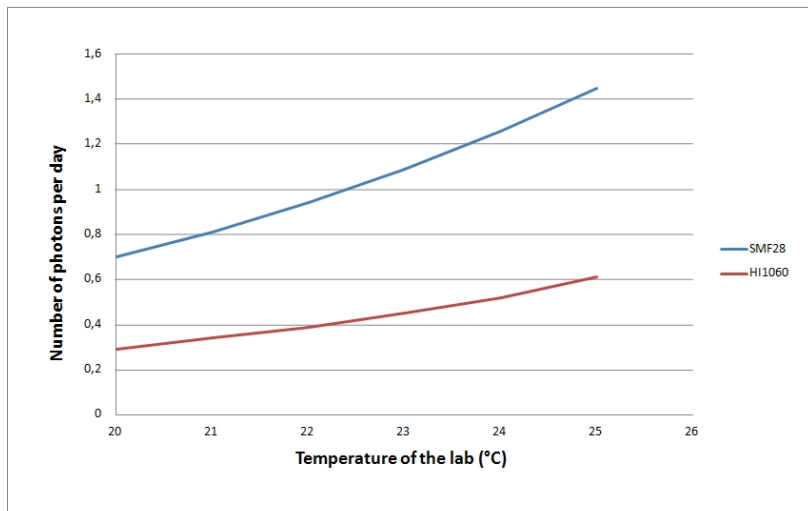
Figure 5.5: Number of photons per day entering a fiber through its end as a function of the environmental temperature. - The computations have been done for two types of fibers. SMF28 fibers have a NA of 0.14 and an inner diameter of 8.2 μm. HI1060 fibers have a NA of 0.22 and an inner diameter of 5.3 μm.
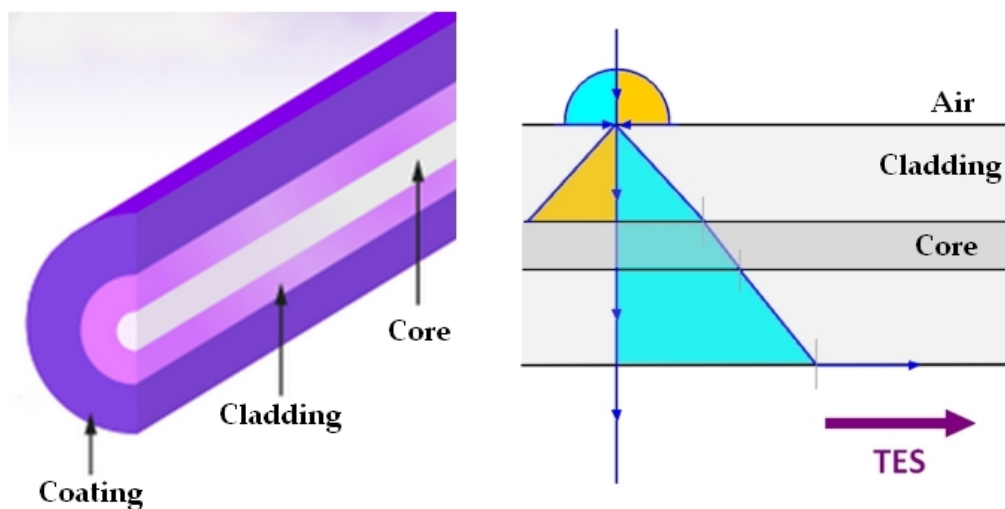
Figure 5.6: On the left, a drawing of the inner structure of a fiber can be seen (not to scale). On the right, the drawing shows the different paths that a particle entering the fiber by its length would take. The yellow part is a mirror of the blue one.

5.2.2 Black body photons emitted by the fiber itself

If an optical fiber is considered an ideal transparent medium, it should not emit BBPs. However, as can be seen on figure 5.9, they are not totally transparent. BBPs can be emitted inside the cladding, the coating or even the jacket. Photons originating from this phenomenon can have different fates depending on their propagation angle in the initial medium.

On figure 5.7, different trajectories have been drawn. The yellow portion is a mirror of the blue one. The dark blue region is divided in two different areas. The light blue region contains all the photons which get out of the fiber whereas the red one contains the photons which are transmitted by the cladding (see green arrows). A little fraction of these photons is then able to hit the detector.
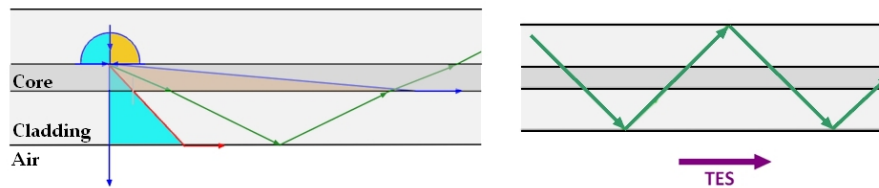
Figure 5.7: Drawings showing the different paths that a particle emitted by the fiber itself could take. The yellow part is a mirror of the blue one. The light blue region defines the angle range for which the particles would exit the fiber. The red region depicts the angle range for which BBPs would be transmitted. The green arrows give an example of a transmitted particle path inside the fiber in the direction of the detector.

As a conclusion, we could say that a little part of BBPs produced inside the fiber can be transmitted and will then participate in the final count rate[5]. The fiber length would then be expected to influence the BBPs counts and should always be minimized in a warm environment (i.e. T>70 K). However, silica optical fibers have a very strong attenuation for wavelengths $\lambda > 2\,000$ nm. It means that optical fibers are transparent to $\lambda < 2\,000$ nm, i.e. emit BBPs with $\lambda > 2\,000$ nm. In consequence, such background should be negligible in our case considering our ROI.

---

[5]The exact refractive indexes are necessary in order to determine how many BBPs emitted inside the fiber could hit the detector.
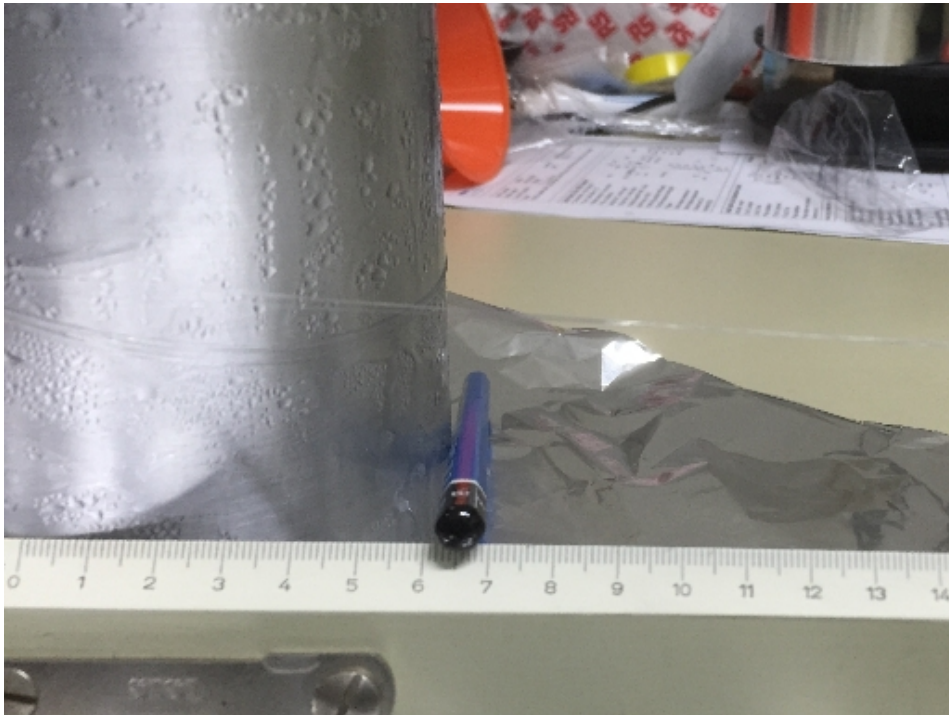
Figure 5.8: Picture of the ice cup. Two fibers have been enrolled around the metallic cup [13].
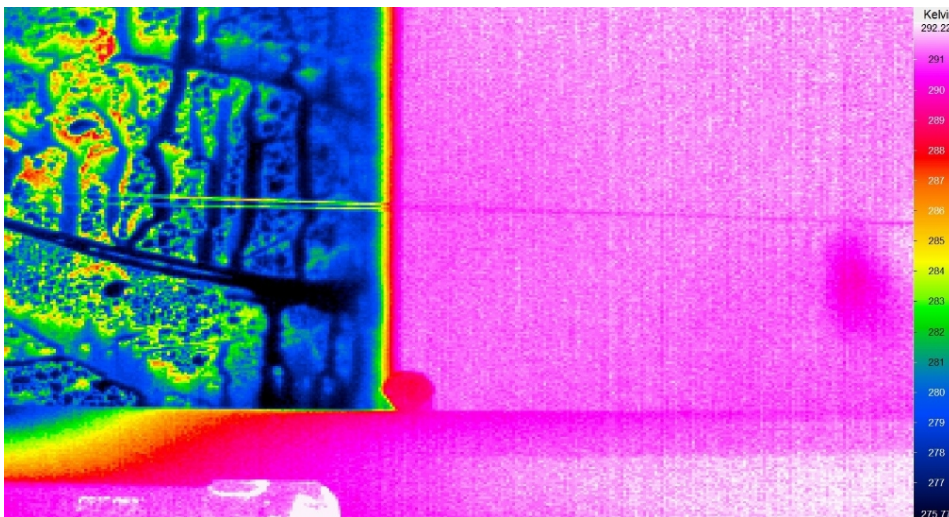
Figure 5.9: Picture of the ice cup taken with an IR camera. After one turn, the fiber has thermalised. As we can see the fiber on this picture, we can conclude that the fiber is opaque to certain wavelengths [13].

5.3 Muons

Muons represent a potential source of intrinsic dark count. Indeed, the muon flux at sea level is of approximately mf = 70 $\text{m}^{-2}\,\text{s}^{-1}\,\text{srad}^{-1}$ [16, 41]. Computations were made in order to determine whether or not an active muon shielding should be considered [45].
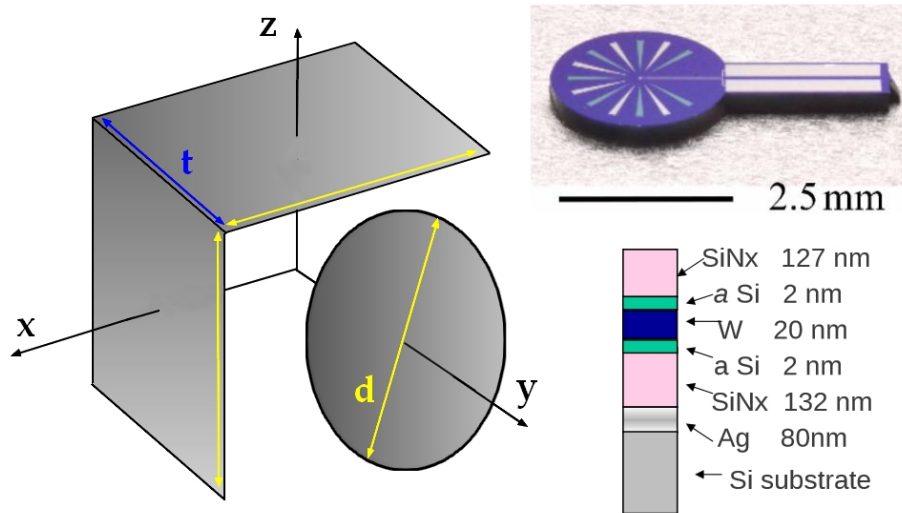
Figure 5.10: Detector geometry - On the left, the drawing depicts the simplified model used for computation. On the right, a drawing of the full TES chip [56] as well as a drawing of the different sensor layers can be seen (Source: A. Lita).

We consider that the total volume of the substrate is active. For simplification purposes, rather than treating the detector as a cylinder with d its diameter and t its thickness, it will be treated as if it was constituted of two rectangular surfaces with their normal vector pointing towards the z and x axes and of a circular area with its normal vector parallel to the y axis (see Fig. 5.10). Given the geometry of the ALPS laboratory, the maximum angle for muons to reach the detector is of θ_m=20° [6].

The three components of the cross section can be defined as follows:

$$\begin{cases} a_1 &= d \cdot t \quad \text{Cross section of downgoing muons} \\ a_2 &= (d/2)^2 \quad \text{Cross section of muons hitting the face of the detector} \\ a_3 &= d \cdot t \quad \text{Cross section of muons coming sideways} \end{cases}$$

---

[6]This angle will be even smaller for ALPS IIc which will be located underground, in one of the former HERA halls.

The integrals can be calculated in the following way:

$$r_1 = m_f \int_0^{2\pi} d\phi \int_0^{\theta_m} d\theta \sin\theta\, a_1 \cos\theta \cos\theta = \frac{2\pi}{3} a_1 m_f (1 - \cos\theta_m)$$

$$r_2 = m_f \int_{-\pi/2}^{+\pi/2} d\phi \int_0^{\theta_m} d\theta \sin\theta\, a_2 \cos\phi \sin\theta \cos\theta = \frac{2}{3} m_f a_2 \sin^3\theta_m$$

$$r_3 = m_f \int_0^{\pi} d\phi \int_0^{\theta_m} d\theta \sin\theta\, a_3 \sin\phi \sin\theta \cos\theta = \frac{2}{3} m_f a_3 \sin^3\theta_m$$

The upper limit of the muon rate (i.e. total triggered window) is then given by:

$$r_{\text{tot}} = r_1 + 2(r_2 + r_3) = 2.8 \cdot 10^{-5} \text{counts/sec}$$

This upper limit of the muon rate absorbed in the detector's substrate demonstrate that muons represent a negligible background source for ALPS II experiment.

5.4 Ambient radioactivity

The dark count rate of the ALPS Transition-Edge Sensors has been measured to be of approximately 10^{-4} counts/sec in the ROI. These counts can have different sources. Muons have already been ruled out as a dominant source for such a background. Natural radioactivity of the different materials placed near the detector is another potential source. The surrounding materials include different types of copper, aluminium, stainless steel and zirconia as well as all the different materials of the detector itself (e.g. silicon, silver, tungsten).

In order to assess the influence of natural radioactivity on the ALPS detector system, tests were performed. Multiple calibration measurements were carried out with two different radioactive sources: a 53 kBq Co^{60} source and a 280 kBq Na^{22} source. Both sources were placed in front of the cryostat, at the height of the detector. Results can be found in table 5.4.

It is possible to test whether or not gamma rays could cause the TES dark counts. We consider the case where both sources have been used. The total activity is of A_{Tot} = 333 kBq. The sources were mounted at a distance of

Source	Exposure time (min)	Trigger windows (counts/sec)	3-σ region (counts/sec)
Co^{60}	90	$6.6(4)\cdot 10^{-2}$	$4(3)\cdot 10^{-4}$
Na^{22}	105	$2.56(6)\cdot 10^{-1}$	$1.3(4)\cdot 10^{-3}$
Co^{60} + Na^{22}	105	$2.91(7)\cdot 10^{-1}$	$5(3)\cdot 10^{-4}$
-	820	$2.3(7)\cdot 10^{-2}$	$1.4(5)\cdot 10^{-4}$

Table 5.4: Calibration measurements of CHB - Measurements taken with radioactive sources have been compared to Noise measurements without any source. There is an increase in counts in the triggered region as well as in the 3-σ region when the source is installed next to the cryostat.

r=0.20 m. The expected rate of events N_γ is given by:

$$N_\gamma = \frac{A_{Tot}}{4\pi r^2} \cdot a_{\text{eff}}$$

The expected rate is then set equal to the measured rate, $N_\gamma = r_{\text{measured}} = 1610/6000\,\text{s}^{-1} = 0.27$ counts/sec, in order to obtain the effective area, equal to:

$$a_{\text{eff}} = \frac{4\pi r^2 N_\gamma}{A_{Tot}}$$

Finally, this results in an effective radius of $r_{\text{eff}} = \sqrt{\frac{a_{\text{eff}}}{\pi}} = 0.36\,\text{mm}$. This means that triggered signal is produced when the detector substrate is hit within 0.36 mm radial distance of the sensitive part of the detector.

The natural background radiation dose rate of the ADR has been measured to be of 0.1 μSv hr^{-1}. An average dose conversion is assumed for gammas of this energy to be of 0.35 GBq^{-1}mSv hr^{-1} m^2 [82]. The flux per solid angle can then be estimated as:

$$I_\gamma = \frac{1}{4\pi} \frac{10^{-4}\,\text{mSv hr}^{-1}}{\text{GBq}^{-1}\,\text{mSv hr}^{-1}\,\text{m}^2} = 0.35\cdot 10^5 \frac{1}{4\pi} \frac{1}{\text{m}^2\,\text{s}}$$

The angular acceptance is assumed to be uniform. The resulting rate is of:

$$\dot{n}_\gamma = \int d\Omega I_\gamma \pi r_{\text{eff}}^2 = 1.42\cdot 10^{-2}\,\text{counts/sec}$$

Approximately 1.42$\cdot$10^{-2} counts/sec are expected in the total triggered window considering the ambient radioactivity in the cryostat. The ratio of the 3-σ events and the triggered events is of 10^{-2} counts/sec. It can be extrapolated by saying that ambient radioactivity is expected in our ROI to be of 10^{-4} counts/sec. If these values are compared to the Noise counts (see Tab. 5.4), it is possible to conclude that natural radioactivity is the source

of the dark count rate in the Noise setup as mentionned above. It could be reduced by using radiopure components in the immediate vicinity of the detector.

In 2016, three cryostat' samples were sent to the Underground Laboratory of Modane in order to be tested with Gentiane, a high-purity germanium diodes [25]. **Sample 1** was 53.3 g of copper similar to the one used by Entropy GmBh inside the cryostat. **Sample 2** was 21 units of TES fiber endings (i.e. ferrule and metallic part around the ferrule). Finally, **sample 3** was 59 units of bare ferrules[7].

These samples have been picked for their proximity to the detector as well as for the reputation of their material concerning "high natural radioactivity". For instance, zirconium may have traces of uranium and thorium (up to 1%) in its crystal structure. The waste radionucleides content of zircon ($ZrSiO_4$) transformation into zirconia (ZrO_2) has been measured by the International Atomic Energy Agency to be of 1200-2500 Bq/kg for Th and 3700-7400 Bq/kg for U [5].

Results obtained at the Underground Laboratory of Modane demonstrated that the natural radioactivity of the copper used to build the full cryostat is comparably low ruling out any contamination [25]. However, it has been shown that the zirconium ferrules are not radiopure and would therfore not be considered for rare events experiments[8] (see Tab. 5.5).

Sample	U^{238} (mBq/kg)	Th^{232} (mBq/kg)	U^{235} (mBq/kg)
2	2076 ± 83	1152 ± 100	3386 ± 244
3	2040 ± 45	376 ± 6	303 ± 112

Table 5.5: Results of measurements at the Underground Laboratory of Modane - Results are given for samples 2 and 3 which showed a "high" natural radioactivity. The difference betwenn both samples is the presence or not of the metallic structure. The metallic part attached to the ferrule connector is a high source of ambient radioactivity. Sample 1 is negligible. (Source: [25])

Assessments of each piece of the system would need to be performed in order to identify and then minimize every background source. Natural radioactivity has proven to be a dominant source of dark counts at the level of the ALPS detector.

---

[7]Ferrules are made out of zirconium.
[8]Results have been shared by Edelweiss collaborators.

6 Conclusion

ALPS II experiment (DESY, Hamburg) follows the light-shining-through-the-wall concept. It aims at an increase in sensitivity of 3000 compared to ALPS I, mainly by a regeneration cavity and additional magnets. A tungsten Transition Edge Sensor operating below 100 mK has been successfully used to detect single-photons in the near-infrared (see Chap. 1).

The ALPS II Adiabatic Demagnetization Refrigerator has been upgraded. The preservation protocol has been optimized in order to maintain the dewar at 2.5 K for an extended period of time with a temperature drift as low as 5 mK/day (see Chap. 2).

Owing to the high ambient magnetic field present in the ALPS laboratory, a magnetic shielding has been developed. The source of the field is still to be identified and understood. However, the magnetic shielding that has been created turned out to be efficient and therefore successful (see Sec. 2.2.2).

The detector setup has proven to be stable during a recharge (i.e. period of data-taking) with a fluctuation of the average pulse height for 1064 nm photons lower than 5% (see Chap. 3).

ALPS IIc requires from the detector a high detection efficiency which, in the end, depends on the TES quantum efficiency and on the fibers optical efficiency. It is within this context that emphasis was placed on the improvement of the fiber setup. The detection efficiency has been enhanced by a factor 100 000. Further measurements are necessary in order to determine whether or not the absolute efficiency of the detector will meet ALPS IIc requirements (see Chap. 4).

At the same time, a work of background identification has been conducted. Indeed, the intrinsic dark count rate of the detector has proven to be dominated by natural radioactivity. The background of the detector (i.e. dark counts when the optical fibers are attached) could be caused by thermal photons. Efforts still need to be deployed towards a rejection of all background events in order to reach the ALPS II limit (see Chap. 5).

In conclusion, it is undeniable that this detector system is very promising concerning its potential usage in the Any Light Particle Search II experiment. However, additional work is still crucial in order to meet the experiment requirements.

Appendix A – Acronyms

ADR Adiabatic Demagnetization Refrigerator

ALPS Any Light Particle Search

BBP Black Body Photon

CCD Charge-Coupled Device

CHA Channel A

CHB Channel B

DC Dark Count

DE Detection Efficiency

DESY Deutsches Elektronen-Synchrotron

FAA Ferric Ammonium Alum

GGG Gadolinium Gallium Garnet

NIST National Institute of Standards and Technology

OE Optical Efficiency

PH Pulse Height

PI Pulse Integral

PTB Physikalisch-Technische Bundesanstalt

QE Quantum Efficiency

ROI Region Of Interest

SQUID Superconducting Quantum Interference Device

TES Transition-Edge Sensor

WISP Weakly Interacting Sub-eV/Slim/Slight Particle

Bibliography

[1] Anodizing world. `http://3.bp.blogspot.com/_yY4uYhynwG4/SffdvraPsRI/AAAAAAAAAVY/9G3PTKovZXQ/s400/galvanic+corrosion.jpg`. Accessed: 2016-11-10.

[2] Internationales geomagnetisches Referenzfeld, howpublished = `http://www-app1.gfz-potsdam.de/declinationcalc/`, note = Accessed: 2016-11-10.

[3] MIT experimental cosmology and astrophysics laboratory. `http://web.mit.edu/figueroagroup/ucal/ucal_tes/index.html`. Accessed: 2016-11-10.

[4] P. A. R. Ade et al. Planck 2013 results. XVI. Cosmological parameters. *Astron. Astrophys.*, 571:A16, 2014.

[5] International Atomic Energy Agency. Report number 419.

[6] Simon C Andrews, Ian Norton, Arvindkumar S Salunke, Helen Goodluck, Wafaa S.m. Aly, Hanna Mourad-Agha, and Pierre Cornelis. Control of iron metabolism in bacteria. *Metal Ions in Life Sciences*, 12:203–239, 12 2013.

[7] Paola Arias et al. WISPy Cold Dark Matter. *JCAP*, 1206:013, 2012.

[8] Paola Arias, Joerg Jaeckel, Javier Redondo, and Andreas Ringwald. Optimizing Light-Shining-through-a-Wall Experiments for Axion and other WISP Searches. *Phys. Rev.*, D82:115018, 2010.

[9] E Armengaud, Q Arnaud, C Augier, A Benoit, L Bergé, T Bergmann, J Blümer, A Broniatowski, V Brudanin, P Camus, et al. Axion searches with the edelweiss-ii experiment. *Journal of Cosmology and Astroparticle Physics*, 2013(11):067, 2013.

[10] S. Aune et al. CAST search for sub-eV mass solar axions with 3He buffer gas. *Phys. Rev. Lett.*, 107:261302, 2011.

[11] Robin Baehre et al. Any light particle search II Technical Design Report. *JINST*, 8:T09001, 2013.

[12] Noemie Bastidon, Dieter Horns, and Axel Lindner. Quantum Efficiency Characterization and Optimization of a Tungsten Transition-Edge Sensor for ALPS II. *J. Low. Temp. Phys.*, 184(1-2):88–90, 2016.

[13] Noemie Bastidon and Yixuan Zhang. Internal communication.

[14] John R. Baylis. Treatment of water to prevent corrosion1. *Industrial & Engineering Chemistry*, 19(7):777–781, 1927.

[15] Custalow Benjamin David. Master thesis - Influences of water chemistry and flow conditions on non-uniform corrosion in copper tube.

[16] Juerg Beringer, J-F Arguin, RM Barnett, K Copic, O Dahl, DE Groom, C-J Lin, J Lys, H Murayama, CG Wohl, et al. Review of particle physics particle data group. *Physical Review D (Particles, Fields, Gravitation and Cosmology)*, 86(1):010001, 2012.

[17] J. Beyer et al. Flux-trapping in narrow-line niobium dc squid current sensors. In *ASC 2012*, Portland, Oregon, Oct. 7-12 2012.

[18] T.R. BOTT. {CHAPTER} 12 - biological growth on heat exchanger surfaces. In T.R. BOTT, editor, *Fouling of Heat Exchangers*, Chemical Engineering Monographs, pages 223 – 267. Elsevier Science B.V., Amsterdam, 1995.

[19] Laboratory Brill and Steinmann. Internal communication.

[20] Yongyao Cai, Yang Zhao, Xianfeng Ding, and James Fennelly. Magnetometer basics for mobile phone applications. *Electronic Products*, 2012.

[21] W.G. Characklis and K.C. Marshall. *Biofilms*. Number vol. 1 in Wiley Series in Ecological and Applied Microbiology. Wiley, 1990.

[22] J. H. Christenson, J. W. Cronin, V. L. Fitch, and R. Turlay. Evidence for the 2 pi Decay of the k(2)0 Meson. *Phys. Rev. Lett.*, 13:138–140, 1964.

[23] John Clarke and Alex I. Braginski. *The SQUID handbook: Fundamentals and technology of SQUIDs and SQUID systems*. Wiley-VCH, 1 edition, August 2004.

[24] Alessandro De Angelis, Marco Roncadelli, and Oriana Mansutti. Evidence for a new light spin-zero boson from cosmological gamma-ray propagation? *Phys. Rev.*, D76:121301, 2007.

[25] M. De Jésus. Private communication, EDELWEISS collaboration (2016).

[26] Piet AJ de Korte, Henk F Hoevers, Jan-Willem den Herder, Johan A Bleeker, Wouter B Tiest, Marcel P Bruijn, ML Ridder, Remeo J Wiegerink, Jelle S Kaastra, Jan van der Kuur, et al. Tes x-ray calorimeter-array for imaging spectroscopy. In *Astronomical Telescopes and Instrumentation*, pages 779–789. International Society for Optics and Photonics, 2003.

[27] Michael Dine, Willy Fischler, and Mark Srednicki. A Simple Solution to the Strong CP Problem with a Harmless Axion. *Phys. Lett.*, B104:199–202, 1981.

[28] R. Dortwegt and E. Maughan. The Chemistry of Copper in Water and Related Studies Planned at the Advanced Photon Source. *Conf. Proc.*, C0106181:1456–1458, 2001. [,1456(2001)].

[29] Jan Dreyling-Eschweiler. *A superconducting microcalorimeter for low-flux detection of near-infrared singles photons*. PhD thesis, Universität Hamburg, 2014.

[30] Jan Dreyling-Eschweiler, Noemie Bastidon, Babette Doebrich, Dieter Horns, Friederike Januschek, and Axel Lindner. Characterization, 1064 nm photon signals and background events of a tungsten TES detector for the ALPS experiment. *J. Mod. Opt.*, 62(14):1132–1140, 2015.

[31] Dietmar Drung. High-tc and low-tc dc squid electronics. *Superconductor Science and Technology*, 16(12):1320, 2003.

[32] Klaus Ehret et al. Resonant laser power build-up in ALPS: A 'Light-shining-through-walls' experiment. *Nucl. Instrum. Meth.*, A612:83–96, 2009.

[33] Klaus Ehret et al. New ALPS Results on Hidden-Sector Lightweights. *Phys. Lett.*, B689:149–155, 2010.

[34] Albert Einstein. Lens-Like Action of a Star by the Deviation of Light in the Gravitational Field. *Science*, 84:506–507, 1936.

[35] Zujie Fang, Ken Chin, Ronghui Qu, and Haiwen Cai. *Fundamentals of optical fiber sensors*, volume 226. John Wiley & Sons, 2012.

[36] D. J. Fixsen. The temperature of the cosmic microwave background. *The Astrophysical Journal*, 707(2):916, 2009.

[37] Timothy Edgcumbe Ford. Microbiological safety of drinking water: United states and global perspectives. *Environmental Health Perspectives*, 107(Suppl 1):191, 1999.

[38] Maurizio Giannotti, Igor Irastorza, Javier Redondo, and Andreas Ringwald. Cool WISPs for stellar cooling excesses. *JCAP*, 1605(05):057, 2016.

[39] W. F. Giauque. A thermodynamic treatment of certain magnetic effects. a proposed method of producing temperatures considerably below 1 absolute. *Journal of the American Chemical Society*, 49(8):1864–1870, 1927.

[40] Peter R Girguis, Aaron E Cozen, and Edward F DeLong. Growth and population dynamics of anaerobic methane-oxidizing archaea and sulfate-reducing bacteria in a continuous-flow bioreactor. *Applied and environmental microbiology*, 71(7):3725–3733, 2005.

[41] Peter KF Grieder. *Cosmic rays at Earth*. Gulf Professional Publishing, 2001.

[42] LEGIONELLA GROWTH-PROMOTING. Disinfection of water distribution systems for legionella. In *Seminars in respiratory infections*, volume 13, pages 147–159, 1998.

[43] H.P. Hack and ASTM Committee G-1 on Corrosion of Metals. *Galvanic Corrosion*. ASTM special technical publication. American Society for Testing Materials, 1988.

[44] Reza Hodajerdi. *Production cavity and central optics for a light shining through a wall experiment*. PhD thesis, Universität Hamburg, 2015.

[45] Dieter Horns. Internal communication.

[46] K. D. Irwin and G. C. Hilton. Transition-edge sensors. In Christian Enss, editor, *Cryogenic particle detection*, pages 63–149. Springer-Verlag Berlin Heidelberg, 2005.

[47] KD Irwin. An application of electrothermal feedback for high resolution cryogenic particle detection. *Applied Physics Letters*, 66(15):1998–2000, 1995.

[48] T. Isogai, J. Miller, P. Kwee, L. Barsotti, and M. Evans. Loss in long-storage-time optical cavities. *Opt. Express*, 21:30114–30125, 2013.

[49] Joerg Jaeckel and Andreas Ringwald. The Low-Energy Frontier of Particle Physics. *Ann. Rev. Nucl. Part. Sci.*, 60:405–437, 2010.

[50] Jihn E. Kim. Weak Interaction Singlet and Strong CP Invariance. *Phys. Rev. Lett.*, 43:103, 1979.

[51] Adriana E. Lita, Aaron J. Miller, and Sae Woo Nam. Counting near-infrared single-photons with 95% efficiency. *Opt. Express*, 16(5):3032–3040, Mar 2008.

[52] Sumitomo Heavy Industries Ltd. Technical instruction for the F-50H compressor unit.

[53] Sumitomo Heavy Industries Ltd. Operation manual for the SRP-062 Series Cryocooler.

[54] Alessandro Melchiorri, Antonello Polosa, and Alessandro Strumia. New bounds on millicharged particles from cosmology. *Phys. Lett.*, B650:416–420, 2007.

[55] Kristina D Mena and Charles P Gerba. Risk assessment of pseudomonas aeruginosa in water. In *Reviews of Environmental Contamination and Toxicology Vol 201*, pages 71–115. Springer, 2009.

[56] Aaron J Miller, Adriana E Lita, Brice Calkins, Igor Vayshenker, Steven M Gruber, and Sae Woo Nam. Compact cryogenic self-aligning fiber-to-detector coupling with losses below one percent. *Optics express*, 19(10):9102–9110, 2011.

[57] N. Minorsky. Directional stability of automatically steered bodies. *Journal of the American Society for Naval Engineers*, 34(2):280–309, 1922.

[58] Gerard Muyzer and Alfons J. M. Stams. The ecology and biotechnology of sulphate-reducing bacteria.

[59] K. A. Olive et al. Review of Particle Physics. *Chin. Phys.*, C38:090001, 2014.

[60] R. D. Peccei and Helen R. Quinn. CP Conservation in the Presence of Pseudoparticles. *Phys. Rev. Lett.*, 38:1440–1443, 1977.

[61] J. M. Pendlebury et al. Revised experimental upper limit on the electric dipole moment of the neutron. *Phys. Rev.*, D92(9):092003, 2015.

[62] Arno A. Penzias and Robert Woodrow Wilson. A Measurement of excess antenna temperature at 4080-Mc/s. *Astrophys. J.*, 142:419–421, 1965.

[63] H. Pirmakoff. Photoproduction of neutral mesons in nuclear electric fields and the mean life of the neutral meson. *Phys. Rev.*, 81:899, 1951.

[64] Max Planck. On the law of distribution of energy in the normal spectrum. *Annalen der Physik*, 4(553):1, 1901.

[65] Frank Pobell. *Matter and methods at low temperatures*. Springer Science & Business Media, 2007.

[66] Ray Radebaugh. Development of the pulse tube refrigerator as an efficient and reliable cryocooler. In *Proc. Institute of Refrigeration (London)*, 1999–2000.

[67] Ray Radebaugh. Development of the pulse tube refrigerator as an efficient and reliable cryocooler. In *Proceedings of Institute of Refrigeration*, volume 96, pages 1999–2000. Citeseer, 2000.

[68] T.S Rao and K.V.K Nair. Microbiologically influenced stress corrosion cracking failure of admiralty brass condenser tubes in a nuclear power plant cooled by freshwater. *Corrosion Science*, 40(11):1821 – 1836, 1998.

[69] Walter J. Rossiter, McClure Godette, Paul W. Brown, and Kevin G. Galuk. An investigation of the degradation of aqueous ethylene glycol and propylene glycol solutions using ion chromatography. *Solar Energy Materials*, 11(5):455 – 467, 1985.

[70] Vera C. Rubin and W. Kent Ford, Jr. Rotation of the Andromeda Nebula from a Spectroscopic Survey of Emission Regions. *Astrophys. J.*, 159:379–403, 1970.

[71] Gerhard Schikorr. Ueber eisen(ii)-hydroxyd und ein ferromagnetisches eisen(iii)-hydroxyd. *Zeitschrift fuer anorganische und allgemeine Chemie*, 212(1):33–39, 1933.

[72] A Schippers, H Von Rge, and W Sand. Impact of microbial diversity and sulfur chemistry on safeguarding sulfudic mine waste. *Minerals Engineering*, 9(10):1069 – 1079, 1996.

[73] Amel Shamseldeen Ali Alhassan. Internal communication.

[74] George F. Smoot et al. Structure in the COBE differential microwave radiometer first year maps. *Astrophys. J.*, 396:L1–L5, 1992.

[75] D. N. Spergel et al. First year Wilkinson Microwave Anisotropy Probe (WMAP) observations: Determination of cosmological parameters. *Astrophys. J. Suppl.*, 148:175–194, 2003.

[76] Gheorghe Stan, Stuart B Field, and John M Martinis. Critical field for complete vortex expulsion from narrow superconducting strips. *Physical review letters*, 92(9):097003, 2004.

[77] Manfred Sumper and Nils Kröger. Silica formation in diatoms: the function of long-chain polyamines and silaffins. *Journal of Materials Chemistry*, 14(14):2059–2065, 2004.

[78] JAMES M Tiedje. Ecology of denitrification and dissimilatory nitrate reduction to ammonium. *Biology of anaerobic microorganisms*, 717:179–244, 1988.

[79] Dieter Trines. Internal communication.

[80] K. van Bibber, G. G. Raffelt, D. M. Moltz, F. R. Huson, J. T. White, P. M. McIntyre, R. N. Boyd, and H. N. Nelson. Construction and operation of an axion helioscope. 1988.

[81] Karl van Bibber and Gianpaolo Carosi. Status of the ADMX and ADMX-HF experiments. In *8th Patras Workshop on Axions, WIMPs and WISPs (AXION-WIMP 2012) Chicago, Illinois, July 18-22, 2012*, 2013.

[82] Hans-Gerrit Vogt, Heinrich Schultz, and Jan-Willem Vahlbruch. *Grundzüge des praktischen Strahlenschutzes*. Hanser, 2011.

[83] Jan Eike von Seggern. *Constraining Weakly Interacting Slim Particles with a Massive Star and in the Laboratory*. PhD thesis, DESY, 2014.

[84] C. Wang, G. Thummes, and C. Heiden. A two-stage pulse tube cooler operating below 4 K. *Cryogenics*, 37:159–164, 1997.

[85] Hamburg Wasser. Trinkwasseranalyse 2013 - Grundwasserwerk Baursberg.

[86] Steven Weinberg. A New Light Boson? *Phys. Rev. Lett.*, 40:223–226, 1978.

[87] Christoph Weinsheimer. Internal communication.

[88] Frank Wilczek. Problem of Strong p and t Invariance in the Presence of Instantons. *Phys. Rev. Lett.*, 40:279–282, 1978.

[89] Klaus Zenker. Internal communication.

[90] A. R. Zhitnitsky. On Possible Suppression of the Axion Hadron Interactions. (In Russian). *Sov. J. Nucl. Phys.*, 31:260, 1980. [Yad. Fiz.31,497(1980)].

[91] F. Zwicky. Die Rotverschiebung von extragalaktischen Nebeln. *Helv. Phys. Acta*, 6:110–127, 1933.

Acknowledgments

Eidesstattliche Versicherung
Declaration on oath

Hiermit erkläre ich an Eides statt, dass ich die vorliegende Dissertationsschrift selbst verfasst und keine anderen als die angegebenen Quellen und Hilfsmittel benutzt habe.

I hereby declare, on oath, that I have written the present dissertation by my own and have not used other than the acknowledged resources and aids.

Hamburg, den
City and date

Unterschrift
Signature